PART III:

ANALOGUE MODELS

PART III: ANALOGUE MODELS

III. 1 INTRODUCTION

III.1.1 The role of experimental models in volcanology

As in many others geological disciplines, experimental research is essential to understand volcanic processes. Recently, experiments have been applied to study complex dynamical processes and their underlying mechanisms.

Without models (experimental, theoretical, mathematical) volcanologists are limited to qualitative interpretations of field observations and remote sensing (Martí and Folch, 2005). Field data are fundamental and useful to compare the results obtained with the different models and to check their reliability and veracity. However, as we have mentioned before (see sections II.2.5 and II.5.8), there are several handicaps around the obtaining of field measures.

In short, analogue experiments are an important and an indispensable tool to explore new phenomena, observe processes, determine the values of key parameters, test hypotheses and theoretical models and validate computational models.

The principal drawback of analogue models is a problem of scale. Volcanic systems involve processes that operate over a much wider range of length and timescales than is possible to reproduce in the laboratory. The range of scales present can be crucial to the dynamics because they can be dominated by the interaction of processes on different scales. Therefore, the scaling process is important when reproducing eruptive processes with an analogue experiment. In many cases, the appropriate scaling relationships are unknown. However, rigorous scaling almost always involves the physical parameters of the materials used as well as the dimensions of the system. Therefore, fully-scaled dynamical simulations will usually require the use of suitably-chosen analogue materials. If analogue experiments cannot be fully scaled they are not true 'simulations' of natural processes and are unlikely to reproduce the full range of behaviour. The role of experiments, in this case, is primarily as a tool to identify, investigate and visualize processes that cannot be directly observed in nature (Mader et al., 2004; Martí and Folch, 2005).

III.1.2 Classification

Experimental models can be classified according to the applied materials (Mader et al., 2004):

➤ **Natural materials:** These experiments are focused on the determination directed towards determining the basic physicochemical parameters of the system. Usually, natural materials are use for very small-scale processes (Mader et al., 2004).

➤ **Analogue materials:** These materials try to emulate the natural ones with a factor of scale regarding physical properties. Analogue materials are use for the study of large-scale dynamic processes. However, analogue materials rarely capture the full range of the physicochemical behaviour of the natural system leading to alterations in the experimental results. In that case it is impossible to extrapolate the experimental results to reality. This remains the principal objection to the use of analogue material (Mader et al., 2004).

III.2 STATE OF THE ART

III.2.1 Previous analogue models of caldera collapse processes

The aim of this section is to briefly describe previous analogue models of caldera collapse processes. A summary of the most important results is also included, principally those relevant for this study. Furthermore, Table 3.1 lists the applied analogue devices with a short description of the apparatus and the analogue materials.

Analogue models on collapse calderas performed during the last two decades can be grouped depending on the topic they are focused on. There exit principally five different groups:

➤ **Pure collapse models:** These experiments simulate the development of collapse calderas, as a consequence of a pressure decrease within the chamber (Komuro, 1987; Martí et al., 1994; Roche et al., 2000; Acocella et al., 2000; Acocella et al., 2001a;

Acocella et al., 2001b; Roche and Druitt, 2001; Walter and Troll, 2001; Kennedy et al., 2004; Lavallée et al., 2004)

➤ **Collapse by doming:** The experiments simulate the development of caldera collapses at the summit part of resurgent domes during the pressure increase inside the magma chamber (Komuro et al., 1984; Martí et al., 1994; Acocella et al., 2000; Walter and Troll, 2001).

➤ **Collapse during multicycling deformation processes:** The experiments simulate the development of the superimposition of doming on collapse and vice versa (Martí et al., 1994; Acocella et al., 2000; Walter and Troll, 2001)

➤ **Collapse with topography presence:** The experiments simulate the development of a collapse caldera considering the presence of a volcanic edifice (Walter and Troll, 2001; Lavallée et al., 2004).

➤ **Collapse under a specific regional tectonic regime:** The experiments simulate pure collapse due to magma chamber underpressure, considering the role of pre-existing structures and the effect of superimposing a regional tectonic regime (deviatoric stress) to the local stress field (Acocella et al., 2004; Holohan et al., 2005).
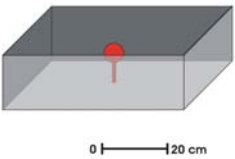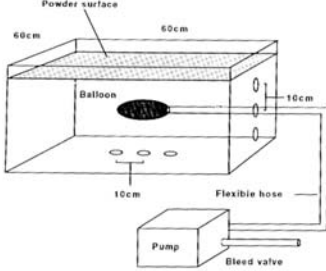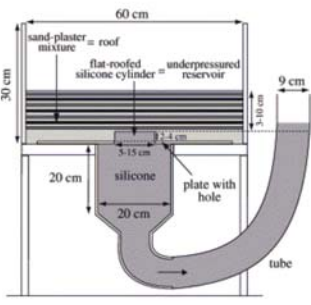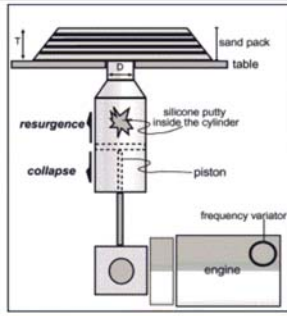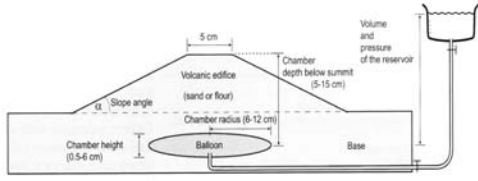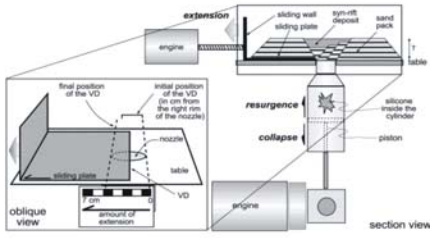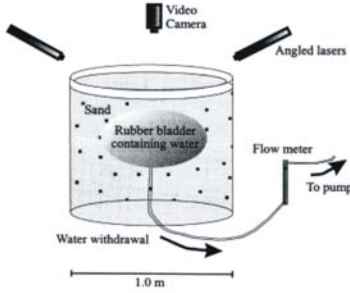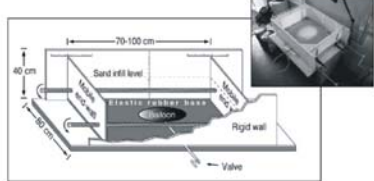
Author	Year	Experimental Device		Materials
Komuro et al.	1984	0 ⊢—⊣20 cm	Box with dimensions 12 × 45 × 55 cm. Hole of 1 cm at the bottom. Through this hole is passed a shaft having a rigid globe of R-cm diameter. The shaft, which is controlled by a motor, rises with an uniform speed. The box is filled with the analogue material, once the shaft has been adjusted to the desired depth. Scale 1:200.000	**Material I:** dry sand + clay powder $\rho=1.25$ g/cm^3 $\phi=26^\circ$ $c=1.3\cdot10^3$ Pa **Material II:** clay powder $\rho=1.12$ g/cm^3 $\phi=28$ $c=5.2\cdot10^3$ Pa
Komuro, H.	1987	A ball of ice is introduced in a rectangular container and covered with the analogue material. Evaporation of ice imitates the outpouring or effusion of magma. Scale 1:200.000		dry sand + clay powder $\rho=1.25$ g/cm^3 $\phi=26^\circ$ $c=1.3\cdot10^3$ Pa
Martí et al.	1994		Glass tank with dimensions 60 × 60 cm filled with alumina powder. A latex balloon is connected via a flexible hose through a pressure gauge to a small pump. Scale 1:100.000	fused alumina powder $\rho=3.1$ g/cm^3 $\phi=38^\circ$ $c=200$ Pa $\varphi=0.054$ mm
Roche et al.	2000		Experiments carried out in 2-D and 3-D. 2-D apparatus: 60 ×10 ×30 cm. 3-D apparatus:60 × 60 ×30 cm The silicone layer representing the magma chamber is underlain by a large volume of silicone connected to an outflow tube, which was blocked during the preparation phase. The experiments are initiated by unlocking the outflow tube. The silicone is allow to flow outside the reservoir, pushed by the subsiding roof. Scale 1:100.000	**Material I:** dry sand $\rho=1.5$ g/cm^3 $\phi=33.5^\circ\pm0.8^\circ$ $\varphi_{mean}=200$ μm **Material II:** silicone putty $\rho=1.15$ g/cm^3 $\nu=2.4\cdot10^4$Pa
Roche & Druitt	2001			**Material I:** dry sand $\rho=1.36$ g/cm^3 $\phi=29^\circ$ $c=40$-60 Pa **Material II:** silicone putty $\rho=1.15$ g/cm^3 $\nu=2.4\cdot10^4$Pa
Acocella et al.	2000		Piston within a cylinder at the base of a table. Horizontal layers of sand are placed on the table covering the output hole of the cylinder. The piston, controlled by an engine, moves upward or downward the silicone putty simulating doming and collapse.	**Material I:** dry quartz sand $\rho=1.5$ g/cm^3 $\phi=35^\circ$ $c=200$-500 Pa
Acocella et al.	2001		Scale 1:100.000	**Material II:** silicone putty $\rho=1.14$g/cm^3 $\nu=10^4$Pa

$\rho \rightarrow$ **density**　$\phi \rightarrow$ **internal friction angle**　**c**$\rightarrow$ **cohesion**　$\nu \rightarrow$ **viscosity**　$\varphi \rightarrow$ **particle diameter**

Table 3.1: List of the existing studies of analogue models of caldera collapse. A short description and sketch of the experimental device is included as well as the physical properties of the analogue materials.

Author	Year	Experimental Device	Materials
Walter & Troll	2001	Glass tank of approximately 1m³ is filled with sand. The balloon is placed in the centre of the box. Inflatable reservoirs are constructed by attaching two equivalent-sized mats of very thin stretchy rubber at the outer rims. In the lower mat, an inlet and connected a pipe system is inserted, through which inflation and evacuation of a balloon is accomplished. An outflow valve is joined to the pipe. Scale 1:100.000	**Material I:** dry quartz sand ρ=1.5-1.7 g/cm³ ϕ= 31° c=40-50 Pa φ=500 μm **Material II:** flour ρ=0.57 g/cm³ ϕ= 33° c=35 Pa φ=100-200 μm
Acocella et al.	2004	Piston within a cylinder at the base of a table. Horizontal layers of sand are placed on the table covering the output hole of the cylinder. The piston, controlled by an engine, moves upward or downward the silicone putty. A sliding plate above the table allows the simulation of the extensional regime. Scale 1:100.000	**Material I:** dry quartz sand ρ=1,5 g/cm³ ϕ= 35° c=200-500 Pa **Material II:** silicone putty ρ=1,14g/cm³ ν=10⁴Pa
Kennedy et al.	2004	The apparatus comprises a cylinder 0.9 m in diameter and 1.0 m in height. A 45-l water-filled rubber bladder (0.6 m diameter) is buried within the sand to represent a magma chamber. Magma withdrawal is simulated using a tube attached to the underside of the analogue chamber, with a flowmeter to control the rate of water evacuation. Scale 1:40.000	sand ρ=1,89 g/cm³ c=18-240 Pa
Lavallée et al.	2004		
Holohan et al.	2005	The apparatus consists of a sand-filled box with two free walls. Inward and outward motions of these exert horizontal compressive stress and horizontal extensional stress on the sand medium. A rubber sheet fixed to the bottom of the end walls and distributes the regional stresses uniformly across the deforming medium. Sill-like rubber balloons buried in the sand simulate the magma chamber. These are circular in plan view and have rigid rims to preserve their plan view shape under stress. The balloons are inflated and deflated via a narrow tube connected to an air inlet valve outside the sandbox. Scale 1:100.000	**Material I:** dry quartz sand ρ=1.3-1.5 g/cm³ ϕ= 31° c=40-50 Pa φ=300 μm **Material II:** flour ρ=0.57 g/cm³ ϕ= 33° c=35 Pa φ=100-200 μm

$\rho \rightarrow$ **density** $\phi \rightarrow$ **internal friction angle**   **c** $\rightarrow$ **cohesion** $\nu \rightarrow$ **viscosity** $\varphi \rightarrow$ **particle diameter**

Table 3.1 (continuation): List of the existing studies of analogue models of caldera collapse. A short description and sketch of the experimental device is included as well as the physical properties of the analogue materials.

❖   **PURE CALDERA COLLAPSE MODELS**

Analogue models based on pure caldera collapses (subsidence takes place as a consequence of a pressure decrease within the chamber) conclude that:

➢   This collapse type depends on the roof aspect ratio **R**. For low values of **R**, the caldera collapse is piston-like and the subsiding block is coherent. Collapse is controlled by a combination of outward dipping reverse faults and vertical or sub-vertical ring faults (Fig. 3.2 A). By contrast, for higher roof aspect ratios, the collapse is more funnel type. Collapse occurs along multiple reverse faults. A first pair of faults nucleates at the top of the magma chamber and propagates upward; this triggers the formation of a second pair, and so on until the structures arrive at surface (Fig. 3.1 B). No peripheral faults generate and subsidence is greater at depth than at surface.
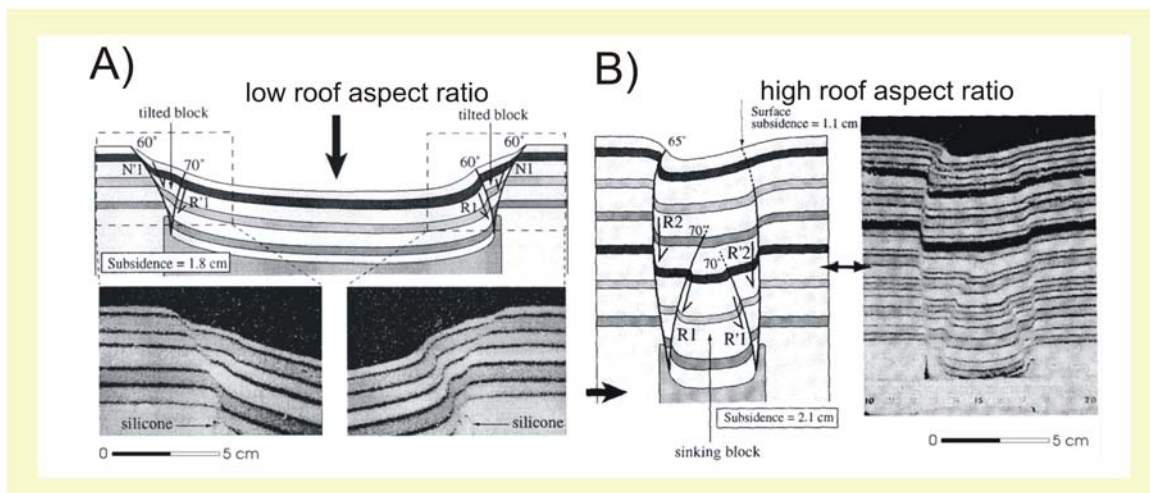
Fig. 3.1: Photographs and sketches of two of the experiments conducted by Roche et al. (2000). **(A)** R=0.2. **(B)** R=2 . **R** Reverse fault; **N** Normal fault. (Modified from Roche et al., 2000)

➢   Collapse begins with down flexure of the roof ("down sagging") more marked at low **R**.

➢   The percentage of extensional area in relation to the total collapse area increases with **R**.

➢   The resulting caldera is characterized by two depressions (Fig. 3.2 A). The inner one, is bordered by outward-dipping, high-angle reverse ring faults. The outer depression is

defined by inward-dipping normal ring faults. The strata located between the reverse and the normal faults are tilted inward by approximately 40°. By contrast, the layers in the central collapse basin are horizontal.

➢ During the collapse, the caldera walls break down causing the caldera rim to propagate outwards. The blocks fall and tilt from the outer undisturbed wall into the basin along a set of interconnected faults.

➢ In a plot of inner depression diameter / outer depression diameter (**Di / Do**) towards sand-pack thickness (i.e. analogue magma chamber depth) / inner depression diameter (**T / Di**) (Fig. 3.2 B), the distribution of the experimental results and of the real data are similar, suggesting that at least some nested calderas result from single episodes of collapses. Furthermore, the relative size of the depressions (**Di / Do**) decreases with (**T / Di**) (line A; Fig. 3.2 B). Thus, in the experimental depressions, diameter and depth of nucleation are well correlated, independently of asymmetries and the shape of the sand–silicone interface.
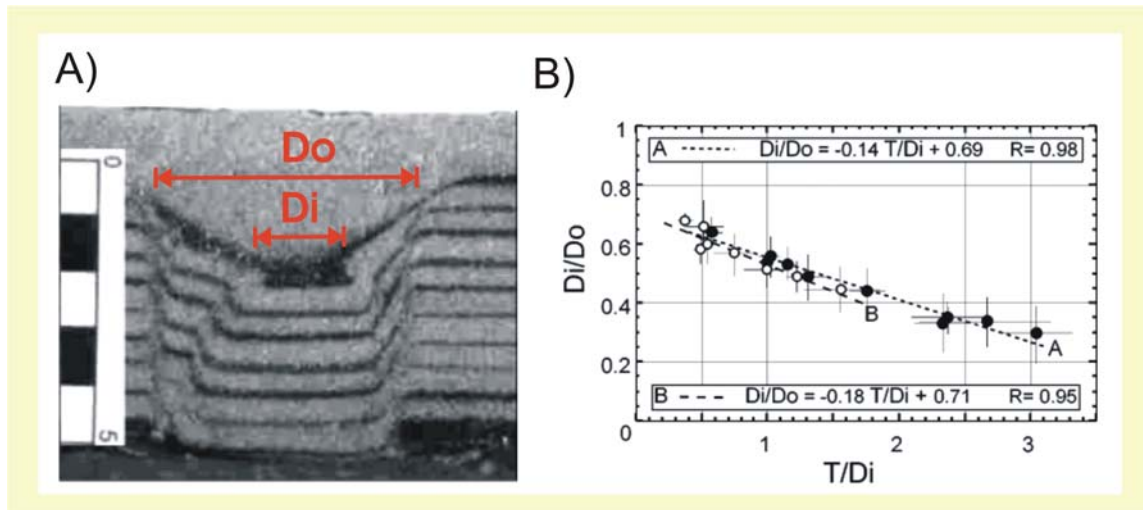
Fig. 3.2: **(A)** Cross section of one of the experiments. The inner depression is bordered by outward-dipping reverse faults; outer depression is bordered by inward-dipping normal ring faults. **(B)** Plot of (Di/Do) vs. (T/Di) in experiments (black dots, best fit line A) and in nature (white dots, best fit line B). **Di** Diameter of the inner depression; **Do** Diameter of the outer depression; **T** Sand-pack thickness (i.e. magma chamber analogue depth). (Modified from Acocella et al., 2001b)

➢   For a certain type of experimental devices (with silicone reservoir as magma chamber analogue) high roof aspect ratios (R >1) can lead to non-coherent collapses (Fig. 3.3). In theses cases, no surface deformation is visible, but a very complex pattern of deformation occurs at depth. The collapse occurs when the roof becomes too thin to sustain gravitational stresses and is bounded by steep, outward-dipping fractures, and develops through about half the thickness of the roof and its height is equal to its width.
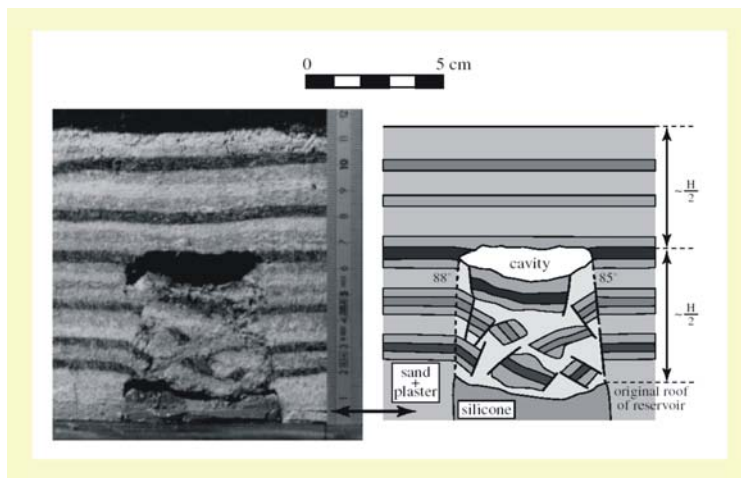
Fig. 3.3: Photograph and schematic cross-section in an experiment with R=2. H is the height of the roof. Highly brecciated material within the subsided part is shown in light grey, individualised blocks. (Modified from Roche et al., 2001)

❖   **CALDERA COLLAPSE BY DOMING**

In these experimental studies, the caldera collapse develops at the apical part of a dome (e.g. Komuro et al., 1984; Martí et al., 1994; Acocella et al., 2000). The main features of these collapses obtained by the experimental studies may be summarized as follows:

➢   During the first doming stages, radial cracks appear from the centre of the dome. Afterwards, concentric cracks generate outward from the centre of the dome, where extensive stresses are greater (Fig. 3.4). The number of faults depends on the analogue material used in the experiment. Additionally, the physical properties of analogue materials have an effect on the spacing of cracks, which consequently determines whether a collapse structure will form or not.

➢   Radial and concentric cracks always intersect with right angles and the central part of the dome collapses by means of small blocks bounded by both types of cracks (Fig. 3.4) and is bounded by nearly vertical fault scarps. That occurs when extensional stresses exceed the material tensile strength.
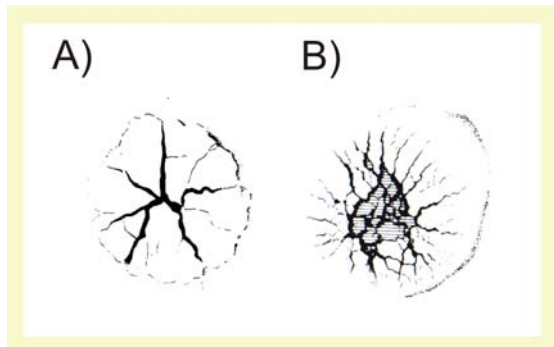
Fig. 3.4: Schematic plan view representation of the final structures that can be observed in the experiments of Komuro et al. (1984) and Komuro (1987) with materials I **(A)** and II **(B)** (See Table 3.1). (Modified from Komuro et al., 1984)

❖   **CALDERA COLLAPSE DURING MULTICYCLING PROCESSES**

Calderas and domes are commonly related to inflation-deflation of magma chambers (Smith and Bailey, 1968; Lipman, 2000), which can control the structural features of caldera collapse like fault orientation and reactivation, caldera geometry and size, etc. Therefore, realistic analogue models have to consider the possibility of a previous and/or later deformation in the area of collapse due to magma chamber inflation. Several authors (e.g. Martí et al., 1994; Acocella et al., 2000; Walter and Troll, 2001) considered this and carried out experiments with inflation and deflation processes. The most important results are:

➢   Radial and concentric fractures (polygonal intracaldera structure) appear during the tumescence stage. These radial cracks, subordinate concentric reverse faults and horseshoe-shaped faults define an apical graben with a mean diameter approximately half of the reservoir's diameter (Fig. 3.5).

➢   Subsequent evacuation of the experimental chamber results in a closure of the radial cracks, accompanied by two concentric domains: (a) a bell-shaped fracture system forming

the major caldera basin (main ring fault) and (b) periphery en echelon faults with diverse dips.

➢ There exists reactivation of faults formed due to inflation during the collapse phase and the subsiding block is controlled by high-angle inward dipping reverse faults and outward dipping normal faults (Fig. 3.5). The interaction of reversal reactivated radial fractures and newly formed concentric collapse faults generated a heterogeneous polygonal intracaldera structure and non-coherent caldera subsidence in all cyclic experiments.

➢ In each cycle (a) radial dome structures propagated outwards and increased in quantity, and (b) reactivated concentric faults shifted outward, accompanied by outward-propagating flank steepening.

➢ The maximum cumulative caldera subsidence was a combination of apical graben fault displacement plus ring–fault subsidence.
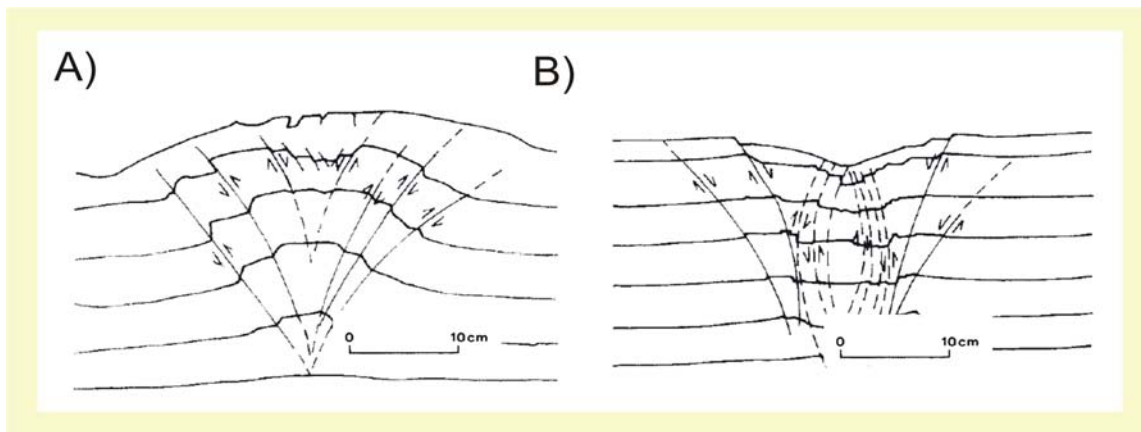
Fig. 3.5: Sketches of the experiments carried out by Martí et al. (1994) to show internal structure with interpretation of fault systems. **(A)** Uplift dome after tumescence. **(B)** Collapse structure formed after balloon deflation below tumescence dome. (Modified from Martí et al., 1994)

❖ **EXPERIMENTS WITH TOPOGRAPHY**

At some volcanic complexes the topographic load may be the principal upper-crustal stress field. In many cases, volcano loading is able to modify the regional fault patterns, increase the fault throw and induce extension (Lavallée et al., 2004, and

references therein). Despite this fact, previous commented analogue models use a flat horizontal topography, although calderas usually form in volcanic fields with significant topographic relief. Therefore, some authors (e.g. Walter and Troll, 2001; Lavallée et al., 2004) considered in their experiments the presence of a volcanic edifice. The results obtained, strongly conditioned on the relationship between the size of the edifice and the dimensions of the magmatic reservoir, can be summarized as follows:

Experiments with small topography in comparison with the magma chamber size:

➢   Resulted calderas are of trapdoor-style (Fig. 3.6).

➢   In presence of topography, increasing the load above the analogue chamber leads to the formation of faults at the topographic margin and the concentration of the subsidence along the inner set of subsidence-controlling faults. Furthermore, the topographic load entails an increase of the depth of the caldera by up to 20% and a decrease of the diameter of the main subsidence-controlling ring faults, the outward growth rate of sagging, the diameter of sagging and the ellipticity of the area of sagging.

➢   Moving the sand pile from above the centre to above the edge of the analogue magma chamber reduces the loading effect on the system. Therefore, moving the topographic relief to an off-centred position has similar effects as having no pre-existing relief.
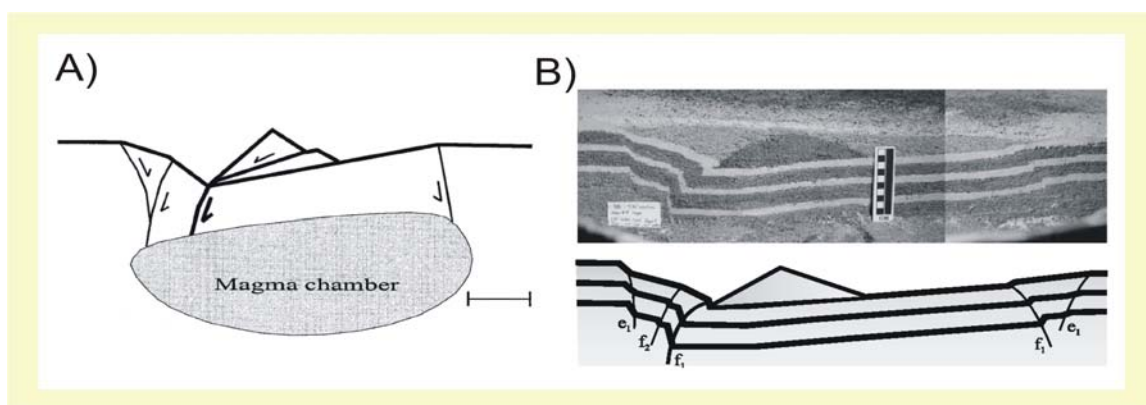
Fig. 3.6: (A) A schematic view showing the relationship between the size of the edifice and the magmatic reservoir. Notice that the first is considerably smaller. **(B)** Cross-section for a experiments with heavy topographic masses, the subsidence concentrates along f1, which propagates at the margin of the topography. The displacement can be seen to be greatest at depth, showing that the subsidence-controlling fault propagated upward. (Modified from Lavallée et al., 2004)

Experiments with large topography in comparison to the magma chamber size:

➢   The topography affects the distribution, location and orientation of the concentric fracture systems. A steep cone causes the concentric fractures to have a less pronounced tendency to form open faults and the central collapse basin fractures are disorganised (Fig. 3.7). Additionally, irregular edifice morphologies lead to piecemeal caldera floors even in pure evacuation experiments.

➢   For cone morphologies not directly centred above the chamber, the pattern of radial fractures is uniform only near the centre. Away from the centre, the radial fractures propagate dominantly parallel to the dip line of the slope.

➢   With several stages of doming and evacuation, the extent of radial faults and the diameter of concentric faults are thought to migrate outwards with each additional stage. In this case, the number of faults increases incrementally, reducing the stability of the volcano flanks (Fig. 3.7).
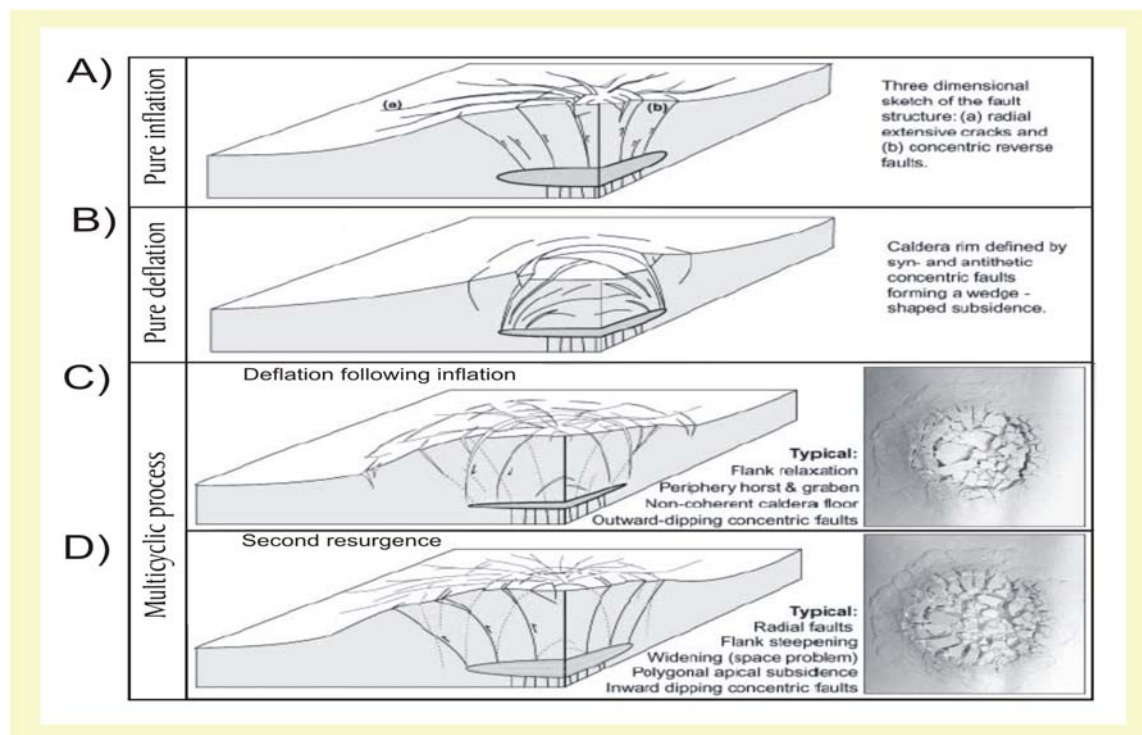
Fig. 3.7: Three-dimensional reconstruction of characteristic structures formed during the experiments of Walter and Troll (2001) **(A)** Pure inflation experiment. **(B)** Pure deflation experiment. **(C)** and **(D)** multi-stage inflation and subsequent deflation experiment (Modified from Walter and Troll, 2001)

❖   **COLLAPSE UNDER A SPECIFIC TECTONIC REGIME**

Pre-existing regional structures (inherited strain) and the existence of a simultaneous regional stress field (deviatoric stress) may influence the development of structures during collapse and resurgence. Some experimental studies (e.g. Acocella et al., 2000; Holohan et al., 2005) tried to define these effects of far-field stresses (i.e. regional tectonics) on caldera structures and near-field structural patterns. Since several resurgences and calderas are located in extensional settings, the extensional tectonics is the most representative far-field stress to consider for any simulation (Acocella et al., 2004). Obtained results can be summarized as follows:

➢   In collapse over extension caldera subsidence begins with down sagging accompanied by an outer concentric zone of tensional fractures. Collapse continues along outward-dipping reverse faults in the intracaldera area, accompanied by normal faulting in the peripheral zone (Fig. 3.8). The areas encompassed by the intracaldera and the peripheral fault zones in stressed experiments remained approximately constant with (and therefore independent of) increasing pre-collapse regional strain.
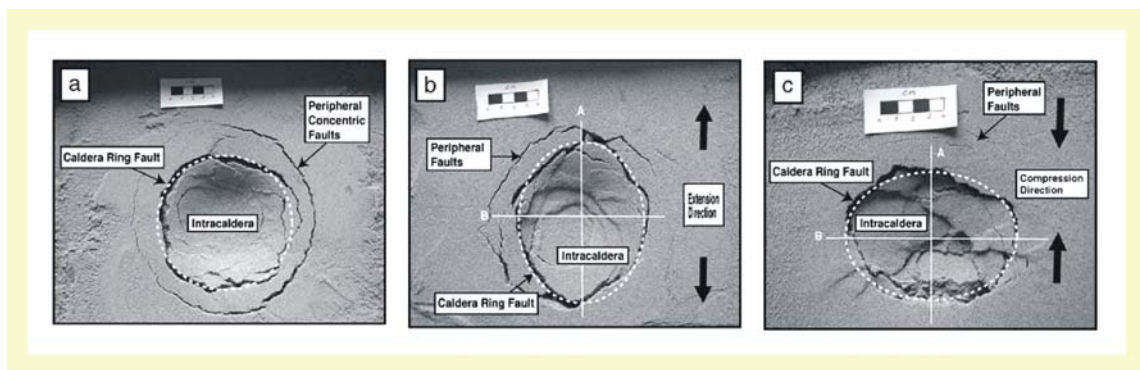
Fig. 3.8: Plan view photographs of experiments made in sand. **(A)** Experiments under stress-free conditions. **(B)** Experiments under regional extension. **(C)** Experiments under regional compression. The major axes of calderas are denoted as A- and B-axes. The A-axis is taken as perpendicular to the end walls and the B-axis parallel to the end walls. (Modified from Holohan et al., 2005)

➢   Reverse faults bordering the depression reactivate the regional normal faults, if these are close. No reactivation occurs where the reverse faults are transverse to the regional faults, reactivation is only observed on sections perpendicular to the extension direction (Fig.3.9)

➢   The inner caldera depression is elliptic, with the major axis parallel to the extension direction. The eccentricity of calderas depends on the number of reactivated regional normal faults. Reactivation of only one regional fault leads to higher eccentricities, whereas every reactivated regional fault induces a decrease in the eccentricity (Fig. 3.9).
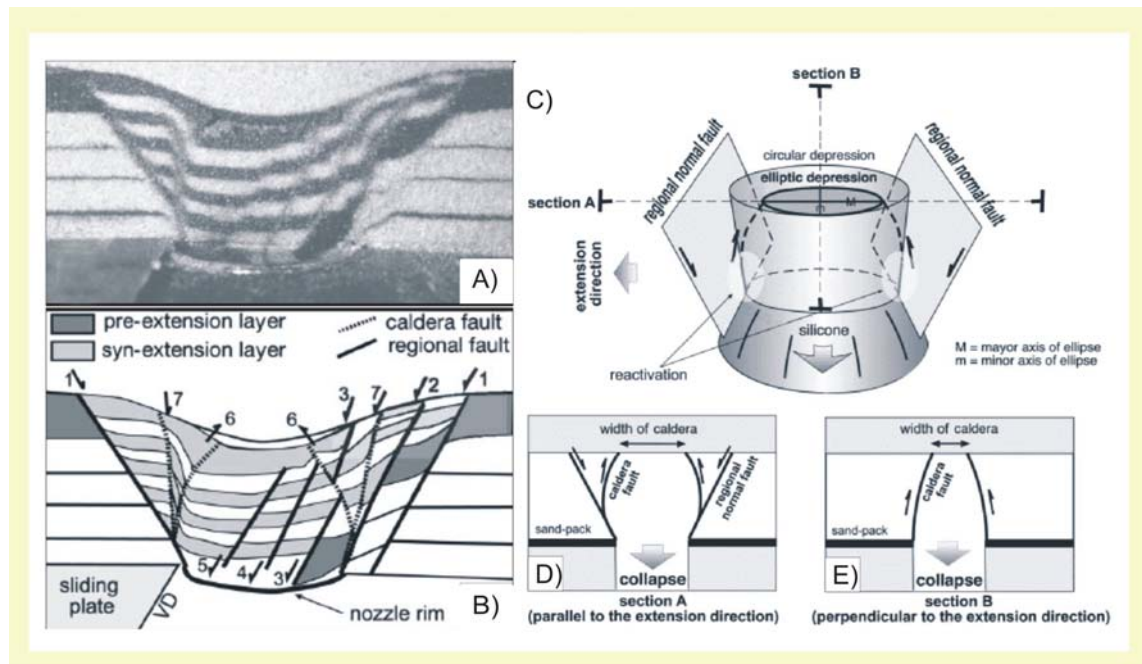
Fig. 3.9: Results obtained by Acocella et al. (2004). **(A)** Photograph of a collapse experiment under extension. Cross section view parallel to the extension direction.**(B)** Sketch Line drawing of the same experiment.**(C)** Proposed mechanism for the reactivation of regional faults during collapse and for the elongation of the caldera parallel to the extension direction. **(D)** The reverse faults, where tangent in strike to the regional faults, become partly inward dipping, inducing a wider depression on the corresponding parts at surface. **(E)** No reactivation is observed when the regional faults are transverse to the reverse faults. (Modified from Acocella et al., 2004)

➢   In active tectonic regimes, distortion of caldera ring faults may be of great significance for caldera formation. This distortion may occur due to: elongation of the concentric caldera ring and peripheral fault systems in the direction of least horizontal compressive stress, truncation and "capture" of ring and peripheral faults by the pre-existing fault systems associated with the regional stress field or post-collapse deformation of the caldera structures due to regional strain. Furthermore, because of the stress-related distortion, ring fault orientation varies from steeply dipping to shallower dips. This variation of caldera fault dip may play a role in the localization of eruptions or intrusions along such an elliptical ring fissure.

➢   In multicycling processes there exists reactivation of the former collapse caldera faults during resurgence and the development of the caldera faults are partly controlled by the pre-existing regional structures, whereas the modalities of reactivation of the caldera faults during resurgence are identical to the ones observed without a regional extension.

III.2.2 Summary of previous results

In order to facilitate the comprehension and understanding of the rest of this chapter, we consider necessary to present a schematic summary of the most important aspects commented in this section. Figure 3.10 offers a sketch summing up the different aspects and topics commented in this section concerning the state of the art of collapse calderas analogue models.
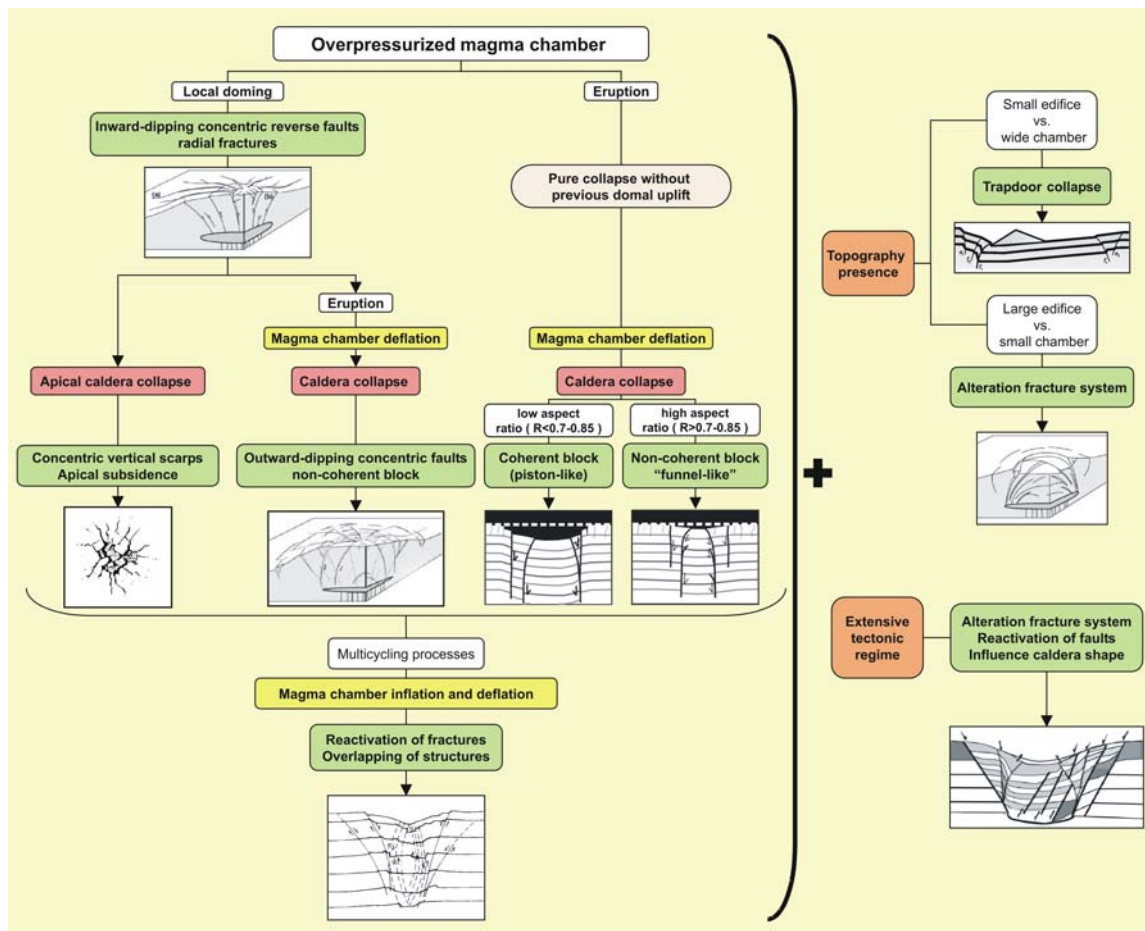
Fig. 3.10: Sketch summing up the different aspects and topics commented in this section concerning the state of the art of collapse caldera analogue models.

III.2.3 Restrictions of the existing analogue models

Before discussing any experimental results and their geological implications, it is necessary to determine the restrictions of the experimental devices and, if possible, to try to minimize their effect in future analogue models.

The restrictions and limitations found in the experimental devices applied to the study of collapse calderas vary from device to device, and are principally dependent on the used materials and the magma chamber analogue. For all existing experimental devices the most relevant restrictions are:

➢ **Unrealistic deformation of the magma chamber**
➢ **Existence of grain flow processes**
➢ **Impossibility of dike injection**
➢ **Homogeneous magma chamber roof**
➢ **Thermal effects**

❖ **UNREALISTIC DEFORMATION OF THE MAGMA CHAMBER**

The choice of the magma chamber analogue is an important step in the design of an apparatus aimed at studying caldera collapse processes. The physical properties of the magma chamber analogue, as well as its deformation pattern, control the subsidence model and the resulting structures, determining whether the analogue model is realistic or not.

In previous studies, the most widespread magma chamber analogues are the latex balloon, filled with air or water, and the silicone reservoir. Other analogue materials like a rigid ball (Komuro et al., 1984) or a dry ice ball (Komuro, 1987) were used only in one occasion and subsequently ruled out. In this section we only consider the most common magma chamber analogues: the latex balloon and the silicone reservoir.

➢ **Latex Balloon**

The use of a balloon as magma chamber analogue imposes several restrictions. Possibly, the main limitation of this kind of "magma chambers" is that due to its elastic walls, it can be

deflated indefinitely, allowing the system to pass by different stages of collapse. This is not certainly the case of natural systems in which the withdrawal process can be interrupted at any instant if magma is unable to flow out. Furthermore, during doming processes the elastic walls permit an almost infinite expansion to geological improbable levels (Martí et al., 1994). In natural systems, once expansion has reached a specific level the tensile strength of the country rock goes over and an eruption can occur (Tait et al., 1989). The collapse and the doming structures can be overstated compared to natural ones. Some authors avoid these possible edge effects by stopping the experiment until the deformation is still realistic.

Furthermore, during the deflation process a water-filled balloon deforms in two different ways. Filled to its maximum capacity it deflates elastically and contracts due to overpressure decrease (Fig. 3.11 A). By contras, at lower water capacities, the roof subsided vertically as the water is evacuated (Fig. 3.11 B). Lavallée et al. (2004) proposed that these two mechanisms of analogue chamber deformation represent initially the elastic behaviour of the crust and the crystal mush around the chamber during contraction as the pressure in the magma chamber decreases. This is followed by brittle failure of the roof when the deviatoric stress reached the Mohr-Coulomb criterion curve.
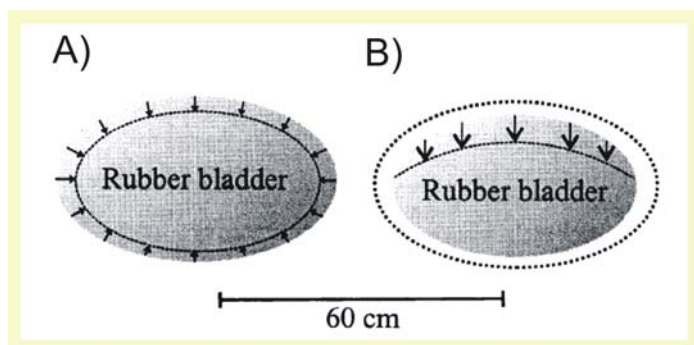
Fig.3.11: (A) Deformation of the bladder during initial withdrawal. The bladder contracts, similar in radial fashion. (B) Schematic representation of the bladder deformation at a later stage, where the roof subsides vertically. (Lavallée et al., 2004)

Moreover, the elastic walls of the balloon generate forces that do not have a counterpart in natural systems and, in consequence, violate the principles of scaling. Some authors (Lavallée et al., 2004) argued that the elastic walls can be interpreted as the boundary between the water and the sand and may represent the crystal-mush transition between the magma and the rock. However, the same authors admit that this boundary is not scaled and prevents physical processes such as intrusion and the collapse of blocks into the analogue magma chamber. In nature, such processes may affect the magmatic pressure and could play a role during the process of caldera formation.

Finally, some authors (e.g. Martí et al., 1994; Walter and Troll, 2001) buried the balloon close to one of the walls of the experimental tank. This layout is useful to observe the temporal evolution of the collapse but one could expect that this experimental set-up may alter the structures developed during the collapse process. Martí et al. (1994) evaluated the importance of this perturbation and considered that these edge effects are of second order.

➢ **Silicone reservoir**

The silicone reservoir as magma chamber analogue entails important restrictions. Probably, the major limitation is that the reservoir's walls are completely rigid. This would imply a rigid magma chamber. During the deflation process, i.e. the outflow of the silicone throughout the cylindrical reservoir (Roche et al., 2000) or the piston (e.g. Acocella et al., 2000, 2001a, 2001b, 2004), the lateral deformation of the analogue magma chamber is restricted due to the rigid walls of the tube or the piston. Evidently, this does not have a counterpart in nature. Besides, further important problem is to scale the silicone viscosity and to translate it into natural values. The extent to which the experimental results obtained with silicone reservoir models are applicable is limited by current knowledge of such natural parameters as viscosities, time-scales and strain rates (Merle and Vendeville, 1995; Acocella et al., 2000). Given the possible range of these values in nature, a single experiment might be associated with different equivalents in nature, characterized by diverse viscosities, time-scales and strain rates. The aim of the experiments is thus not to simulate a specific case, as the impossibility of determining its natural parameters would limit the applicability of the models (Acocella et al., 2000). The goal is rather to understand the overall mechanism of deformation, which might be valid for a wide range of natural cases.

❖ **EXISTENCE OF GRAIN FLOW PROCESSES**

All analogue experiments use granular materials (e.g. dry quartz sand, flour) to simulate country rock. Although these materials have the ability to deform in a brittle fashion and have a Mohr-Coulomb behaviour like natural rocks, they are also susceptible to slump and adjust by small scale grain flow processes. These processes lead to structures that may not have an analogy in natural rock systems, but some authors consider that these processes can be regarded as permanent plastic deformation (e.g.

Martí et al., 1994). This effect diminishes decreasing the grain size and increasing the cohesion of the material.

❖ IMPOSSIBILITY OF DIKE INJECTION

None of the experimental devices used up to now can simulate dike injection during the collapse or tumescence process. Only those experiments considering silicone as magma analogue could reproduce dike injection however, the high viscosity of the silicone and the granular nature of sand prohibit the intrusion of the silicone and the formation of "ring dikes" (Roche et al., 2000). The possibility of dike injection is important during magmatic processes because it can regulate the equilibrium inside the magma chamber. For example, in situations of overpressure, dike intrusion can decrease the magma chamber pressure and may avoid the initiation of an eruptive event.

❖ HOMOGENEOUS MAGMA CHAMBER ROOF

Analogue models have been carried out with homogenous roof above the magma chamber analogue. This is not a correct approximation to natural systems, since country rocks around magma chamber are normally heterogeneous in composition. Previous volcanic eruptions or sedimentation processes can establish above the magma chamber a roof with materials of very different physical properties such as pumice and basalt. Compositional heterogeneities can influence the stress field and consequently, fracture propagation and structure development. Therefore, it is important to introduce compositional heterogeneities in order to approach the analogue model, as much as possible, to reality.

❖ THERMAL EFFECTS

Furthermore, due to the experimental set-ups, none of the previously published analogue models of caldera collapse process takes into account thermal effects of the reservoir on the country rock and the eruption dynamics, although these factors may play

an important role. Thermal effects of the magmatic reservoir may alter the host rock rheology, creating a brittle-ductile transition zone between the liquid chamber and the solid host rock (Burov and Guillou-Frottier, 1999). Except some major faults or fractures, brittle structures will not penetrate inside this boundary, but structures at shallower levels are unaffected by the thermal effect. Normally, analogue models studies do not consider structures located close or in contact to the magma chamber analogue as realistic because the existence of the latex boundary. Consequently, since the thermal effects of the magma chamber are constrained to the material around the reservoir it does not affect our experimental results. However, future works may study the possibility of including thermal effects of the magmatic reservoir in order to improve existing experimental set-ups.

III.3 NEW ANALOGUE MODELS

III.3.1 Objectives

The new analogue models exposed in this work have several objectives. First, both experimental devices presented here should be able to reproduce some of the experiments set out in preceding studies. This offers the possibility to compare the obtained results with previous ones, verify the good working of the experimental set-ups and determine their restrictions. The aim of using two different experimental devices (those most common in prior studies) is to provide the differences in the results because the experimental set-ups and not due to the input parameters. This is possible carrying out the same experiment (same geometry and values in the input parameters) and comparing the obtained results. Furthermore, new variable will be introduced in some experiments hitherto not consider (e.g. compositional heterogeneities).

Another important objective of some of these new experiments is to describe the temporal evolution of faults at surface and at depth and to correlate the different stages of a caldera collapse with the volume of "magma" (analogue material) withdrawn from the analogue magma chamber. The results will be compared with already published numerical estimations.

The final goal of all these "new" analogue models is to establish the general features of caldera collapse formation in order to use them in the design of mathematical models.

III.3.2 Experimental method

III.3.2.1 Experimental devices and procedure

The experiments have been carried out in two different experimental devices. Both of them consist of a tank filled with dry quartz sand (host rock analogue) with the magma chamber analogue buried at a certain depth. The main difference between them is the analogue material used for simulating the magma chamber.

In the experimental set-up I, a water-filled latex balloon emulates the magmatic reservoir. Depending on the experiment, the balloon is located in the centre of a wood tank (100 × 100 × 20 cm) (Fig. 3.12 A) or at a lateral wall of a transparent glass tank (60 × 60 × 40 cm) that allows the observation of the temporal evolution of the caldera collapse process (Fig. 3.12 B). Magma withdrawal is simulated using a tube attached to the balloon. When the tube is unblocked, water simply flows out through it and the balloon deflates gradually leading to a collapse of the overlying structure. In the case of experimental set-up II, a silicone reservoir is located in the centre of a wood tank (100 × 100 × 20 cm) (Fig 3.12 C). The silicone is placed in a cylindrical reservoir of 10 cm of diameter connected to an outflow tube. In all experiments the level of silicone in the open tube and in the apparatus is the same. The excess of weight of the overlying sand pack causes the subsidence.

In order to study the internal structure and fault development, thin coloured layers of analogue material are placed at intervals of 1-2 cm within the white analogue material. Both materials have indistinguishable physical properties. Furthermore, the temporal evolution of the collapse process is monitored using a video camera centred above or in front of the apparatus. Finally, after each experiment, the model is covered with sand to preserve the depression and other surface structures. Afterwards, the model is saturated with water and sectioned.

III.3.2.2 Analogue materials properties

Analogue materials have been selected taking into account that their physical properties have to fulfil the scaling requirements presented in section III.3.3. The physical properties of the materials used in our experiments are summarized in Table 3.2. Well-sorted dry quartz sand follows, similar to natural rocks, the Mohr-Coulomb brittle failure criterion. For this reason, it is considered a good analogue for brittle crust (Krantz, 1991). Additionally, in some experiments, a compound of dry quartz sand and fused alumina is used to simulate "rock compositional heterogeneities". Fused alumina has similar physical properties and mechanical behaviour as quartz sand. In those experiments where both materials are applied, the dry quartz sand represents low dense volcanic rocks and the compound denser ones (e.g. basalts).

Furthermore, the applied silicone putty is a Newtonian fluid with a viscosity of 5×10^4 Pa. Its density is 970 kg/m^3 and its applicability in analogue models is widespread (ten Grotenhuis et al., 2002). Physical properties of silicone may vary depending on applied polymer (Table 3.1).

MATERIAL	(mean diameter)	Density (uncompacted)	Friction angle (ϕ)	Cohesion (C)	Viscosity
Quartz sand	~40 μm	1270 kg/m^3	~ 37º	250 Pa	_____
Fused alumina	~54 μm	2010 kg/m^3	38º	200 Pa	_____
Compound $V_{sand}/V_{alumina}=1,03$	~50 μm	1640 kg/m^3	~ 37º	~240 Pa	_____
Silicone putty	_____	970 kg/m^3	_____	_____	5×10^4 Pa

Table 3.2: Principal characteristics of the analogue materials used in this study.
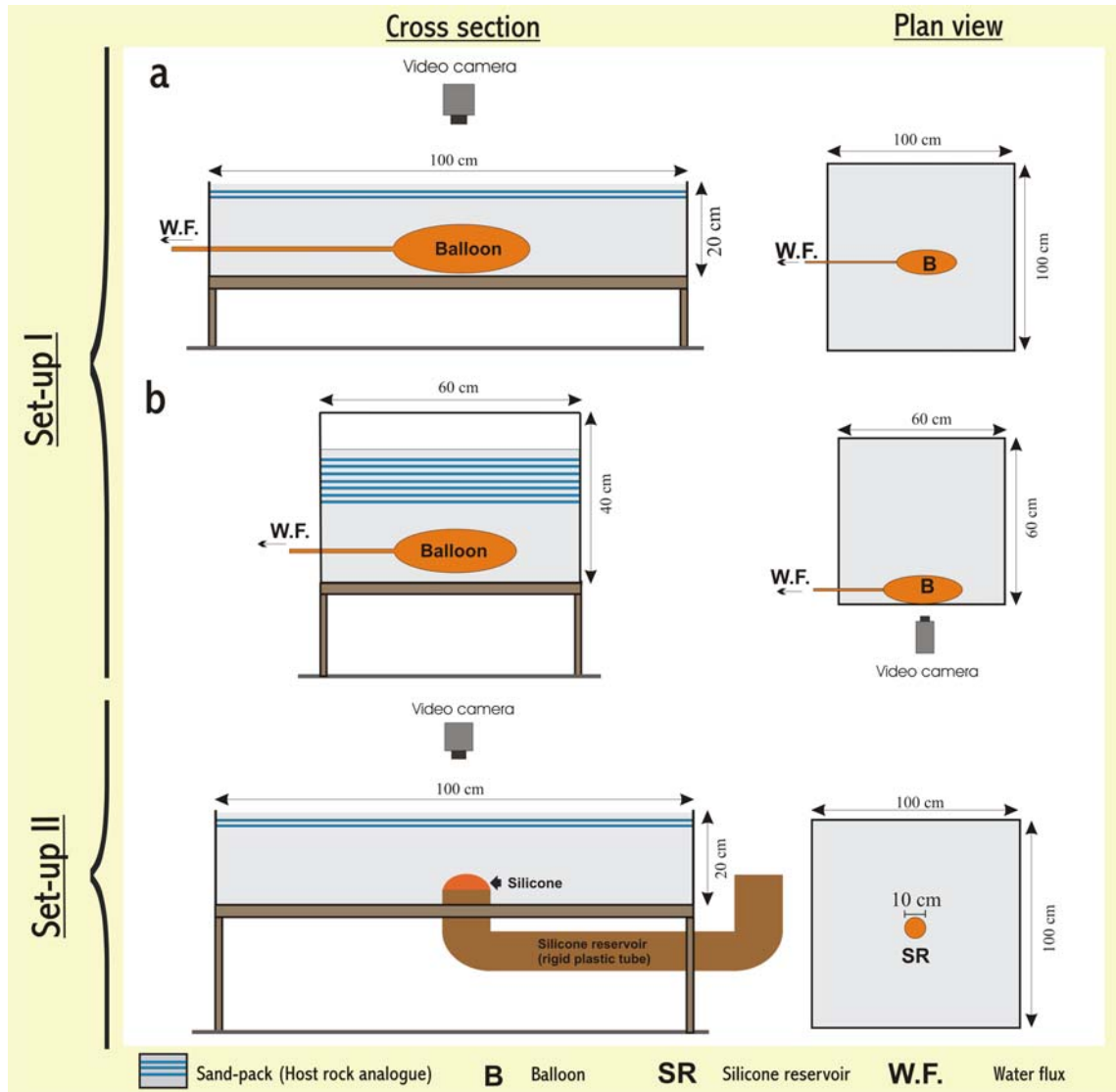
Fig.3.12: Sketches of the experimental devices used in this work. Experimental set-up I with the balloon (magma chamber analogue) located at the centre or the lateral of the wood or glass tank, respectively. Experimental set-up II, the silicone reservoir (magma chamber analogue) is located at the centre of the wood tank (100 x 100 x 20 cm).

III.3.3. Scaling: principles and methods

II.3.3.1 Principles of scaling:

Correct scaling of analogue models is not trivial. Analogue models have to fulfil three important requirements (Hubbert, 1937):

➢   **Geometrical similarity:** An analogue model is said to be geometrically similar to nature when all corresponding lengths are proportional and all angles present in nature are preserved equal at the model.

➢   **Kinematic similarity:** An analogue model is said to be kinematically similar to nature when provided the time required for any change in the one is proportional to that required for the corresponding change in the other.

➢   **Dynamical similarity:** An analogue model is said to be dynamically similar to nature when for every force F_i acting on an element of mass dm_i which a volume dV_i of the natural model there is a corresponding vector force F_j with the same orientation as F_i and the ratio of the magnitudes of the two forces being: $F_j / F_i = \phi$, where ϕ is constant for every pair of forces F_i and F_j. It can be said that, for each element of mass dm_j occupying volume dV_j of the model the forces acting are such that the motion is geometrically and kinematically similar to the corresponding motion of the element of mass dm_i in volume dV_i of nature.

The correct scaling of analogue models can be carried out through two possible methods. The first one follows the considerations of Hubbert (1937) and Sanford (1959) and is based on the ratios of physical parameters. Another possibility is to apply the Buckingham-Π theorem, involving dimensionless numbers, which should maintain a constant value in the natural and in the experimental system (Middleton and Wilcock, 1994; Merle and Borgia, 1996).

III.3.3.2 Scaling methods

<u>III.3.3.2.1 Scaling based on physical parameters ratios</u>

The definition of ratios among physical parameters is a possible way to check if an analogue model verifies these requirements. Analogue experiments are scaled considering that for each key physical parameter X it is possible to define a ratio $\mathbf{X^*}$:

$$\mathrm{X^*} \equiv \frac{\mathrm{X_{model}}}{\mathrm{X_{nature}}} \qquad [3.1]$$

In particular, our analogue models involve six different ratios: length ratio ($\boldsymbol{L^*}$), density ratio (ρ^*), gravitational acceleration ratio ($\boldsymbol{g^*}$), stress ratio (σ^*), time ratio ($\boldsymbol{t^*}$) and viscosity ratio ($\boldsymbol{v^*}$); being only three of them independent.

➢ $\mathbf{L^*}$ (Length ratio)

The value of the length ratio $\boldsymbol{L^*}$ is determined by the size of the experimental device and the dimensions of natural systems. Collapse calderas may have diameters up to hundred kilometres (e.g. Smith, 1979; Spera and Crisp, 1981; Lipman, 1984; Newhall and Dzurisin, 1988) whereas the characteristic dimensions of the experimental tanks are 100 × 100 × 20 cm (wood tank) and 60 × 60 × 40 cm (glass tank). Consequently, the value of $\boldsymbol{L^*}$ ranges from 10^{-5} to 2×10^{-5}, i.e. 1cm in the experiments corresponds to 0.5 - 1 km in nature. In order to have geometric similarity, we choose dimensions and positions of the balloon consistent with this value of $\boldsymbol{L^*}$. In addition, all the angles in the analogue models have to be as close as possible to those of the natural systems. Note that the similarity of angles affects not only the geometry but also a physical property of the material like the angle of internal friction. In this case, the angle of internal friction ϕ of dry quartz sand is ~35°- 37° (Krantz, 1991; Acocella et al., 2001a; Acocella et al., 2004), a value in the range of natural values.

➢ ρ^* (Density ratio)

The density ratio ρ^* depends on the selected analogue material. The densities of our well-sorted dry quartz sand and our silicone putty are 1270 kg/m³ and 980 kg/m³, respectively. Assuming a representative value of 2500 kg/m³ for density of upper crust rocks, the density ratio results $\rho^* = 0.4 - 0.5$.

➢ g^* (Gravitational acceleration ratio)

The gravity ratio is simply $g^* = 1$ because analogue models also run under the Earth's gravity field.

➢ σ^* (Stresses ratio)

The stress and time ratios can be derived from the above values making use of dimensional analysis. It yields $\sigma^* = \rho^* g^* L^* \approx 0.5 \times 10^{-5} - 10^{-5}$. Dynamic similarity requires therefore that any property of the analogue material having units of stress have to scale the natural rocks with this value of σ^* (Hubbert, 1937). For instance, since natural rocks have a cohesion c of around 10-50 MPa (e.g. Martí et al., 1994), the rock analogue material should have a cohesion in the range of 50-500 Pa in order to guarantee a correct scaling. In order to estimate the cohesion of our granular material we applied a method suggested by Roche et al. (2001) and described in civil engineering (Philipponat and Hubert, 1997). The cohesion of the granular material is calculated from the maximum, or critical, height of a vertical cliff that can be dug before it collapses. The cohesion is given by the following equation (Roche et al., 2001):

$$c = \frac{\rho g CH}{3.85 \tan\left(\dfrac{\pi}{4} + \dfrac{\phi}{2}\right)} \qquad\qquad [3.2]$$

where ρ is the sand density, g the gravitational acceleration, CH the critical height of the cliff and ϕ is the angle of internal friction of sand. The cliffs are created by applying a differential horizontal motions between two plates previously placed beneath the material. With our sand, the highest

cliffs obtained were 6 - 7 cm, which correspond to a cohesion of 230 - 270 Pa. The dry quartz sand has cohesion close to 250 Pa and, in consequence, verifies dynamic similarity.

> ### t^* (Time ratio)

Finally, the time ratio yields $t^* = \sqrt{L^*/g^*} \approx 3\times10^{-3} - 4.5\times10^{-3}$. It constrains the duration of the experiments in order to verify kinematic similarity. Considering these values of time ratio and that our balloon experiments last between 60 and 350 s and the silicone ones between 60 and 180 min, these analogue experiments reproduce caldera collapses with durations between 10 and 32 h or between 10 and 39 days. The duration of the collapse process is poorly constrained, but values from few hours (Wolfe and Hoblitt, 1996) to few days (Wilson and Hildreth, 1997) are generally accepted (Lavallée et al., 2004). Consequently, balloon experiments are also correctly scaled in time. By contrast, some silicone experiments are too long. Although, time for this experimental device is not properly scaled, that is irrelevant since the deformation of Coulomb materials like the dry quartz sand is rate-independent.

> ### ν^* (Viscosity ratio)

The viscosity ratio is defined as: $\nu^* = t^*\sigma^*$. Considering the values of t^* and σ^*, the range of the viscosity ratio yields: 1.6×10^{-8} to 4.5×10^{-8}. Since magma viscosity presents a broad spectrum of values, from few hundreds of Pa s up to 10^{13} Pa s (Hess and Dingwell, 1996), it is easy to find the correct analogue material. The silicone used in the experimental device III ($\nu=5\times10^4$ Pa s) represents magmas with a viscosity between 1.1×10^{12} and 3.1×10^{12} Pa s. These are high values, but still lay in the interval of the natural ones. The use of a high viscous silicone increases the duration of the experiment but do not affect the geometry of faults.

III.3.3.2.2 Scaling based on the Buckingham-Π theorem

The second method of scaling involves application is based on the Buckingham-Π theorem (Middleton and Wilcock, 1994). The theorem states that: *"Any dimensionally homogeneous equation involving certain physical variables can be reduced to an equivalent equation involving a complete set of dimensionless products"*. Therefore,

given **n** principal variables **v** which control a physical phenomenon it is possible to find a kind of functional relationship Ψ between them. Written formally:

$$\Psi\ (v_1,\ ....,\ v_i,\ .....,v_n)=0.$$ [3.3]

The obtaining of this relationship is based on the idea that it is possible to rearrange the variables to form dimensionless combinations (products). A set of such dimensionless products is said to be "complete" if each product in the set is independent of the others. It means that any product inside the group can be expressed as a product of the others in the set, and any other dimensionless product outside the group can be expressed as a product of the dimensionless products in the set (Middleton and Wilcock, 1994).

A consequence of the Buckingham-Π theorem is that**,** existing **n** original variables involving **m** dimensions, it is generally possible to reduce the relationship to a function of **n-m** dimensionless products (Middleton and Wilcock, 1994).

In order to scale analogue models, it is assumed that a caldera collapse can be expressed as a functional relationship Ψ**.** Because the equation is dimensionless, it is true whatever the scale that (Middleton and Wilcock, 1994):

$$\Psi_{\mathbf{nature}} = \Psi_{\mathbf{model}}$$ [3.4]

The Π-numbers required for a correct scaling depend on the number of principal variables involved in the system, varying from an experimental device to another. For this reason they will be explained separately for balloon and silicone models in the corresponding sections.

III.3.4 Balloon models

III.3.4.1 Type of experiments: Design and input parameters

Five different experimental designs have been performed with set-up I (latex balloon as magma chamber analogue (Fig. 3.13). These designs can be divided in two

groups. In the first one (Fig. 3.13 A-C), the balloon is located in the centre of the wood tank (set-up I a), whereas in the second one (Fig. 3.13 D-E), the magma chamber analogue is buried close to one of the glass tank walls (set-up I b).

➢ **Experiments with the magma chamber analogue located at the centre of the wood tank**

-Pure collapse without topography   **(A-type)**

-Pure collapse with homogeneous topography   **(B-type)**

-Pure collapse with heterogeneous topography   **(C-type)**

➢ **Experiments with the magma chamber analogue located at a lateral wall of the glass tank**

-Pure collapse without topography   **(D-type)**

-Pure collapse with homogeneous topography   **(E-type)**

The principal aim of the first set of experiments is to study the structural features of a caldera collapse. Furthermore, A-type experiments (Fig. 3.13 A) are addressed to investigate the influence on the caldera collapse of the roof aspect ratio R and the shape of the balloon (magma chamber analogue) and are decisive to control possible experimental errors, limitations and restrictions. B-type experiments study the effects of topography (volcanic edifice) above the magma chamber. C-type experiments investigate the influence of compositional heterogeneities inside this edifice, introducing in its interior a second one of higher density.

The second set of experiments is decisive to describe and observe the evolution with time of the collapse process without topography and varying the roof aspect ratio (D-type experiments), and with topography (E-type experiments).

A total of 25 balloon experiments have been carried out (Table 3.3), 7 A-type, 8 B-type, 2 C-type, 7 D-type and 1 E-type.
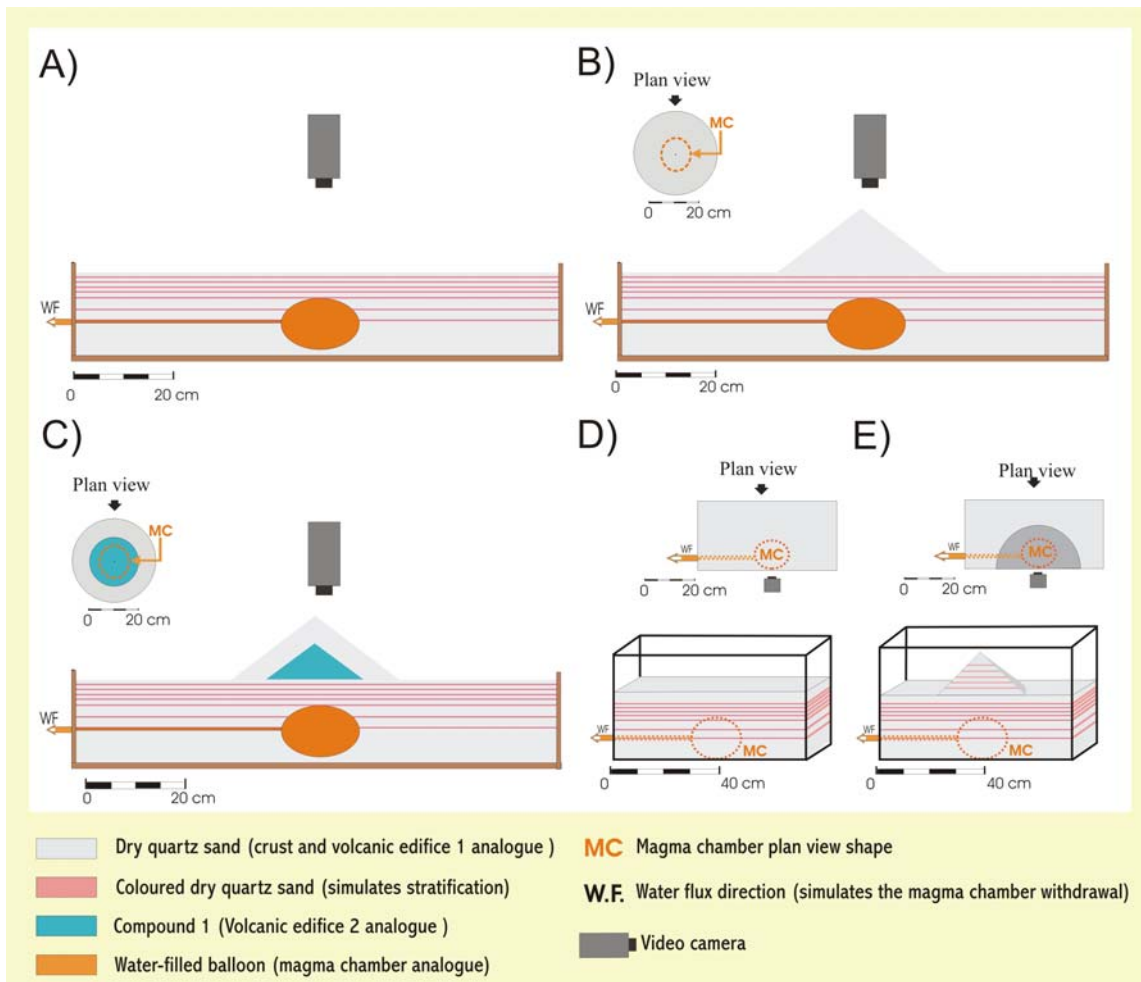
Fig. 3.13: Sketch of the five experimental designs carried out. **(A)** A-type experiments; **(B)** B-type experiments; **(C)** C-type experiments; **(D)** D-type experiments; **(E)** E-type experiments.

Experiments	INPUT PARAMETERS									
	P (cm)	R	H (cm)	D_{max} (cm)	D_{min} (cm)	t (s)	% V	He_1 (cm) / He_2 (cm)	α / β	Ra_1 (cm) / Ra_2 (cm)
A-1	3	0.28	8.0	15.5	8	105	100	/	/	/
A-2	4	0.3	12	14	13	60	60	/	/	/
A-3	5	0.35	11	15.5	13	60	70	/	/	/
A-4	4.5	0.38	8.5	18.5	8.7	85	70	/	/	/
A-5	5	0.39	10.5	13.5	12	60	75	/	/	/
A-6	9	0.44	14	22	19	350	100	/	/	/
A-7	7.5	0.64	8.5	18.5	8.5	60	62	/	/	/
B-1	4	0.96	12	14	13	60	72	9	43º	6.5
B-2	2.5	1.06	8.5	13.5	9	120	100	9	43º	6.5
B-3	5	1.06	12	13.5	13	70	87	9	43º	6.5
B-4	5	1.13	12	13.5	13	60	70	10	45º	10
B-5	4.1	1.8	6.7	8	6.7	180	100	9	43º	6.5
B-6	4.3	1.84	6.3	8	6.6	90	100	9	43º	6.5
B-7	5.8	2.24	4.2	12.5	4.5	60	100	9	43º	6.5
B-8	5.5	2.24	4.5	10	4.8	180	100	9	43º	6.5
C-1	5	1.27	11	15.5	13	60	70	13 / 7.4	37º / 37º	17 / 10
C-2	5	1.42	10.5	13.5	12	60	77	13 / 7.4	37º / 37º	17 / 10
D-1	6	0.34	14	20	16	160	50	/	/	/
D-2	5.7	0.41	14.3	15.2	13	60	100	/	/	/
D-3	9.3	0.48	13	20	18.5	330	100	/	/	/
D-4	12.5	0.52	15.5	25	23	290	64	/	/	/
D-5	17.5	0.84	15	22	20	310	86	/	/	/
D-6	17.9	1.14	13	16	15.5	250	76	/	/	/
D-7	25.7	2.34	11	13	9.5	240	100	/	/	/
E-1	3.9	n.c	11.3	12.5	n.c	60	100	11	33º	17

Table 3.3: List of the experiments carried out with a water-filled balloon as magma chamber analogue. Definitions of the different variables are summed up in Table 3.5. The letters before the experiment number indicate the type of experiment corresponding with Figure 3.19. α Slope of the volcanic cone 1; β Slope of the volcanic cone 2; D_{max} Balloon maximum diameter; D_{min} Balloon minimum diameter; **H** Balloon height; He_1 Volcanic cone height; He_2 Height of the volcanic cone 2; **n.c.** No calculable or measurable value due to experimental reasons or visual problems; **R** Roof aspect ratio defined as R= $[(P+He1)(D_{max}+D_{min})]/2D_{max}D_{min}$ (Roche and Druitt, 2001); Ra_1 Radius of the volcanic cone 1; Ra_2 Radius of the volcanic cone 2; **t** Duration of the experiment; **P** Balloon depth; **V** Total volume of water extruded from the balloon.

III.3.4.2 Complementary scaling: Determination of the suitable Π-numbers

Considering all type of experiments carried out with a balloon as magma chamber analogue (Fig. 3.13), it is possible to establish a total of 18 variables and three different dimensions (L: Length, M: Mass, T: Time) (Table 3.4). For some of them it is difficult or almost impossible to constrain or determine their natural values (e.g. β, He_2…). Therefore, these variables are useless for a correct scaling. In order to scale properly these analogue experiments only 13 of all the variables are considered as "principal" and involved in the scaling procedure. Therefore, according to the Buckingham-Π theorem, 10 independent dimensionless Π-numbers are needed to guarantee similarity. The analogue model is correctly scaled when these dimensionless numbers maintain the same value in nature as well as in the experimental systems.

	Variable & definition	Experimental value	Natural value	Dimensions	References	Experiments without topography (A- and D-type)	Experiments with homogeneous topography (B- and E-type)	Experiments with heterogeneous topography (C-type)
P	"Magma chamber" depth (balloon depth)	2×10^{-2}- 25×10^{-2}m	$\sim 3\times10^3$ –10^4m	[L]	[15,71,193, 198,327, 383]			
H	"Magma chamber" height (balloon height)	4.2×10^{-2}- 15×10^{-2}m	5×10^2- 2×10^3 m	[L]	[281]			
D	"Magma chamber" diameter (balloon diameter)	4.5×10^{-2}- 25×10^{-2}m	$\sim 1.5\times10^3$-10^5m	[L]	[146,147,193, 198,237,325, 327,368]			
ρ_s	"Host rock" density (sand density)	1270 kg/m³	2500-2800 kg/m³	[M L⁻³]	[2]			
φ	Internal friction angle of sand	37°	20-40°	-	[279]			
t	Duration of the experiment	60-350 s	9-98 h	[T]	[185]			
g	Gravity	9,81 m/s²	9,81 m/s²	[M T⁻²]	---			
He_1	"Volcanic cone 1" height	9×10^{-2}- 13×10^{-2}m	$\sim1.2\times10^3$-30×10^3 m	[L]	[2]			
α	"Volcanic cone 1" slope	33-43°	n.d.	-	-			
Ra_1	"Volcanic cone 1" radius	6.5×10^{-2}- 17×10^{-2}m	$\sim5\times10^3$-20×10^3 m	[L]	[2]			
ρ1	"Volcanic cone 1" density	1270 kg/m³	2200-2900 kg/m³	[M L⁻³]	[2]			
φ1	"Volcanic cone 1" internal friction angle	37°	20-40°	-	[279]			
He_2	"Volcanic cone 2" height	7.4×10^{-2}m	n.d.	[L]				
β	"Volcanic cone 2" slope	33-43°	n.d.	-				
Ra_2	"Volcanic cone 2" radius	10×10^{-2}m	n.d.	[L]				
ρ2	"Volcanic cone 2" density	1640 kg/m³	2900-3200 kg/m³	[M L⁻³]	[2]			
φ2	"Volcanic cone 2" internal friction angle	37°	20-40°	-	[279]			

Table 3.4: Variables relevant in the analogue models with a water-filled balloon as magma chamber analogue. Those coloured in blue are considered as "principal" and important for a correct scaling of the geological process of caldera collapse. **n.d.** Not determinable

Table 3.5 lists the values in experiments and in nature of the 10 Π-numbers necessary for scaling the models. Their comparison shows very close values for Π_1, Π_2, Π_7, Π_8, Π_9 and Π_{10}. By contrast, Π_3 (**D/H**) defined as the ellipticity (*e*) of the magma chamber in cross section has smaller values in the experiments (1.06 - 2.98) than in nature (8 - 40). In the experiments are considered almost spherical (e.g. D-2, *e* = 1.08) to slightly ellipsoidal (e.g. B–7, *e* = 2.98) magma chambers, whereas the natural examples correspond to sill-like reservoir. Therefore, experimental values for Π_3 are not necessarily wrong because it is accepted that magma chamber can be almost spherical (*e* = 1), especially smaller ones. The principal problem is the lack of information about the height of magma chambers, being in the natural examples scarce.

Π–Numbers	Experimental values	Natural values	Natural examples	Experiments without topography (A- and D-type)	Experiments with homogeneous topography	Experiments with heterogeneous topography (C-type)
Π_1= P/D	0.19-2.71	0.1-3.2[272]	Aira: 0.2 [15,198,322] Ishizuki: 0.73 [383] Rabaul: 0.4-1 [167,238,251]			
Π_2=ϕ	37°	20-40°	------------------------------			
Π_3=D/H	1.06-2.98	8-40[114]	Aira: 30-40 [116,280] Crater Lake: 8 [116,280] Long Valley 14 [116,280]			
Π_4= P/gt^2	~10^{-5}-10^{-6}	~10^{-10}-10^{-13}	------------------------------			
Π_5= Ra$_1$/D	0.48-1.4					
Π_6= He$_1$/D	0.65-1.88					
Π_7= ϕ1	37°	20-40°	------------------------------			
Π_8 =ρ1/ρa	1	0.8-1.2	Tenerife: 1 [2]			
Π_9 = ρ2/ρa	0.77	1-1.3	Tenerife: 1.3 [2]			
Π_{10}= ϕ2	37°	20-40°	------------------------------			

Table 3.5: Values of the Π dimensionless numbers in experiments and in nature. Numbers in square brackets indicate the data source of the natural examples.

III.3.4.3 Results

III.3.4.3.1 Estimate of the critical value of R

Prior to the description of the results obtained it is necessary to reintroduce here the definition of roof aspect ratio **R** already commented in section II.3.7.2.2, as well as the designation of the limits between supercritical (high), critical (moderate) and

subcritical (low) aspect ratio. Remember that two-dimensional studies in mining subsidence distinguish these three cases (supercritical, critical and subcritical) of collapse depending on the roof aspect ratio **R** defined as the quotient between the roof thickness (depth) **h** and the roof width *w* (see section II.3.7.2.2 for more details). The cited authors (Whittaker and Reddish, 1989) establish that the critical value for **R** considering an angle of draw θ equal to $\approx 35º$ is 0.7. Consequently, they assume a subcritical case if **R** >0.7, a critical case if **R** =0.7 and a supercritical case if **R** <0.7. Despite the calculated critical value for **R** is 0.7, Whittaker and Reddish (1989) proposed critical value for **R** in the range of 0.7 to 0.83, and in some cases even 0.87. In fact, the value of the angle of draw is dependent on the depth on the roof thickness (depth) and on the material (Whittaker and Reddish, 1989). For example, Roche et al., (2000) observed the transition from subcritical to supercritical at an aspect ratio 1 and Roche and Druitt (2001) in the range of 1-1.4. Beside, our experiments show a transition from coherent to non-coherent collapse at **R** $\approx$ 0.7. Such discrepancies between our results and those of Roche et al. (2000) and Roche and Druitt (2001) may be due to following reasons. On the one hand, experiments performed by Roche et al. (2000) do not cover the whole range of R values, then they pass from **R** = 0.5 to 1. Therefore, in the case that the critical value is within this interval they would not be able to detect it. Furthermore, following the indications of mining studies we have measure the angle of draw in Roche et al. (2000) experiments in order to redefine the critical **R** value. The angle of draw is not a constant value, it depends on the roof thickness and on the roof material. Furthermore, it is also logical to think that the experimental set-up (silicone reservoir or latex balloon) may have a certain influence. The case is that in Roche et al. (2000) the angle of draw varies from 25º to 35º (see Figures 5, 6, 10 in Roche et al., 2000) this results in a critical value of **R** from 0.7 to 1.0. Therefore, it is quite plausible that the authors concluded that the transition from a subcritical (coherent collapse) to a supercritical (non-coherent collapse) regime is at **R** = 1. Since their experiments do not cover all possible ranges for R this is only an approximated value. By contrast, in our experiment the angle of draw has an average value of 32.5º . It implies that we should find a change in the subsidence regime at approximately **R** = 0.78. Additionally, Roche and Druitt (2001) proposed that the critical **R** is in the range between 1 and 1.4. This interval is an analytical solution and do not come from experimental data. Furthermore, the authors themselves admit that there exist some discrepancies between the analytical solution and the experimental results, especially for **R** values lower than 0.7.

250

Summarizing, when defining the critical R our experimental results are in agreement with previous mining studies (Whittaker and Reddish, 1989) but there exists some discrepancies between previous works (Roche et al., 2000; Roche and Druitt, 2001). These may have their origin in the accuracy of previous experiments, the host rock analogue material and the experimental set-up. Concluding, although our experimental results indicate a transition at **R** $\approx$ 0.7 we accept that this value may be broadened to 0.85.

III.3.4.3.2 Measured and calculated values

In this section we sum up the most relevant information obtained with each performed balloon analogue model (Table 3.6).

Exp.				MEASURED AND CALCULATED VALUES						
	R	S_p (cm)	S_s (cm)	$P\text{-}D_p$ (cm)	$P\text{-}D_{smax}$ (cm)	$P\text{-}D_{smin}$ (cm)	$OL\text{-}D_{max}$ (cm)	$OL\text{-}D_{min}$ (cm)	$N\text{-}D_{max}$ (cm)	$N\text{-}D_{min}$ (cm)
A-1	0.28	n.c	4-6	15.4	14.5	8	17	12	8.3	3.7
A-2	0.3	n.c	5	n.c.	15	13	23	21.5	7.4	6.8
A-3	0.35	2.3	2.4	13.5	14.8	13	26.5	23	7.2	4.6
A-4	0.38	n.c	3.4	17.8	14	12	19.9	17.38	n.c.	n.c.
A-5	0.39	4	3.8	13.2	14	12	27	22	11	8
A-6	0.44	n.c	6.5	n.c.	25.5	25.5	48	44	15	14
	0.64	2-3.4	2.5-3	18.3	14.5	10	20	15.5	n.c.	n.c.
B-1	0.96	4.2	n.c	13.5	14	13.4	27.65	27.65	13.7	13.7
B-2	1.1	3.4	2.1	13.4	12	12	n.c.	n.c.	n.c.	n.c.
B-3	1.06	4.1	n.c.	13.4	14.3	12.4	n.c.	n.c.	n.c.	n.c.
B-4	1.13	2.5-3.7	2.3	14.2	13.5	11	35.6	35.6	12.25	12.25
B-5	1.8	n.c.	n.c.	n.c.	n.c.	n.c.	n.c.	n.c.	n.c.	n.c.
B-6	1.84	n.c	n.c.	n.c.	9.2	9.2	n.c.	n.c.	n.c.	n.c.
B-7	2.24	0.7	n.c.	n.c.	10.8	10.8	n.c.	n.c.	n.c.	n.c.
B-8	2.24	1.1	0.5	n.c.	9.6	9.6	n.c.	n.c.	n.c.	n.c.
C-1	1.27	3.6	2.3	13.5	15	15	n.c	n.c	n.c	n.c
C-2	1.42	n.c	3.4	13	13.5	12.8	n.c	n.c	n.c	n.c
D-1	0.34	n.c.	n.c.	n.c.	18	16.5	31.5	27.5	15	12.5
D-2	0.41	n.c.	n.c.	n.c.	18.5	16	31.5	29	10.5	9
D-3	0.48	n.c.	n.c.	n.c.	25.5	22	49.5	48	15	13
	0.52	n.c.	n.c.	n.c.	31	27	61.3	57.9	18	15
D-5	0.84	n.c.	n.c.	n.c.	22	21	57	55	17.5	13.5
	1.14	n.c.	n.c.	n.c.	20	17.9	56.6	48.7	12	9.5
D-7	2.34	n.c.	n.c.	n.c.	13.5	12.5	46	42	8	5.5
E-1	n.c.	n.c.	n.c.	n.c.	n.c.	n.c.	n.c.	n.c.	n.c.	n.c.

Table 3.6: Relevant measured or calculated parameters in balloon analogue models. **n.c.** No calculable or measurable value due to experimental reasons or visual problems; **N-D$_{max}$** Maximum diameter of the non-deformed area; **N-D$_{min}$** Minimum diameter of the non-deformed area; **OL-D$_{max}$** Maximum diameter of the outer limit of the collapse; **OL-D$_{min}$** Minimum diameter of the outer limit of the collapse; **P-D$_p$** piston diameter at depth; **P-D$_{smax}$** Maximum piston diameter at surface; **P-D$_{smin}$** Minimum piston diameter at surface; **S$_p$** subsidence at depth; **S$_s$** subsidence at surface.

III.3.4.3.3 Pure collapse without topography (A- and D-type experiments)

➢   Piston diameters at depth (D_p) are, considering experimental errors, similar to the magma chamber diameters of the corresponding experiments. Furthermore, piston diameters at surface (D_s) are generally lower or similar to D_p values. Both observations indicate that faults delimiting the subsiding block are vertical or outward dipping with high slope angle.

➢   Plane view observations at surface allow to define two different regions for any value of **R** (Fig. 3.14): a non-deformed central area (**N**) and an annular zone of flexure and extension encircling the former (**EXT**). This external extensional region can be subdivided, in turn, into a zone where strata are tilted towards the depression (**T**) and a horizontal area with extensive surface fractures (**E**).
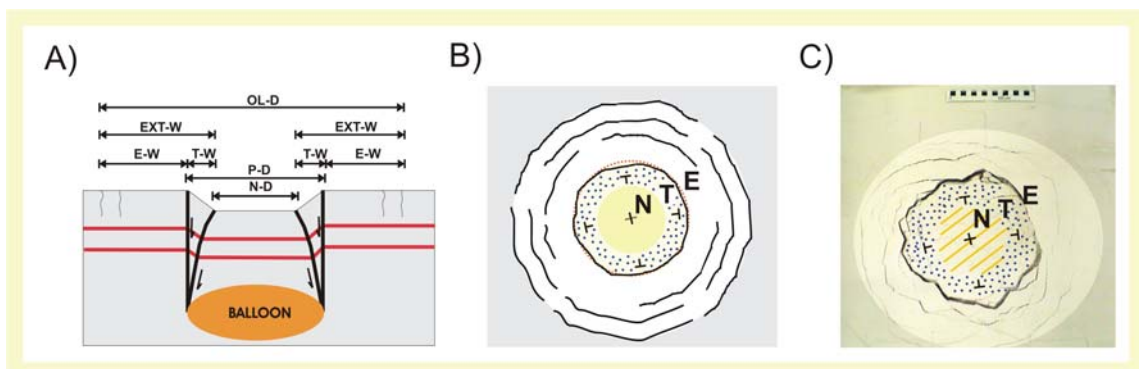

Fig. 3.14: Structural parts of a caldera collapse with a balloon as magma chamber analogue. **(A)** Sketch in cross section of a caldera collapse without topography and low **R** value. **(B)** Sketch in plan view of the same collapse as in A). Red dotted line corresponds to the plan view shape of the magma chamber. Yellow colour corresponds to the non-deformed area **N**, blue dots to the tilted area **T** and white colour to the extensional zone **E**. **(C)** Photograph of experiment A-6 with the three different parts. **E** Extensional zone; **E-W** Width of the extensional zone; **EXT-W** (EXT-W=E-W + T-W) Width of the external area of flexure and extension; **N** Non-deformed area; **N-D** Non-deformed area diameter; **OL-D** Structural limit diameter; **P-D** Piston diameter; **T** Tilted area; **T-W** Width of the tilted area.

➢   For low aspect ratios (**R** < 0.7 - 0.85), the collapse is piston-like with a non-deformed central area (Fig. 3.15). The subsiding piston is bounded by circular, vertical or sub-vertical (90°-70°) ring-faults (**RF**) that dip slightly outwards or inwards. In some cases, the fault dip angle is not constant but decreases towards the surface. A second internal group of reverse faults dip outwards with angles between 40° and 70°. These "bell-

shaped" faults (**BF**) appear at depth and some of them may not reach the surface (Fig. 3.15)

➢　　　　For high aspect ratios (**R** > 0.7 - 0.85), the collapse does not occur as a coherent block. Multiple ring faults slice the subsiding block into a series of cones and the initial reverse faults no longer reach the surface. Furthermore, the annular extensional zone dominates the depression. The higher the ratio **R**, the larger the number of faults.
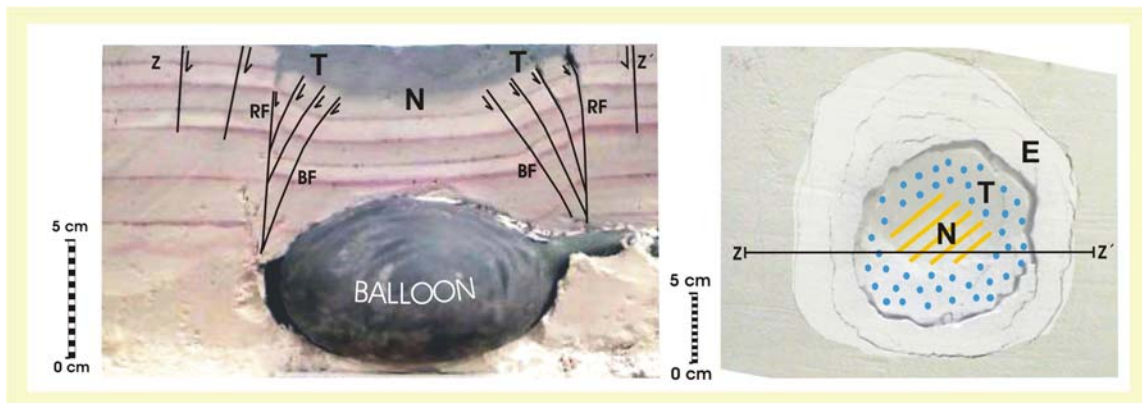

Fig. 3.15: Photographs of experiment A-3. **(A)** Cross-section of experiment A-3. **(B)** Plan view of experiment A-3. **BF** "Bell-shaped" faults; **E** Extensional zone; **N** Non-deformed area; **RF** Ring-fault; **T** Tilted area.

➢　　　　Temporal evolution

Caldera collapse is a continuous process that evolves through the appearance of certain sets of fractures and faults. Therefore, we cannot consider the formation of these distinctive sets of brittle features as discrete events in a continuous caldera-forming process. Their appearance and development is intimately related to the decompression of the magma chamber, which will determine the different phases of a caldera collapse process.

On the one hand, Figure 3.16 shows the evolution of the collapse at surface from the beginning of the experiment until the complete withdrawal of the balloon. Additionally, Figures 3.17, 3.18, and 3.19 illustrate a sequence of shots that reproduce the process of collapse for experiments D-1, D-3 and D-5, respectively. These experiments are, in that order, good representatives of low (**R** = 0.34), moderate (**R** =0.54) and high (**R** = 2.34) roof aspect ratio models. The onset of caldera collapse is characterized by the appearance of surface fractures (**SF**) in the extensional area and the initiation of subsidence (Fig. 3.16 indication A, Fig. 3.17 and Figs.

3.18 A, 3.19 A and 3.20 A). As subsidence continues by surface down flexure, these fractures propagate around the depression, fusing together to form a complete ring fracture or just intersecting at low angles (Figs. 3.16 and 3.17). Simultaneously, the first set of "bell-shaped" faults (BSF) nucleates at depth (Figs. 3.18 B, 3.19 B and 3.20 B). As the process goes on, further ground deformation occurs due to flexure and new extensional fractures develop at surface towards the central area. Concurrently, the outward dipping "bell-shaped" reverse faults propagate upwards (Fig. 3.18 C and 3.19 C). At high aspect ratios (R >0.7 - 0.85) the temporal evolution varies in comparison to that of experiments at low aspect ratio. The principal difference is the number of reverse faults taking place in the collapse. For high chamber aspect ratios, the development of these faults triggers the formation of new structures that progressively nucleate at shallower depths to break the roof in a series of cones as illustrated in Figure 3.20 C. Immediately after, the "bell-shaped" reverse faults reach the surface (Figs. 3.18 D, 3.19 D and 3.20 D). Subsequently, the extensional fractures grow downwards evolving into vertical or sub-vertical faults and the material between the two sets of faults begins to tilt into the depression (Figs. 3.18 E, 3.19 E and 3.20 E). Further collapse is controlled by a combination of the outward dipping reverse faults and the vertical or sub-vertical ring faults (Figs. 3.18 F, 3.19 F and 3.20 F). Experiments conclude when edge effects begin to be visible and to disguise real results (Fig. 3.18 G). Since the instant at which edge effects become relevant is different for each experiment, it follows that not all the experiments have the same duration.
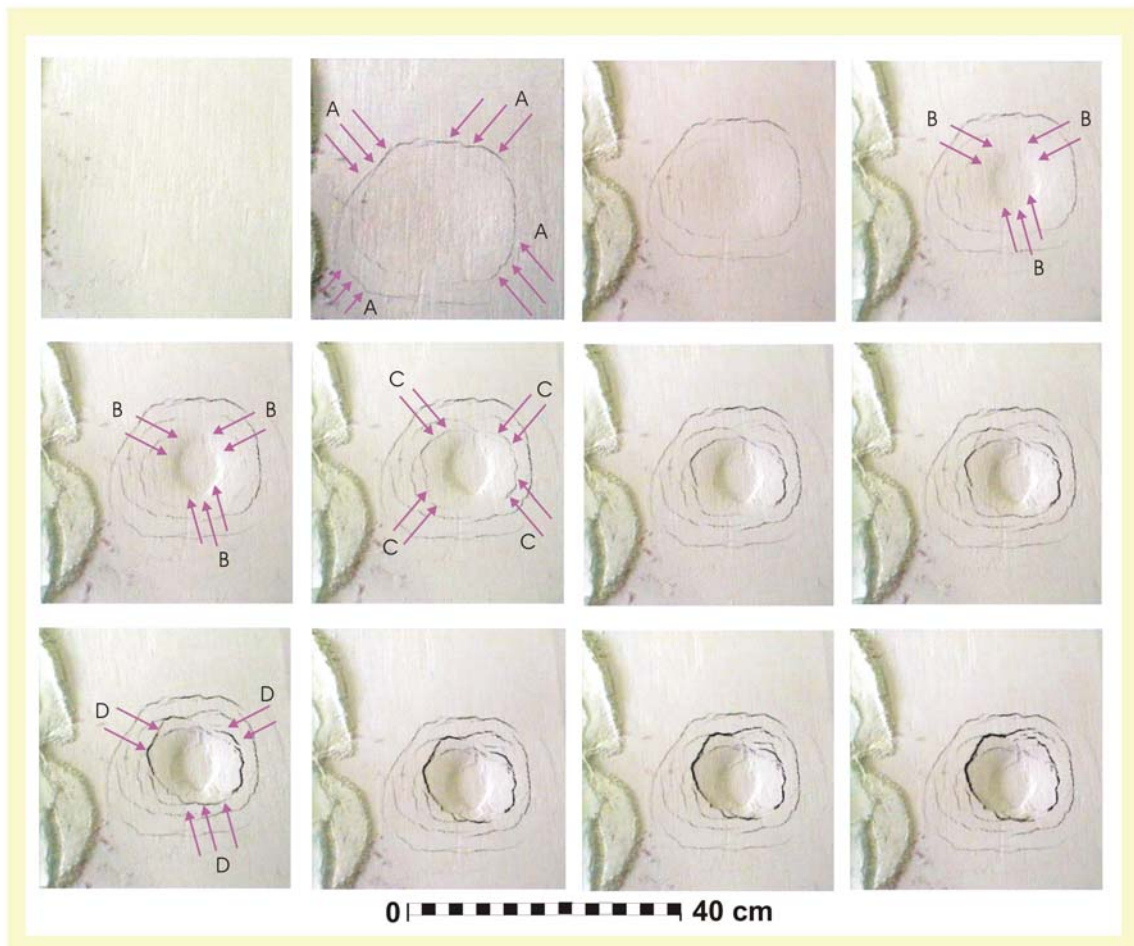
Fig. 3.16: Images of experiment A-7. Photographs taken every 5 s show the evolution of the collapse at surface from the beginning of the experiment until the complete withdrawal of the balloon (magma chamber analogue).
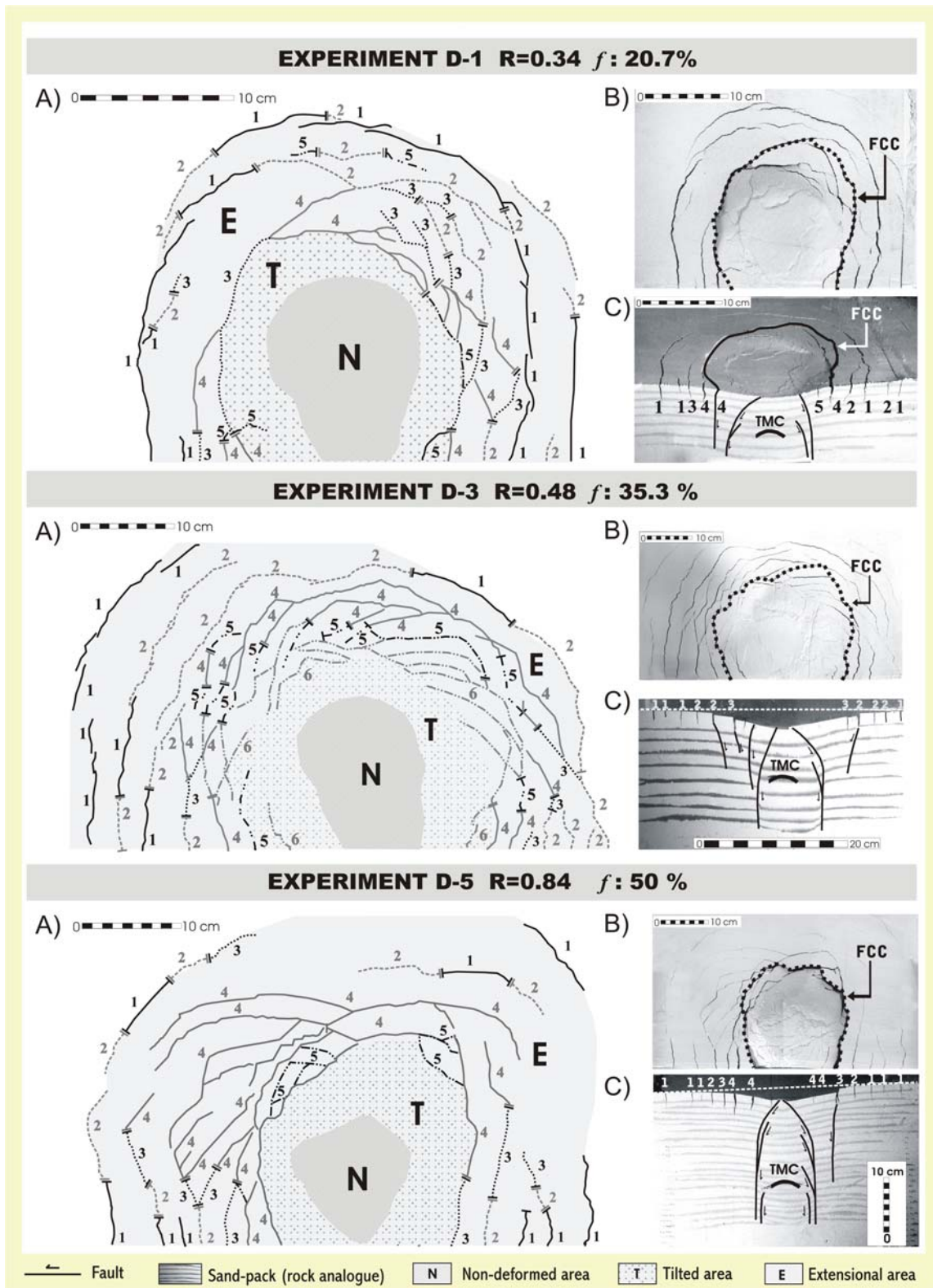
Fig. 3.17: Results for experiments D-1, D-3 and D-5. **(A)** Scheme of surface fractures inferred from photographs. Numbers indicate the order of appearance of the corresponding fracture segment. Different fill patterns show the tilted (**T**), the non-deformed (**N**), and the extensional (**E**) areas. **(B)** Top view photographs. Surface fractures are clearly visible at the extensional zone. Black broken lines indicate the fractures that will evolve into vertical or sub-vertical ring faults and will delimit the piston subsidence during the last stages (FCC). **(C)** Cross section photographs. Numbers, in concordance with those of (A) indicate the order of appearance of fractures. **TMC** Top of the magma chamber analogue at the beginning of the experiment.

Fig. 3.18: Different shots of the caldera collapse process of experiment D-1. The removed volume fraction *f* is indicated in each photograph. White numbers, in concordance with those of Figure 3.17, indicate the order of appearance of fractures at surface.

Fig. 3.19: Different shots of the caldera collapse process of experiment D-3. The removed volume fraction *f* is indicated in each photograph. White numbers, in concordance with those of Figure 3.17, indicate the order of appearance of fractures at surface.
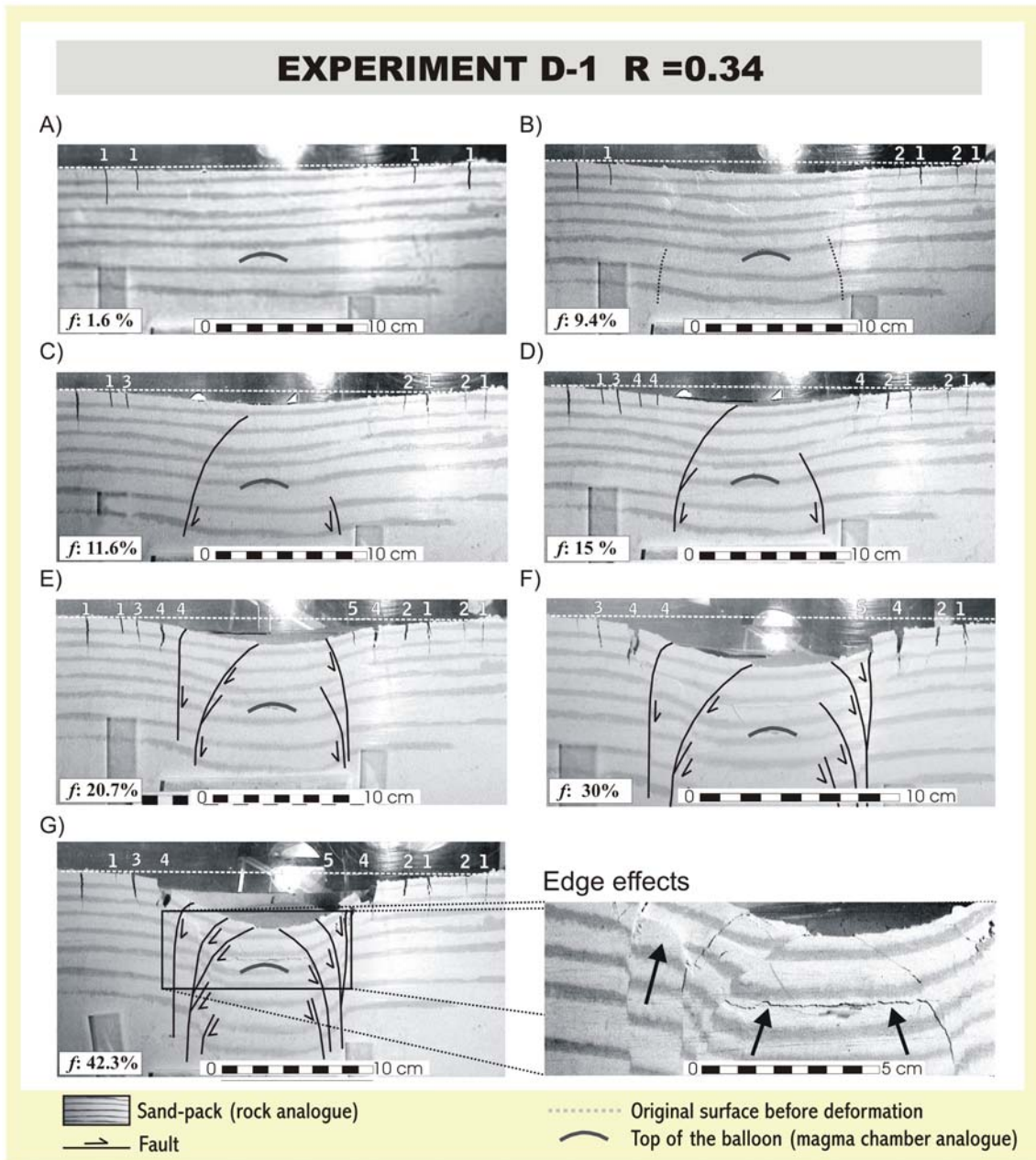
Fig. 3.20: Different shots of the caldera collapse process of experiment D-5. The removed volume fraction *f* is indicated in each photograph. White numbers, in concordance with those of Figure 3.17, indicate the order of appearance of fractures at surface.
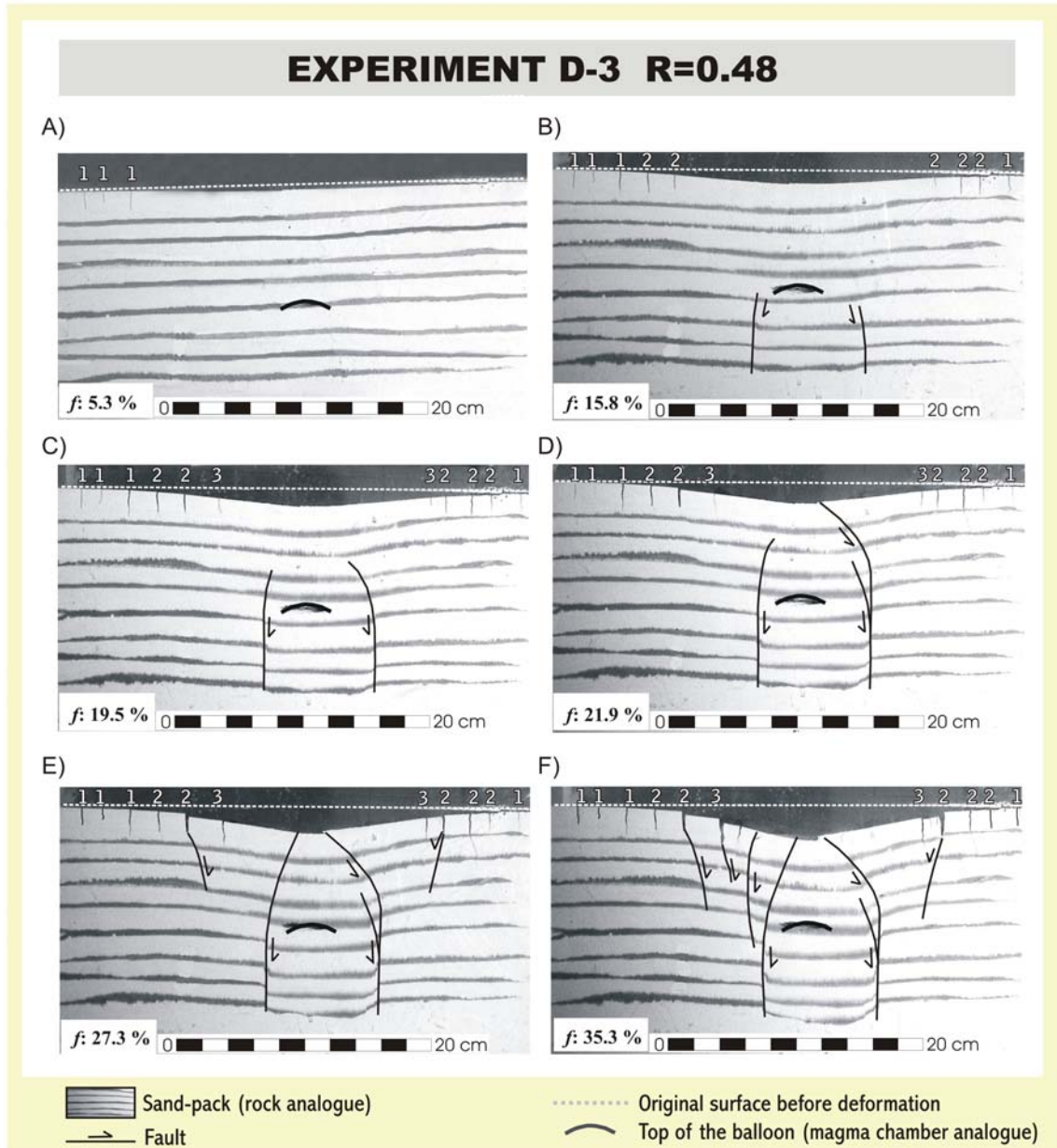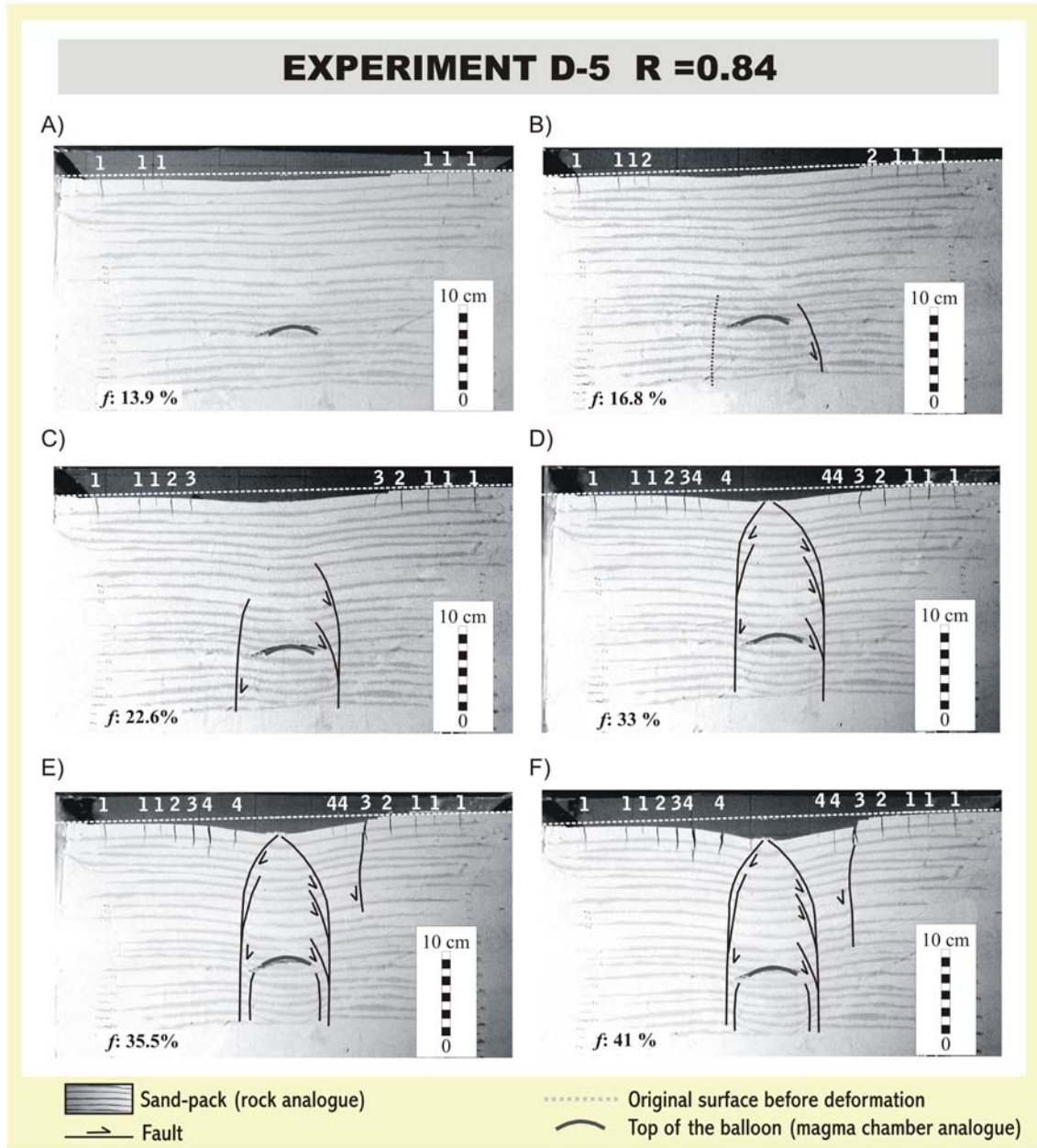
III.3.4.3.4 Pure collapse with homogeneous topography (B- and E-type)

➢   The collapse is piston-like with a non-deformed central part (Figs. 3.21 and 3.22). The subsiding block, bounded by almost vertical ring faults, is a cylinder with a cone on the top. The diameter of the piston is similar to that of the corresponding magma chamber (Table 3.6).

➢   Some reverse faults that never reach the surface form at depth (Figs. 3.21 and 3.22). Subsidence at depth (S_p) is greater than at surface due to the accumulation of displacement along the great number of faults located at depth (Table 3.6).
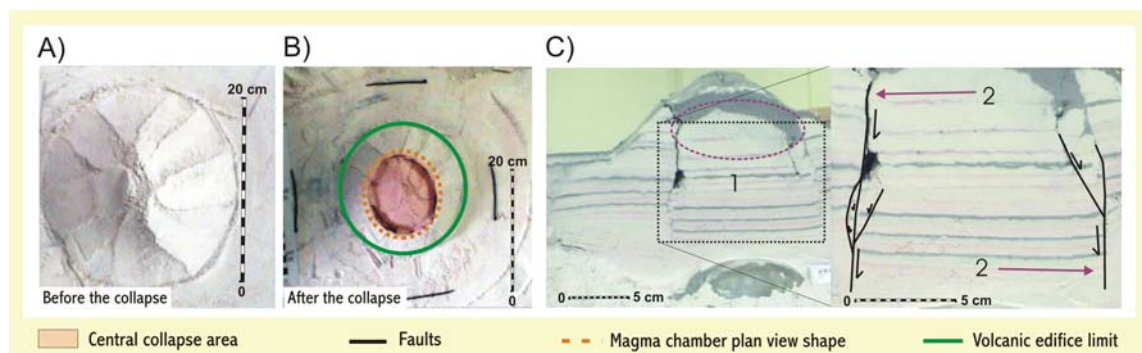
Fig. 3.21: Photographs of experiment B-7. **(A)** Plan view of the experiment before the collapse. **(B)** Plan view of the experiment after the collapse.**(C)** Cross section of the experiment after the collapse. **1** Non-deformed central area of the subsiding piston; **2** Vertical ring faults bounding the piston.

➢   **Temporal evolution**

First, a first pair of reverse ring faults nucleates at depth (Fig. 3.22). The formation of this first group of faults triggers the nucleation of a second set higher up (Fig. 3.22). First these reverse faults are almost vertical and when propagate get curved, losing steepness (50º-60º) (Fig. 3.22). The fault growth pattern continues until one of the sets reaches the surface. Then the collapse becomes piston like. Due to this fault growth pattern when the last group of reverse faults arrive at surface the subsiding block has circular and vertical walls (Fig. 3.22).
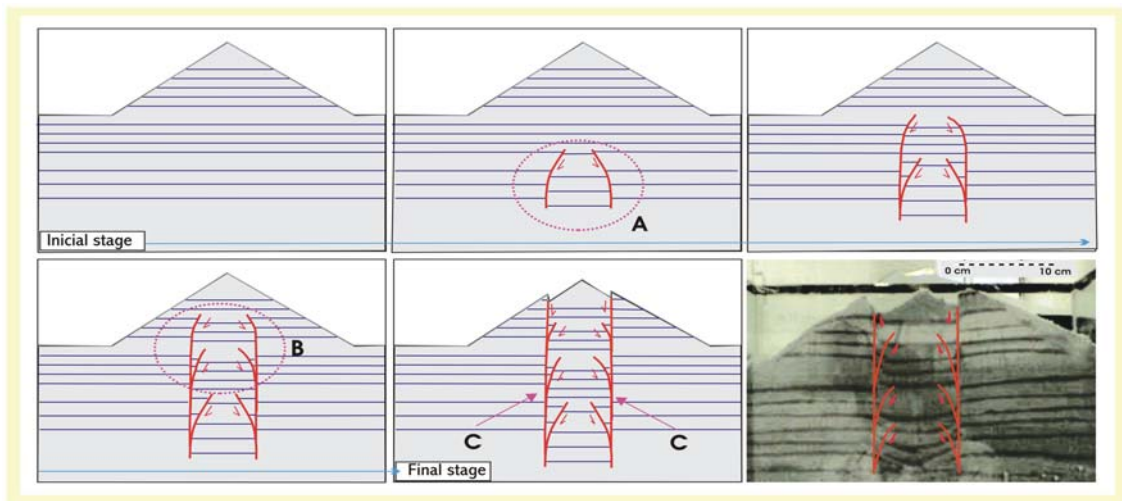
Fig. 3.22: Sketch of the evolution in time of a collapse caldera with pre-existing topography. The photograph corresponds to experiment E-1.

III.3.4.3.5 Pure collapse with heterogeneous topography (C-type)

➢ **For experiments with a heterogeneous edifice, the number of faults delimiting the subsiding block is higher than for homogeneous composition, being the relationship between faults very complex (Fig. 3.23).**
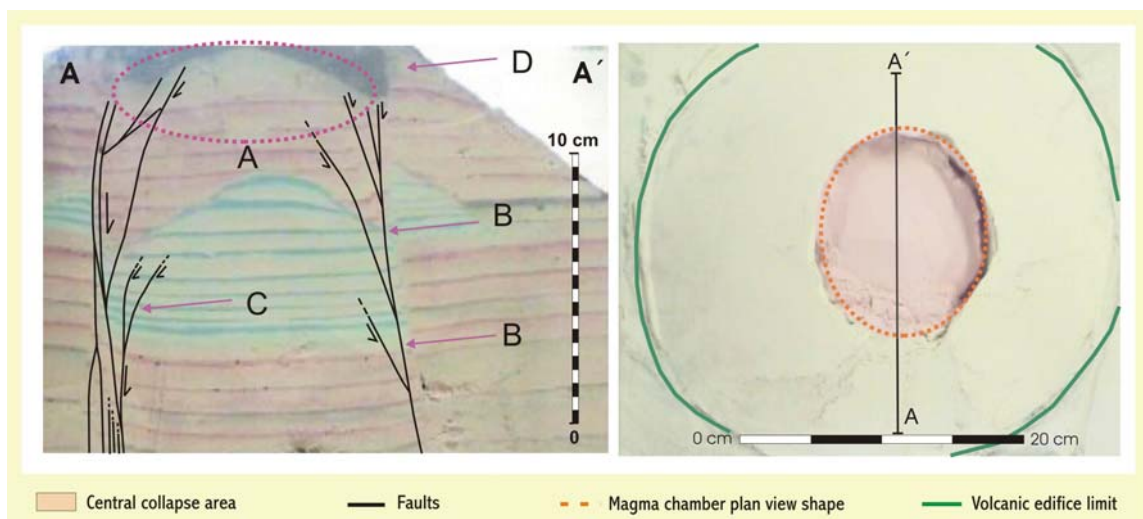
Fig. 3.23: Cross section and plan view photographs of experiment C-1. **A** Non-deformed central area; **B** Vertical normal ring faults delimiting the piston; **C** Reverse faults that do no reach the surface.

III.3.4.3.6 Comparison between experiments with and without topography

➢ **The number of surface extensional fractures is lower in experiments with topography, and the width of the extensional area decreases considerably.**

➢ **Topography has a similar effect as a caldera collapse at high R values:**
   ▪ A great number of reverse faults appear at depth, normally these never reach the surface.
   ▪ Subsidence at depth is greater than at surface
   ▪ The temporal evolution of the caldera collapse is in agreement with the observed in experiments of high R values (compare Fig. 3.20 and 3.22)

➢ **The main differences between experiments of high aspect ratio values and those with topography are:**
   ▪ Calderas formed at high **R** values present deformation at the central part of the piston (Roche et al, 2000). The percentage of non-deformed central area is small in comparison with the total area of the collapse. By contrast, in B/E-type experiments the piston is not deformed, and it maintains the morphology of the topography.
   ▪ Compositional heterogeneities inside the analogue volcanic edifice entail a more complex pattern of faults bounding the subsiding piston and the number faults increases considerably. Despite this structural difference, the piston geometry is equal in both types of edifices.

III. 3.4.3.7 Erupted magma chamber volume fraction

Analogue models have improved notably the comprehension of caldera formation mechanisms. However, no previous work correlates the different stages of a caldera collapse with the volumes of magma withdrawn from the underlying reservoir, a subject addressed only in part by some theoretical models (Druitt and Sparks, 1984; Bower and Woods, 1997; Martí et al., 2000; Roche and Druitt, 2001). This link between magma volume and collapse extent is crucial in terms of hazard, as it might predict when an eruption may evolve into a caldera-forming one. The main goal of this paper is to

evaluate, through analogue modelling, the fraction of magma f (parameter introduced by Roche and Druitt, 2001) that is necessary to be removed in order to create the different set of fractures and faults that will lead to caldera subsidence. To determine the structural evolution of collapse calderas is relevant to understand the relationship between the volume of extruded magma and the total volume of the magma chamber. Furthermore, a subsequent objective is to study the dependency of f with the roof aspect ratio **R** and to determine the f value required to lead to a caldera collapse and compare the obtained results with the existing from mathematical models and natural examples.

For each experiment, we measure the amount of water extracted from the balloon. This way, we are able to calculate the water volume that needs to be removed to form each of structural features we investigate (appearance of the first set of surface fractures, nucleation of the first "bell-shaped" faults, arrival of the "bell-shaped" faults at surface and caldera collapse onset). Results are shown on Table 3.7 and point out that the specific value of f varies from experiment to experiment, that is, there is a dependency of f with R.

Structural phenomena	Experiments						B		r^2
	E-1 R = 0.34								
Appearance of the first SFs	1.6	5.3	5.9	10	10.3	17	7.6	10.4	0.97
Appearance of the first BSFs	9.4	13.3	12	16.8	17	26	8.2	17.9	0.96
BSFs reach the surface	15	22	22.3	33	36.5	43	14.9	32.7	0.96
Caldera collapse onset	20.7	27.3	31.4	35.5	45.1	64.8	22.4	43.5	0.97

Table 3.7: Values of f at which the different structural sets or phenomena appear. Rounded values for A and B in a log fit $f(\mathbf{R})=A \ln(\mathrm{R}) + B$ are also given. r^2 Coefficient of determination (r^2 =1 implies a perfect fit); **SF** Surface fracture; **BS**F "Bell-shaped" fault.

Figure 3.24 sketches the evolution of the collapse process for different experiments. For a given value of f, experiments with higher **R** show a delay in comparison with experiments with a lower value of **R**. For example, in experiment D-1 (**R** = 0.34) with f = 30%, the reverse faults generated at depth have already reached the surface and the vertical or sub-vertical faults nucleated at surface have already propagated downwards. In contrast, in experiment D-7 (**R** = 2.34) with the same value of f, the reverse faults are just in the first stages of development.

Additionally, Figure 3.25 plots the necessary erupted magma chamber volume fraction f versus **R**. The Figure includes those f values necessary to form the first surface fractures (Fig. 3.25 A) and those required to lead the "bell-shaped" faults reach the surface for the first time (Fig. 3.25 B). Fractions of volumes for the opening of tensional fractures at surface range approximately from 1 to 20% and those for "bell-shaped" faults reaching the surface from 15 to 45%. Both datasets are dependent on the aspect ratio. The experimental dependency f (**R**) is well fitted by a log function f (**R**)=A ln(**R**) + B where A and B are constants. Best-fit values for these parameters are given in Table 3.7.
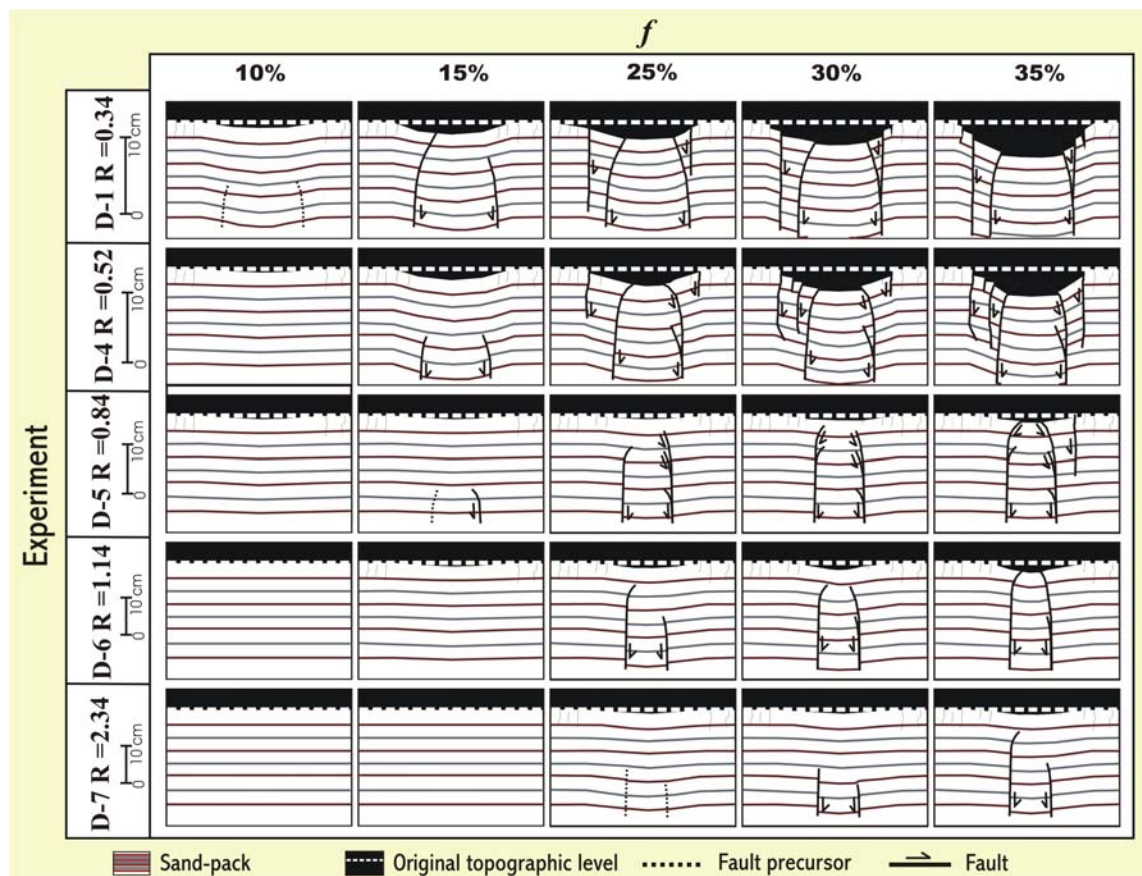

Fig. 3.24: Sketches showing different stages in the structural evolution of the collapse process. Notice that for constant values of f structural development is strongly dependent on the roof aspect ratio **R**.
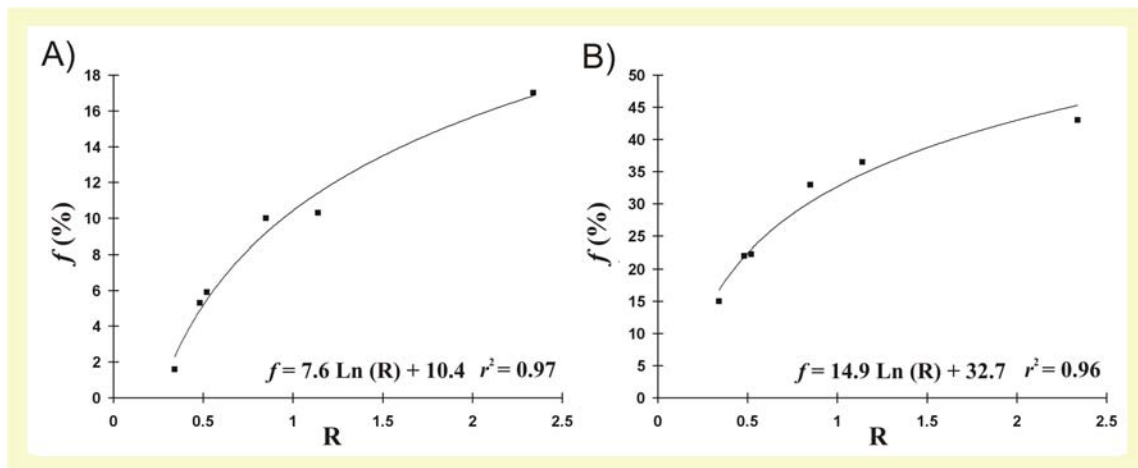
Fig. 3.25: Dependency *f* (**R**). **(A)** Appearance of the first fractures at surface. **(B)** The "bell-shaped" reverse faults reach the surface. A log-fit to experimental data is given in both cases. *r* Coefficient of determination (r^2 = 1 implies perfect fit).

From a hazard point of view it is of special interest to assess if a particular eruption may be able to trigger a collapse caldera (in the strict sense of a "large" morphologic depression), as this would drastically change the course of the eruption. To achieve this purpose, it is necessary to define along the eruption the "point of no return", that is, to assess when the formation of a large morphologic depression (collapse of the chamber roof) will be unavoidable in a natural system. Since caldera formation is controlled by subsidence along vertical or sub-vertical annular faults and reverse "bell-shaped" faults in its interior, we assume that a "collapse caldera" would irremediably occur in nature when reverse faults reach the surface and, simultaneously, a number of surface fractures have already evolved into vertical or sub-vertical ring faults. Results are shown in Figure 3.26. We define f_{CRIT} as the critical erupted magma chamber volume fraction required to trigger caldera collapse. Values for f_{CRIT} may vary from values as little as 20% for low aspect ratio chambers (**R** = 0.34) to 70% for the highest **R** (**R** = 2.34).
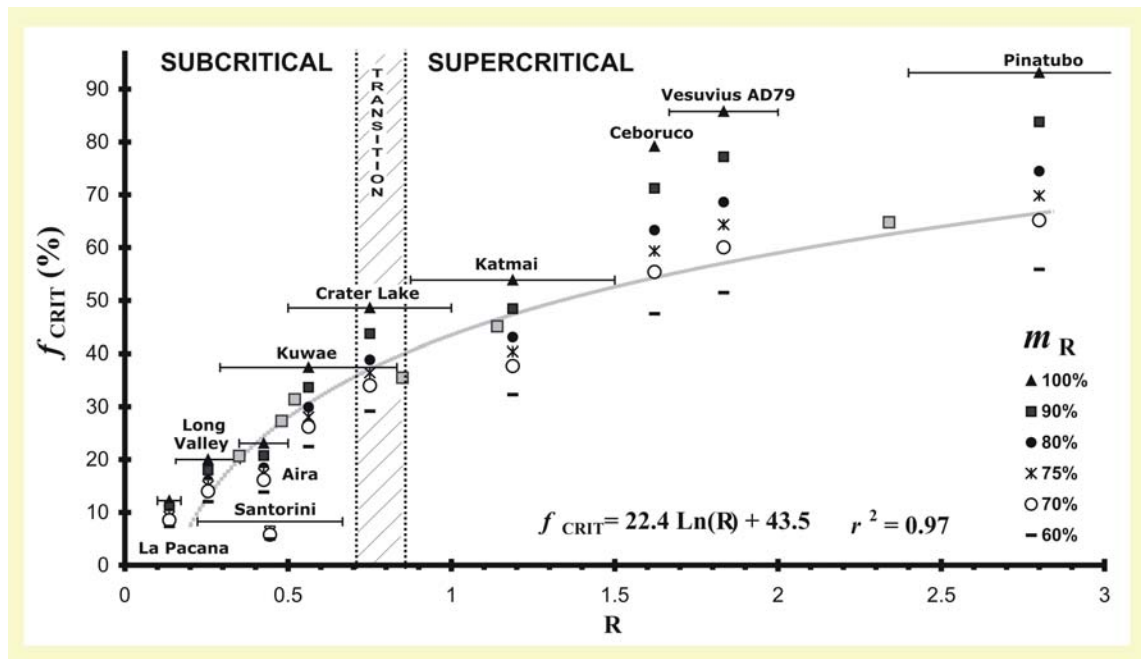
Fig. 3.26: Erupted volume fraction at the caldera onset as a function of **R**. Grey squares indicate experimental f_{CRIT} values (f values at the caldera collapse onset). A discontinuous line shows the log-fit to experimental values. Values of f_{CRIT} for natural examples are calculated considering different percentages (100% - 60%) of erupted magma (see text for details). Horizontal lines in triangles (f_{CRIT} values considering that the magma chamber is completely emptied) are the error bars due to the roof aspect ratio uncertainty. The vertical lined zone line marks the transition from subcritical to supercritical collapses.

Table 3.8 contains data for some well-documented calderas that cover the range of values of **R** considered in the experiments. The critical erupted magma chamber volume fraction for the natural examples is obtained considering that $f_{CRIT} = 100 \times V_{PC} / V_{MC}$, where V_{PC} is the volume of the pre-caldera deposits and V_{MC} is the total volume of the magmatic reservoir before the eruptive event, both in DRE (dense-rock equivalent). A serious drawback is that direct information on magma chamber volumes is in general scarce or unavailable and one has to infer data from field observations like the total volume of extruded deposits V_{TD} (pre-caldera plus syn-caldera). Some authors (e.g. Roche and Druitt, 2001), assuming an idealized end-member situation, consider that magma chambers empty completely during the collapse, i.e. that all the magma inside the chamber is removable. Therefore, V_{MC} is estimated assimilating the total volume of the deposits V_{TD} to that of the original chamber ($V_{MC} = V_{TD}$). A natural example for this is the Crater Lake caldera, where Druitt and Bacon (1989) observed basal chamber cumulate textures in that last erupted magmas. However, this is not necessarily the most common situation in natural systems. In some cases, the

erupted volume is only a part of the total volume of magma inside the reservoir (e.g. Katmai AD~1000 eruption, Hildreth and Fierstein, 2000). Therefore, we estimate the critical erupted magma chamber volume fraction of natural examples considering that, during the eruption, the magma chamber can be totally (100%) or partially (90% - 60%) emptied. Therefore, we define m_R as the percentage of magma removable from the reservoir during the eruptive event. Once calculated V_{TD}, it is necessary to estimate the volume of the pre-caldera deposits V_{PC}. In some cases, an accurate stratigraphic and lithologic work makes possible the volume estimation. Commonly, caldera onset in the stratigraphic record is clearly identifiable, for example, by a significant increase and large variations in nature, size and grading of lithics in the pyroclastic deposits (e.g. Suzuki-Kamata et al., 1993; Gardner and Tait, 2000; Browne and Gardner, 2004). Moreover, monitoring information such us the record of large earthquake clusters (e.g. Hildreth and Fierstein, 2000) may be used as an additional way to detect collapse onset and to calculate V_{PC}. However, in some cases, caldera collapse starts very early in the eruption thus producing very little pre-caldera deposits (e.g. La Pacana - *Argentina*, Lindsay et al., 2001).

Figure 3.26 plots the values of f_{CRIT} for the natural examples depending on m_R together with those experimentally obtained.

Caldera, *Formation*	$V_{TD}(km^3)$	$V_{PC}(km^3)$	P (km)	D (km)	*r*	Ref.
La Pacana , *Atana Ignimbrite*	1600	< 160	6	60 × 35	0.1-0.17	[190, 295]
Long Valley , *Bishop Tuff*	750	150	5-6	17 × 32	0.16-0.35	[251, 280]
Santorini , *Minoan Tuff*	27-33	2-3	2-3	6 × 9	0.22-0.67	[41, 96, 280]
Aira , *Ito Tuff*	143	33	7-10	20	0.35-0.5	[280]
Katmai	13	7	3.5-4.5	3 × 4	0.88-1.5	[151, 152, 153]
Crater Lake, *Climactic*	40-64	17-35	5-8	8 × 10	0.5-1	[96,17, 280]
Ceboruco, *Jala Pumice*	3-4	2.5-3	>6	3.7	1.62	[52,280]
Vesuvius, *Pompeii Pumice*	1.2-1.7	1-1.5	5-6	3	1.67-2	[280]
Pinatubo	3.7-5.3	3.4-5	6-8	2.5	2.4-3.2	[280]

Table 3.8: Natural examples. **D (D$_{min}$ × D$_{max}$)** Caldera diameter, i.e. magma chamber diameter; **P (P$_{min}$ - P$_{max}$)** Magma chamber depth; **R** roof aspect ratio; **V$_{PC}$** Volume of the pre-caldera deposits given in DRE (dense-rock equivalent); **V$_{TD}$** Total volume of deposits given in DRE.

Experimental and natural data sets present a similar behavior. Values of f_{CRIT} of the natural examples are strongly dependent on the value of m_R considered, especially at high roof aspect ratios. Values of critical erupted magma chamber volume fraction of natural examples fit the experimental curve particularly at low roof aspect ratios (**R** < 0.7 - 0.85), e.g. Aira, Long Valley and La Pacana caldera. In contrast, for calderas with high roof aspect ratios (**R** > 0.7 - 0.85), f_{CRIT} values match notably the log fit only if a partial emptying of the magma chamber is considered, e.g. Crater Lake (m_R ~80%), Ceboruco (m_R ~70%), Vesuvius (m_R ~70%), Pinatubo (m_R ~75%).

Apart from the influence of m_R we argue that discrepancies between natural and experimental values may have at least two additional origins. First, experimental measures of the f_{CRIT} are obtained when the ring fault system is not completely developed (extensional fractures have just begin to propagate downwards and to evolve into vertical or sub-vertical faults). In contrast, in a natural case, the value of f_{CRIT} is inferred from the volume of the pre-caldera deposits V_{PC}. The limit between pre- and syn-caldera deposits is marked, for example, by a sudden large increase on the lithic contents due to the opening of ring faults (Roche and Druitt, 2001), or by changes observed in the eruptive style, e.g. a Plinian phase followed by large volumes of pyroclastic flows during the Minoan eruption of Santorini volcano (Bond and Sparks, 1976) or the climactic eruption of Mount Mazama (Bacon, 1983). Both datasets may have, therefore, a small "temporal" shift that implies that f_{CRIT} values for experiments may be underestimated with respect to natural examples. A second source of discrepancy may come from the wide error bar related to the calculation of the roof aspect ratio in natural examples (e.g. Crater Lake **R**= 0.5 - 1, Pinatubo **R** = 2.4 - 3.2). For example, the f_{CRIT} value for Crater Lake caldera assuming **R** = 0.81 (value within the range proposed by Roche and Druitt, 2001) matches perfectly the experimental curve when m_R = 80 %. In contrast, if **R** = 1 the chamber could be emptied up to 90% in volume and the f_{CRIT} value would still match the experimental log-fit.

A number of analytical models based on physical properties of magmas have correlated extruded volumes to magma chamber pressure drops. Despite these studies do not focus on the structural evolution they can roughly predict the erupted volume at the onset of collapse by assuming a chamber underpressure equal to the strength of the embedding rocks. Druitt and Sparks (1984) estimated values of f_{CRIT} between 10-30%, whereas Martí et al. (2000) came up with values ranging from a few percent for deep, gas-poor reservoirs, to 40% for shallow, gas-rich chambers. On the other hand, Roche

and Druitt (2001) proposed variations in f_{CRIT} from less than 10% to the whole chamber volume depending on the roof aspect ratio. Our experimental results constrain f_{CRIT} to values lower than 55% except for very high aspect ratio chambers $R > 2$.

III. 3.4.3.8 Subsidence pattern during the collapse process

Another important aspect to consider is the subsidence pattern during the collapse process, i.e. how subsidence increases with the erupted magma chamber volume fraction f. A new variable is introduced here, the subsidence ratio γ, defined as:

$$\gamma = \frac{S_{smax}}{H} \qquad [3.5]$$

where H is the balloon height (i.e. chamber thickness) and S_{smax} is the maximum subsidence measured at surface. The maximum point of subsidence is located approximately at the centre of the non-deformed area.

Figure 3.27 plots γ versus f for different experiments (D-1, D-3, D-4, D-5, D-6 and D-7). At low aspect ratios ($R < 0.7 - 0.85$) the experimental dependency $\gamma(f)$ is well fitted by a linear function $\gamma(f) = A f + B$, where A and B are constants that vary from experiment to experiment. Best-fit values for these parameters are listed in Table 3.9. At high aspect ratios ($R > 0.7-0.85$), this dependency is slightly different. Prior to the arrival of the "bell-shaped" faults to the surface, values of γ fit a linear function with gentle slope (e.g. D-5 $R=0.84$ and D-6 $R=1.14$) (Table 3.9). Once the reverse faults have reached the surface, the slope increases and becomes similar to those corresponding to low roof aspect ratios.

Differences in the subsidence pattern between experiments with high or low roof aspect ratios values, are due to the collapse mechanisms controlling both type of processes. For low aspect ratios caldera collapses ($R > 0.7 - 0.85$), the "bell-shaped" faults reach the surface very rapidly ($f < 25\%$) and the subsidence process is quickly controlled by the ring faults (at $f < 35\%$). By contrast, at high aspect ratios ($R > 0.7-0.85$) due to the high number of internal "bell-shaped" faults located at depth the ring faults controlling the collapse appear later (at $f > 45\%$ for $R > 1$). During the first stages,

subsidence increases at depth more than at surface. The latter increases when the reverse faults nucleated at depth reach the surface and the collapse is principally controlled by the vertical ring faults. This phenomenon is apparently reflected on the change of slope of the function $\gamma(f)$. The linear function has a gentle slope while the "bell-shaped" faults propagate upwards. Once these reverse faults have reached the surface and the ring faults begin to control the collapse, the slope increases, i.e. subsidence at surface is more effective when the vertical ring faults control the collapse.
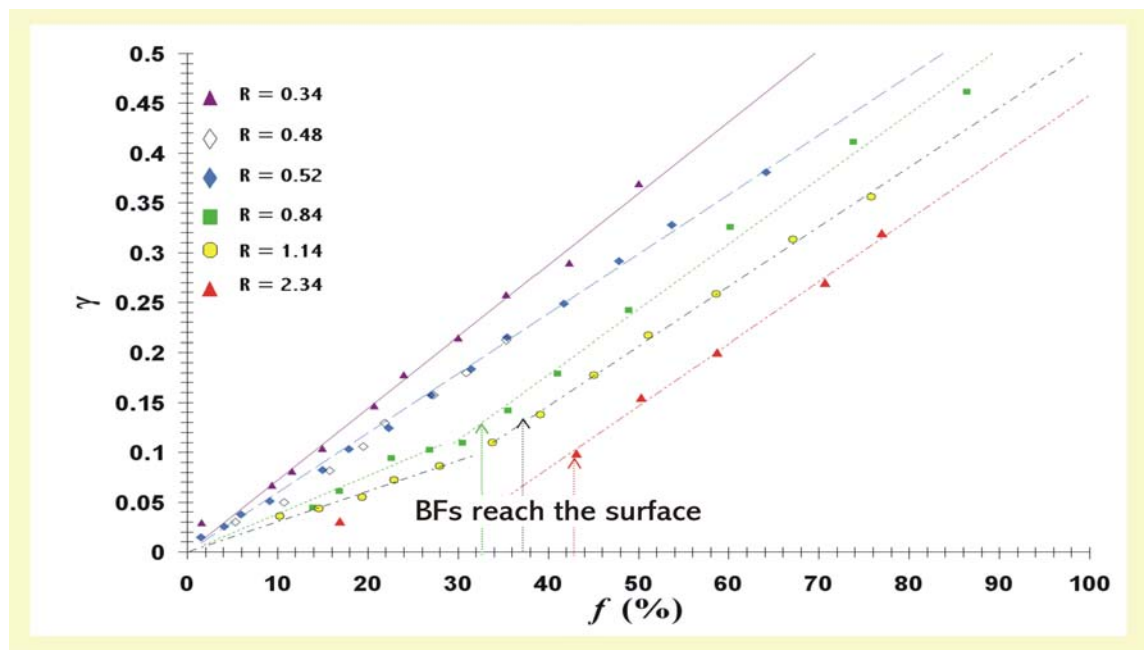

Fig. 3.27: Values of γ towards f for the different experiments. For low aspect ratios (**R** < 0.7-0.85) experimental data fit to a linear function. For high aspect ratios (**R** > 0.7-0.85), data do not fit to a linear function up to the "bell-shaped" faults (**BFs**) have reached the surface. Notice that f = 100 % implies that the water-filled balloon is completely empty and γ = 1 that subsidence is equal to the balloon's height.

| | | D-3 | D-4 | Experiments | | | | D-7 R =2.34 |
| | R = 0.34 | R =0.48 | R = 0.52 | D-5 R =0.84 | | D-6 R =1.14 | | |
				before BFs	after BFs	before BFs	after BFs	after BFs
A	0.0072	0.0058	0.006	0.0038	0.0065	0.0031	0.006	0.0062
B	0	0	0	0	-0.084	0	-0.09	-0.17
r²	0.99	0.99	0.99	0.93	0.99	0.975	0.99	0.99

Table 3.9: Rounded values for A and B in a linear fit γ=A f + B. r^2 is the coefficient of determination (r^2 implies a perfect fit). In the case of high roof aspect ratios (**R**=0.7), the subsidence pattern is subdivided in two different linear-functions. Approximately, the change takes place when the "bell-shaped" faults reach the surface.

In Figure 3.28 we take up again the graph illustrated in Figure 3.27 and continue it to $f > 100\%$ (remember that $f = 100$ % implies that the water-filled balloon is completely empty). The principal aims of this Figure are to calculate γ at he moment the balloon is completely empty ($f = 100$ %) and to estimate f when the maximum subsidence at surface S_{smax} is equivalent to the balloon's height H, i.e. $\gamma = 1$.

Theoretically, a rigid piston-like collapse would imply that at $f = 100$ % the maximum subsidence at surface is equivalent to the balloon height, i.e. $\gamma = 1$. By contrast, results obtained are different. We observe that for all illustrated experiments γ at $f = 100$ % is smaller than 1 (Fig. 3.28 indication I). Additionally, γ at $f = 100$ % increases when the roof aspect ratio R decreases. Moreover, if we calculate the required f to achieve $\gamma = 1$, we can observe that all obtained f values are higher than 100% and that it increases with R.

In fact, subsidence does not always correspond to a rigid piston collapse. For low roof aspect ratio values ($R < 0.7 - 0.85$) subsidence is controlled principally by a low number of "bell-shaped" faults and almost vertical ring-faults. Consequently, the collapse mechanism is not so far away from the strict piston-like collapse. Therefore, for those experiments with low R, γ at $f = 100$ % is closer to 1 and f at $\gamma = 1$ to 100%. By contrast, with increasing R the collapse mechanism is completely different. In those cases, the number of "bell-shaped" faults increases considerably breaking the roof in wedges (see section III.3.4.3.3). On the one hand, this collapse mechanism leads to a porosity increase and consequently, to an increase of the subsiding block volume disguising the real total subsidence. Additionally, due to the fault configuration subsidence is accommodated at depth and do not spread to the surface. The abovementioned phenomena imply that for high R values γ at $f = 100$ % is much lower than 1 and f at $\gamma = 1$ much higher than 100%, i.e. if we want to observe at surface a S_{smax} equivalent to the balloon height, it would be necessary to continue the collapse process (magma chamber withdrawal) until unrealistic limits ($f > 100\%$).
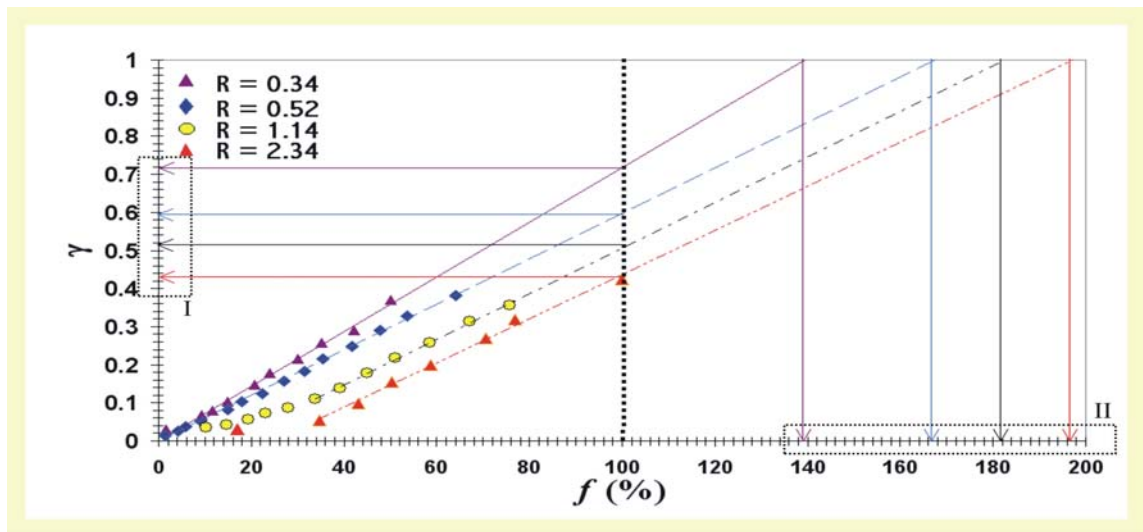
Fig. 3.28: Values of γ towards *f* for the different experiments. Notice that *f* = 100 % implies that the water-filled balloon is completely empty and γ = 1 that subsidence is equal to the balloon's height.

III.3.4.3.9 Dependency of the collapse dimensions with the roof aspect ratio

Several studies (e.g. Roche et al., 2000; Lavallée et al., 2004; Kennedy et al., 2004) and this work have demonstrated that the roof aspect ratio influences the style of a caldera collapse. Previous studies were mainly focused in analysing the structural changes (due to variations on the roof aspect ratio value) in cross section. Only Roche et al. (2000) and Acocella et al. (2001b) carried out a more exhaustive investigation of possible changes at surface studying the variations in size of the non-deformed area (**N**), the piston diameter (**P-D**) and the extensive zone (**EXT**) depending on the roof aspect ratio value.

In Figure 3.29 are plotted for experiments A- and D-type the values of the outer limit diameter **OL-D**, the piston diameter **P-D** and the non-deformed area diameter **N-D** towards the corresponding roof aspect ratio. In order to facilitate the subsequent comparison with silicone models, values of piston diameter (**P-D**), non-deformed area diameter (**N-D**) and collapse outer limit diameter (**OL-D**) are normalized as follows:

$$\text{P-D}_{\text{NOR}} = \frac{\text{P - D}}{\text{D}_{\text{MEAN}}} \quad ; \quad \text{N-D}_{\text{NOR}} = \frac{\text{N - D}}{\text{D}_{\text{MEAN}}} \quad ; \quad \text{OL-D}_{\text{NOR}} = \frac{\text{OL - D}}{\text{D}_{\text{MEAN}}} \qquad [3.6]$$

where **D$_{\text{MEAN}}$** is the mean diameter of the magma chamber.

272

Fig. 3.28: Values of γ towards f for the different experiments. Notice that f = 100 % implies that the water-filled balloon is completely empty and $\gamma = 1$ that subsidence is equal to the balloon's height.

III.3.4.3.9 Dependency of the collapse dimensions with the roof aspect ratio

Several studies (e.g. Roche et al., 2000; Lavallée et al., 2004; Kennedy et al., 2004) and this work have demonstrated that the roof aspect ratio influences the style of a caldera collapse. Previous studies were mainly focused in analysing the structural changes (due to variations on the roof aspect ratio value) in cross section. Only Roche et al. (2000) and Acocella et al. (2001b) carried out a more exhaustive investigation of possible changes at surface studying the variations in size of the non-deformed area (**N**), the piston diameter (**P-D**) and the extensive zone (**EXT**) depending on the roof aspect ratio value.

In Figure 3.29 are plotted for experiments A- and D-type the values of the outer limit diameter **OL-D**, the piston diameter **P-D** and the non-deformed area diameter **N-D** towards the corresponding roof aspect ratio. In order to facilitate the subsequent comparison with silicone models, values of piston diameter (**P-D**), non-deformed area diameter (**N-D**) and collapse outer limit diameter (**OL-D**) are normalized as follows:

$$\text{P-D}_{NOR} = \frac{\text{P - D}}{\text{D}_{MEAN}} \quad ; \quad \text{N-D}_{NOR} = \frac{\text{N - D}}{\text{D}_{MEAN}} \quad ; \quad \text{OL-D}_{NOR} = \frac{\text{OL - D}}{\text{D}_{MEAN}} \qquad [3.6]$$

where D_{MEAN} is the mean diameter of the magma chamber.
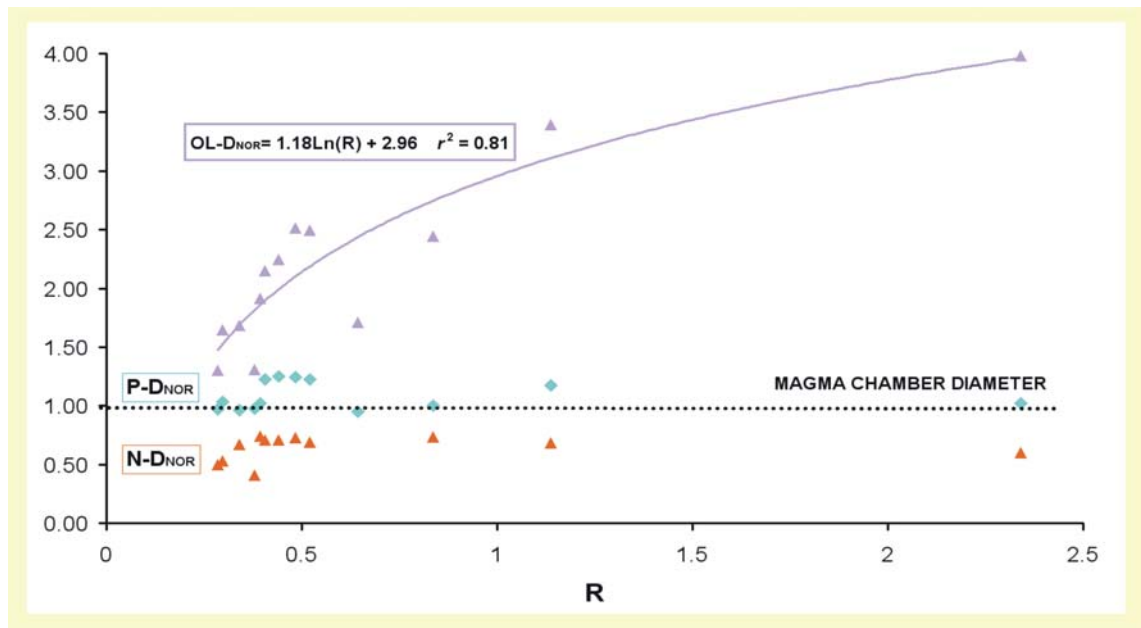
273

Fig. 3.29: Graph of normalized values for outer limit diameter **OL-D$_{NOR}$**, piston diameter **P-D$_{NOR}$** and non-deformed area diameter **N-D$_{NOR}$** towards roof aspect ratio.

In short, with increasing roof aspect ratio the diameter of the collapse outer limit increases and both the diameter of the subsiding piston and of the non-deformed area remain approximately constant. Experimental data for the outer limit diameter may fit a log function OL-D$_{NOR}$= 1.18Ln(**R**) + 2.96, but the coefficient of determination is low r^2 = 0.81. Furthermore, values close to one for the normalized piston diameter indicate that the area of the subsiding block is similar to that of the magma chamber and consequently, that ring faults controlling the piston are vertical. Moreover, when P-D$_{NOR}$ is higher than one, the faults bounding the piston are inward dipping or the collapse depression has been widened by fall down of the overhanging caldera walls (see section II.3.7.2.3). In addition, constant values of the non-deformed area diameter around 0.7 indicate that this zone is always delimited by outward dipping structures. Furthermore, if the outer limit increases with **R** and the non-deformed area remains constant it implies that with increasing roof aspect ratio values increases the extensional zone.

III.3.5 Silicone models

III.3.5.1 Realized experiments: Design and input parameters

A total of 17 silicone experiments have been carried out (Table 3.10), 13 with flat and 4 with curved silicone reservoir. All experiments reproduce a pure caldera collapse process without topography. Experiments SIL_{SEC} are focused to study the temporal evolution of the collapse. Therefore, input parameters are identical except of the experiment duration (t). Experiments were arrested (by solidifying sand with water) after different amounts of subsidence (i.e. elapsed time). By studying the internal structure of each experiment, it is possible to reconstruct a temporal sequence of fault propagation and collapse. This was possible because the experiments were reproducible.

Experiment	INPUT PARAMETERS				
	P (cm)	**D (cm)**	**t (min)**	**Shape**	**R**
SIL-1	2	10	150	FLAT	0.2
SIL-2	3	10	140	FLAT	0.3
SIL-3	4	10	180	FLAT	0.4
SIL-4	5	10	140	FLAT	0.5
SIL-5	6	10	90	FLAT	0.6
SIL-6	6	10	120	FLAT	0.6
SIL-7	7	10	136	FLAT	0.7
SIL-8	8	10	180	FLAT	0.8
SIL-9	3.3	10	100	A= 1.7 cm $e = 2.94$	0.33
SIL-10	2.2	10	60	A= 2.8 cm $e = 1.79$	0.22
SIL-11	2.5	10	n.c.	A= 3.5 cm $e =1.43$	0.25
SIL-12	3.4	10	75	A= 4.6 cm $e = 1.08$	0.34
SIL$_{SEC}$-1	3	10	13	FLAT	0.3
SIL$_{SEC}$-2	3	10	20	FLAT	0.3
SIL$_{SEC}$-3	3	10	38	FLAT	0.3
SIL$_{SEC}$-4	3	10	52	FLAT	0.3
SIL$_{SEC}$-5	3	10	66	FLAT	0.3

Table 3.10: List of experiments with silicone reservoir carried out in this study. **D** Silicone reservoir diameter; *e* Silicone reservoir eccentricity defined as 0.5×**D/A** (*e*=1 implies an hemispheric silicone reservoir and e=0 flat roof); **P** Depth of the silicone reservoir; **R** Roof aspect ratio= P/D; **t** Duration of the experiment.

III.3.5.2 Complementary scaling

In Table 3.11 are listed the variables involved in analogue models with silicone reservoir as magma chamber analogue. A total of 8 variables, all of them considered as "principal", take part in the scaling process. Therefore, according to the Buckingham-Π theorem, 8 variables involving three different dimensions (L: Length, M: Mass, T: Time) need 5 independent dimensionless Π-numbers to guarantee similarity (Table 3.5).

The Π-numbers and their corresponding experimental and natural values are recorded in Table 3.12. Their comparison shows very close values for Π_1, Π_2 and Π_3 Furthermore, experimental values for Π-numbers Π_4 and Π_5 fall in the range of the natural values. Concluding, silicone experiments are considered as "correctly" scaled.

	Variable & definition	Experimental value	Natural value	Dimensions	References
P	"Magma chamber" depth (balloon depth)	2×10^{-2}- 6×10^{-2}m	3×10^3 –10^4m	[L]	[71,15,193,198,251, 327,383]
D	"Magma chamber" diameter (balloon diameter)	10×10^{-2}m	5×10^3-10^5m	[L]	[193,198,237,251,322, 327,368]
ρ_s	"Host rock" density (sand density)	1270 kg/m^3	2500-2800 kg/m^3	[M L^{-3}]	[12]
ϕ	Internal friction angle of sand	37°	20-40°	-	[276]
ν	"Magma" viscosity (silicone viscosity)	5×10^4 Pa s	10^3-10^{13} Pa s	[M L^{-1} T^{-1}]	[149]
ρ_m	"Magma" density (silicone density)	970 kg/m^3	2000-2700 kg/m^3	[M L^{-3}]	[33]
t	Duration of the experiment	60-350 s	9-98 h	[T]	[185]
g	Gravity	9,81 m/s^2	9,81 m/s^2	[M T^{-2}]	---

Table 3.11: Variables relevant in the analogue models with silicone as magma analogue. All variables are red are considered as "principal" and important for a correct scaling of the geological process of caldera collapse. Cited bibliography is referred to natural values sources.

Π–Numbers	Experimental values	Natural values
Π_1= P/D	0.2-0.8	0,1-4,5
Π_2=ϕ	37°	20-40°
Π_3=ρ_s/ρ_m	1.3	0.93-1.4
Π_4= P/gt^2	9×10^{-8}–7.6×10^{-7}	$\sim10^{-9}$-10^{-6}
Π_5= P$^2\rho_m/\nu$t	5×10^{-8} – 3×10^{-7}	$\sim10^{-9}$-10^3

Table 3.12: Values of the Π dimensionless numbers in experiments and in nature.

III.3.5.3 Results

III.3.5.3.1 Measured and calculated values

In this section we summarize the most significant results obtained with the different silicone reservoir analogue models (Table 3.13).

Experiments	MEASURED AND CALCULATED VALUES					
	R	S_p (cm)	S_s (cm)	N-D (cm)	OL-D (cm)	EXT-W (cm)
SIL-1	0.2	0.83	0.83	7.4	9.8	1.20
SIL-2	0.3	0.76	0.76	6	10.5	2.25
SIL-3	0.4	1.4	1.4	5	9.8	2.40
SIL-4	0.5	0.8	0.8	4	8	2
SIL-5	0.6	0.96	0.96	2.9	7.4	2.25
SIL-6	0.6	0.91	0.8	2.8	7.2	2.2
SIL-7	0.7	1	0.8	2.75	5.7	1.48
SIL-8	0.8	1	0.5	1.7	3.57	0.94
SIL-9	0.33	1.46	0.85	5.54	10.7	2.58
SIL-10	0.22	n.c..	0.92	5.7	10.17	2.23
SIL-11	0.25	0.8	0.8	6.12	11.51	2.70
SIL-12	0.34	2.6	2.6	2.11	4.07	0.98
SIL$_{SEC}$-1	0.3	n.c.	n.c.	n.c.	10.5	n.c..
SIL$_{SEC}$-2	0.3	0.2	0.2	n.c.	10.2	n.c..
SIL$_{SEC}$-3	0.3	n.c..	n.c.	7.3	10.1	1.40
SIL$_{SEC}$-4	0.3	0.5	0.5	6.7	10.2	1.75
SIL$_{SEC}$-5	0.3	0.64	0.64	6.3	10.2	1.95

Table. 3.13: Relevant measured or calculated parameters in silicone analogue models. **EXT-W** Width of the external area of flexure and extension; **n.c.** No calculable or measurable value due to experimental reasons or visual problems; **N-D** Diameter of the non-deformed area; **OL-D** Diameter of the outer limit of the collapse; S_p Subsidence at depth; S_s Subsidence at surface.

III.3.5.3.2 Flat silicone reservoir

➢ Plane view observations at surface allow to define two different regions for any value of R (Fig. 3.30): a non-deformed central area (N) and an annular zone of flexure and extension encircling the former (EXT). This external extensional region is composed principally by strata tilted towards the depression (T) and in few cases, a very thin annular zone with

surface fractures surrounds these tilted area. The outer limit of the external zone **(EXT)** corresponds to the outer limit of the whole collapse depression **(OL-D)** and to the diameter of the subsiding piston **(P-D)** (Fig. 3.30).
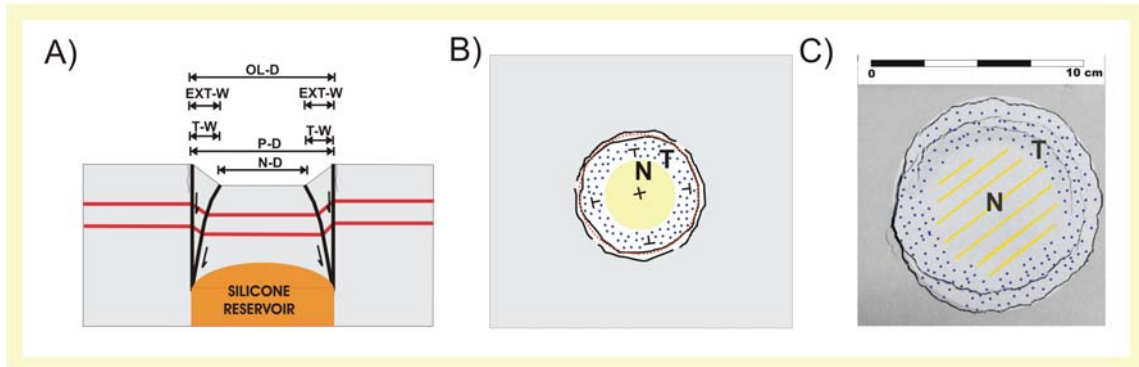

Fig. 3.30: Structural parts of a caldera collapse a silicone reservoir as magma chamber analogue. **(A)** Sketch in cross section of a caldera collapse without topography and low **R** value. **(B)** Sketch in plan view of the same collapse as in (A). Red dotted line corresponds to the plan view shape of the magma chamber. Yellow colour corresponds to the non-deformed area **N** and blue dots to the tilted area **T**. **(C)** Photograph of experiment A-6 with the three different parts. **EXT-W** Width of the external area of flexure and extension; **N-D** Non-deformed area diameter; **N** Non-deformed area; **n.c.** No calculable or measurable value due to experimental reasons or visual problems; **OL-D** Outer limit diameter; **P-D** Piston diameter; **T-W** Tilted area width; **T** Tilted area.

➤ Sharp corners of the silicone reservoir act to arrest faults. The diameter of the collapse outer limit **(OL-D)** is approximately equal to that of the silicone reservoir **(D)** for experiments with very low aspect ratios (e.g. SIL-1,SIL-2 and SIL-3). Therefore, faults bounding the subsiding block are interpreted to be circular and vertical. By contrast, **OL-D** decreases at higher roof aspect ratios **(R)** indicating that at medium **(R**=0.5-0.7) and high aspect ratios **(R**<0.7-0.85) faults controlling the subsidence are reverse and outward dipping with dip angles ranging between 85° and 70° (Fig. 3.31). Furthermore, independent of the roof aspect ratio value, a second group of internal reverse faults nucleated at depth and once reached the surface delimit the non-deformed central part of the collapse. Their dip angles are between 50°-70° (Fig. 3.31).

➤ **Temporal evolution**

The collapse process in analogue models with silicone as magma chamber analogue begins with the appearance of surface fractures in the extensional area (Fig. 3.32). The most outer faults are the first to form. Subsidence continues with the down flexure of the roof and the propagation of surface fractures around the depression fusing together or intersecting at low angles. Additionally,

some surface fractures propagate downwards (Fig. 3.32). If subsidence goes on these surface fractures propagate at depth with high dip angles and simultaneously, reverse faults nucleate at depth (Fig. 3.32). Finally, these vertical fractures reach the limit of the silicone reservoir and evolve to normal faults and the abovementioned reverse faults reach the surface. The collapse continues along the ring faults and the reverse faults.
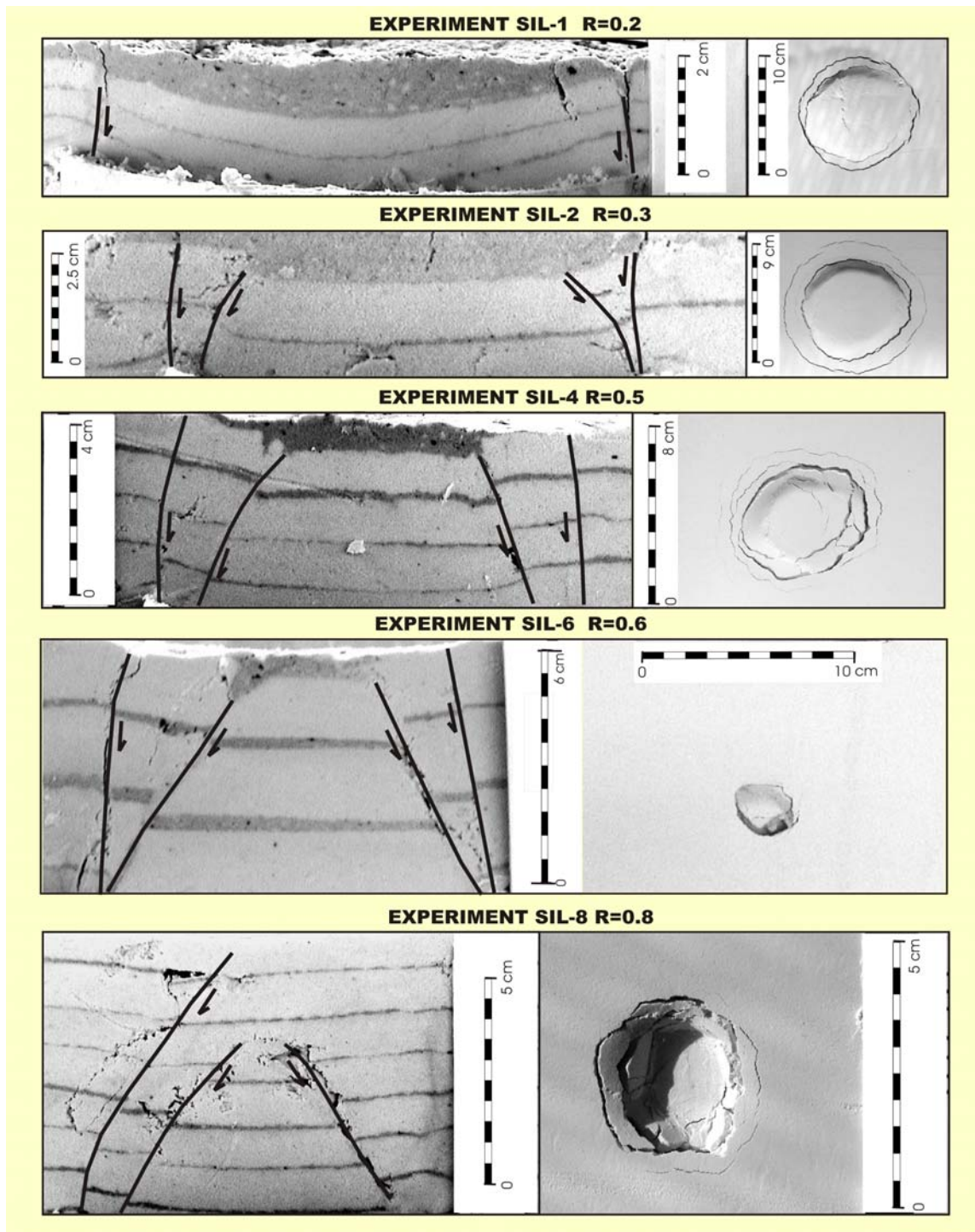

Fig. 3.32: Photographs of flat silicone reservoir experiments **(left)** Cross section. **(right)** Plan view.

Moreover, during the collapse the diameter of the non-deformed central area (**N-D**) decreases, the width of extensional area increases (**EXT-W**) and the outer limit diameter (**OL-D**) remains constant. Figure 3.33 shows th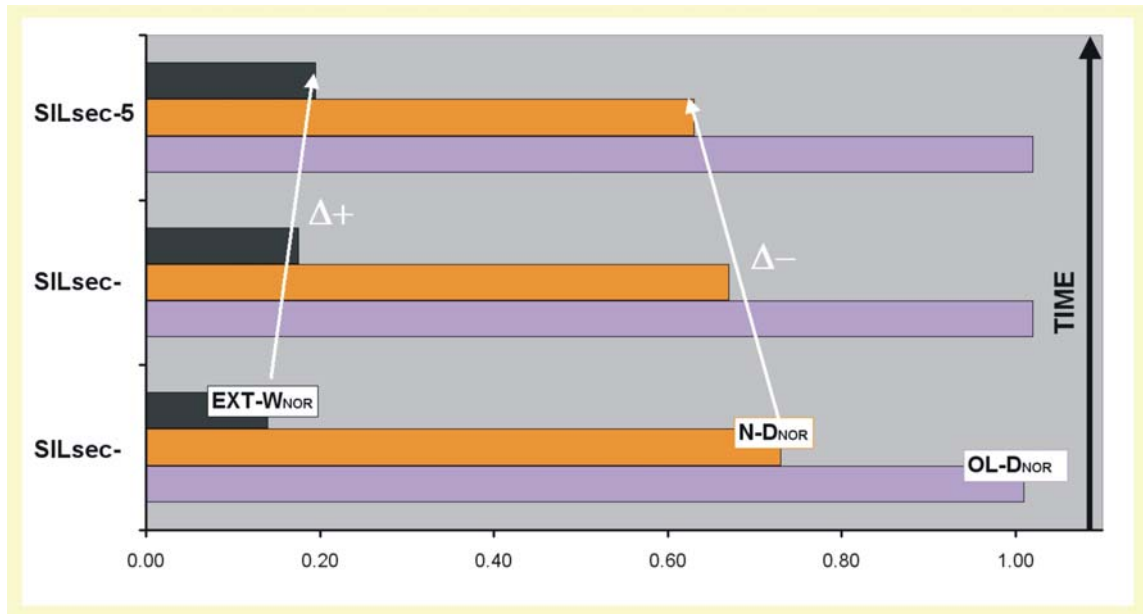e evolution in time of the extensional area width **EXT-W**, the diameter of the non-deformed area **N-D** and the diameter of the outer limit **OL-D**. Again, values are normalized, therefore:

$$\text{EXT-W}_{NOR} = \frac{\text{EXT-W}}{D} \quad ; \quad \text{N-D}_{NOR} = \frac{\text{N-D}}{D} \quad ; \quad \text{OL-D}_{NOR} = \frac{\text{OL-D}}{D} \qquad [3.7]$$

where **D** is the diameter of the silicone reservoir.

Fig. 3.33: Evolution in time of the extensional area width **EXT-W**, the diameter of the non-deformed **area N-D** and the diameter of the outer limit **OL-D**. Values are normalized.

III.3.5.3.3 Curved silicone reservoir

Experimental results for analogue models with a curved silicone reservoir as magma chamber analogue are similar to that obtained with a flat silicone reservoir. Caldera collapse is dependent on the roof aspect ratio **R** and can be piston-like for low values of R or funnel for higher **R** values. The main structural features are equivalent to those found in the analogue models with flat silicone reservoir: surface fractures, vertical or sub-vertical ring fault and outward dipping reverse faults (Fig. 3.34).
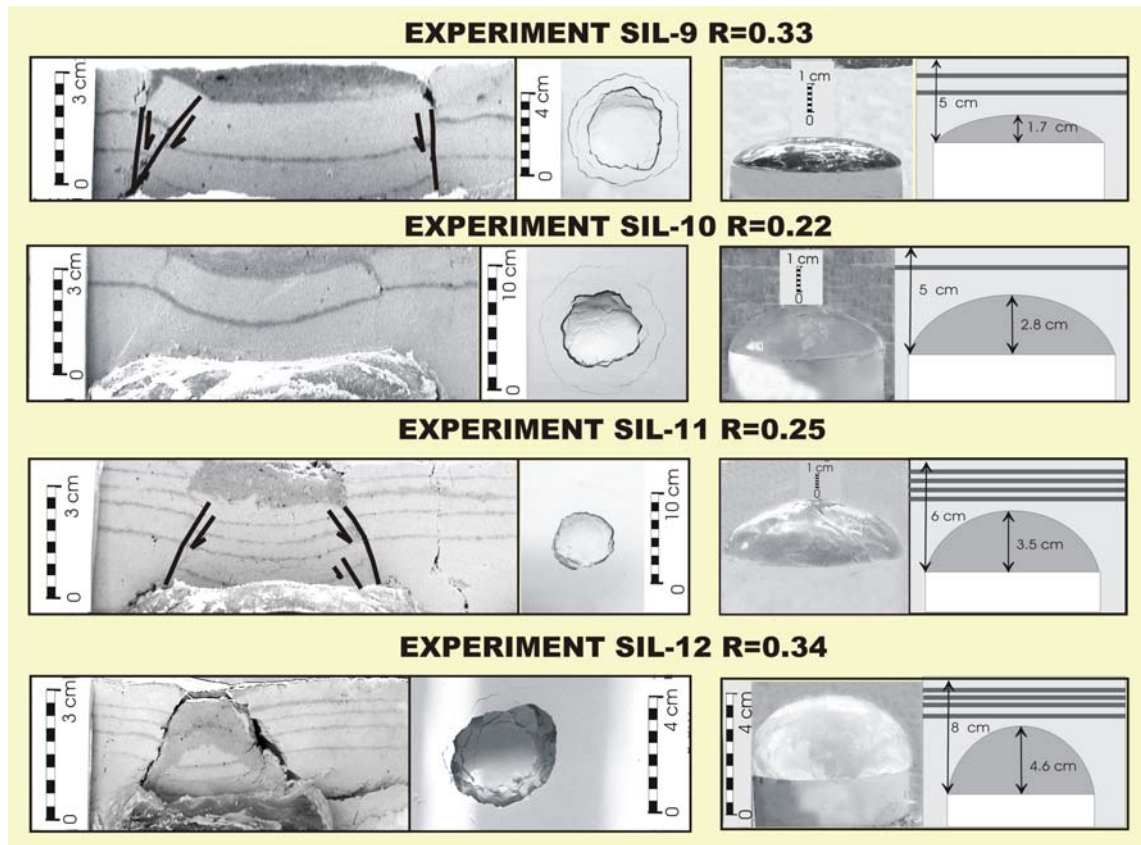
Fig. 3.34: Photographs of curved silicone reservoir experiments **(left)** Cross-section and plan view. **(right)** Photograph and sketch of the silicone reservoir).

III.3.5.3.4 Main differences between flat reservoir and curved reservoir

As mentioned in section (II.3.5.2), in experiments with a flat silicone reservoir as magma chamber analogue, the reverse faults nucleate at the sharp corners of the silicone reservoir. By contrast, with a curved silicone roof the conditions of stress field change and reverse faults nucleate at a certain distance from the reservoir corner (Fig. 3.35).
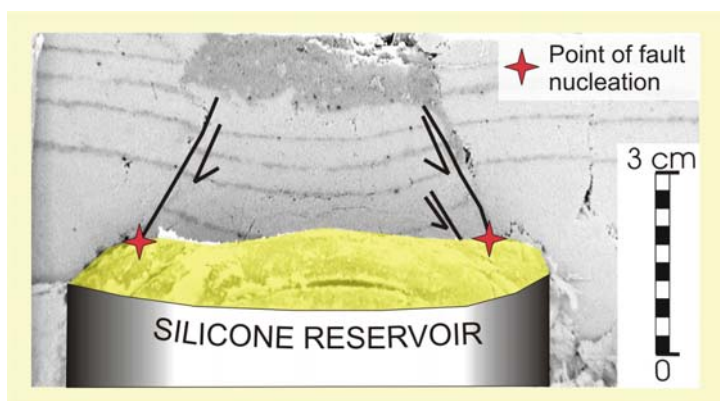

Fig. 3.35: Cross section photograph of experiment SIL-10. In yellow colour the silicone and with red stars the point of fault nucleation clearly displaced from the sharp reservoir corner.

Furthermore, for experiments with curved reservoir it is not possible to establish a correlation with the roof aspect ratio value and the collapse geometry similar to that for experiments with flat silicone reservoir. Roche et al. (2000) proposed that the roof aspect ratio of a rounded roof is defined using the minimum thickness and the diameter of the reservoir. The problem is that whereas experiments with flat reservoir similar roof aspect ratio values produce similar collapse geometries, this is not the case in experiments with curved silicone roof. Compare experiments SIL-9 and SIL-12 (Fig. 3.34), the roof aspect ratio calculated according to Roche et al. (2000) are respectively 0.33 and 0.34, almost equal values. Therefore, it is expected collapse structures and morphology to be similar. By contrast, experiment SIL-9 is characterized by vertical ring faults and a outward dipping reverse fault similar to experiments SIL-2 ($\mathbf{R}$ = 0.3) or SIL-4 ($\mathbf{R}$ = 0.4) (Fig. 3.31), and experiment SIL-12 by the presence of outward dipping reverse faults and any vertical ring fault, comparable to experiments SIL-7 ($\mathbf{R}$ = 0.7) or SIL-8 ($\mathbf{R}$ = 0.8) (Fig. 3.31). The origin of these discrepancies is the degree of curvature of the silicone reservoir. The silicone roof of experiment SIL-9 has an eccentricity e of 2.94 indicating a sill-like morphology and in experiment SIL-12 e = 1.08, corresponding to a almost hemispheric silicone reservoir. The roof aspect ratio $\mathbf{R}$ of experiment SIL-9 varies from 0.33 (in the area of minimum thickness, central part of the reservoir) to 0.5 (in the area of maximum thickness, lateral of the reservoir). The range of variation is short and it explains that the results of this experiment are similar to that of flat reservoir experiments with equivalent $\mathbf{R}$ values. In short, sill-like morphologies of the silicone roof provide similar results as experiments with flat reservoir if both experiments have the same roof aspect ratio value. By contrast, the roof aspect ratio of experiment SIL-12 ranges from 0.34 to 0.8. Therefore, obtained results are completely different from those of SIL-9 and similar to results of experiments with higher aspect ratios (SIL-7 or SIL-8).

III.3.5.3.5 Dependency of the collapse dimensions with the roof aspect ratio

Just as for balloon experiments, this section analyses the influence of the roof aspect ratio on the dimension of the caldera collapse at surface. In Figure 3.36 are plotted for silicone experiments with flat reservoir the normalized values of the outer limit diameter **OL-D**, the extensional zone width **EXT-W** and the non-deformed area diameter **N-D** towards the corresponding roof aspect ratio.
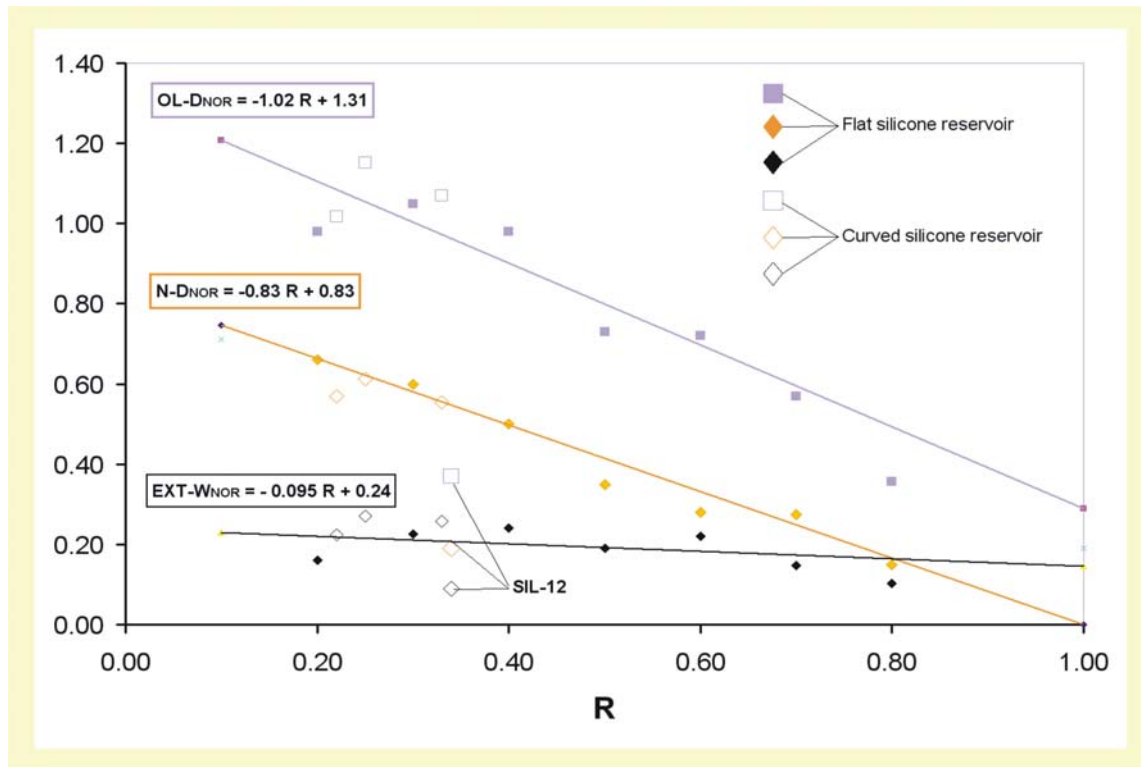
Fig. 3.36: Graph of normalized values for outer limit diameter **OL-D$_{NOR}$**, extensional zone width **EXT-W$_{NOR}$** and non-deformed area diameter **N-D$_{NOR}$** towards roof aspect ratio.

In short, with increasing roof aspect ratio the diameter of the collapse outer limit and the diameter of the non-deformed decrease linearly. Furthermore, the width of the extensional area decreases slightly, with a slope close to zero, indicating that it can be considered almost constant, independent of the roof aspect ratio. The fact that for **R** > 5 OL-D$_{NOR}$ is lower than 1, indicates that faults bounding the piston are outward dipping. Moreover, **N-D$_{NOR}$** values are always lower than 1 implying also that delimiting faults dip outwards.

In Figure 3.36 are included also the results for experiments with curved silicone reservoir. Experiments with low eccentricity (SIL-9, SIL-10 and SIL-11) show a similar behaviour as the experiments with flat reservoir. Experiment SIL-12 (**R** = 0.34), with an almost hemispheric geometry (*e* ↑), has **OL-D$_{NOR}$** and **N-D$_{NOR}$** values similar to experiments with flat silicone reservoir but with higher roof aspect ratios, like experiment SIL-8 (R=0.8).
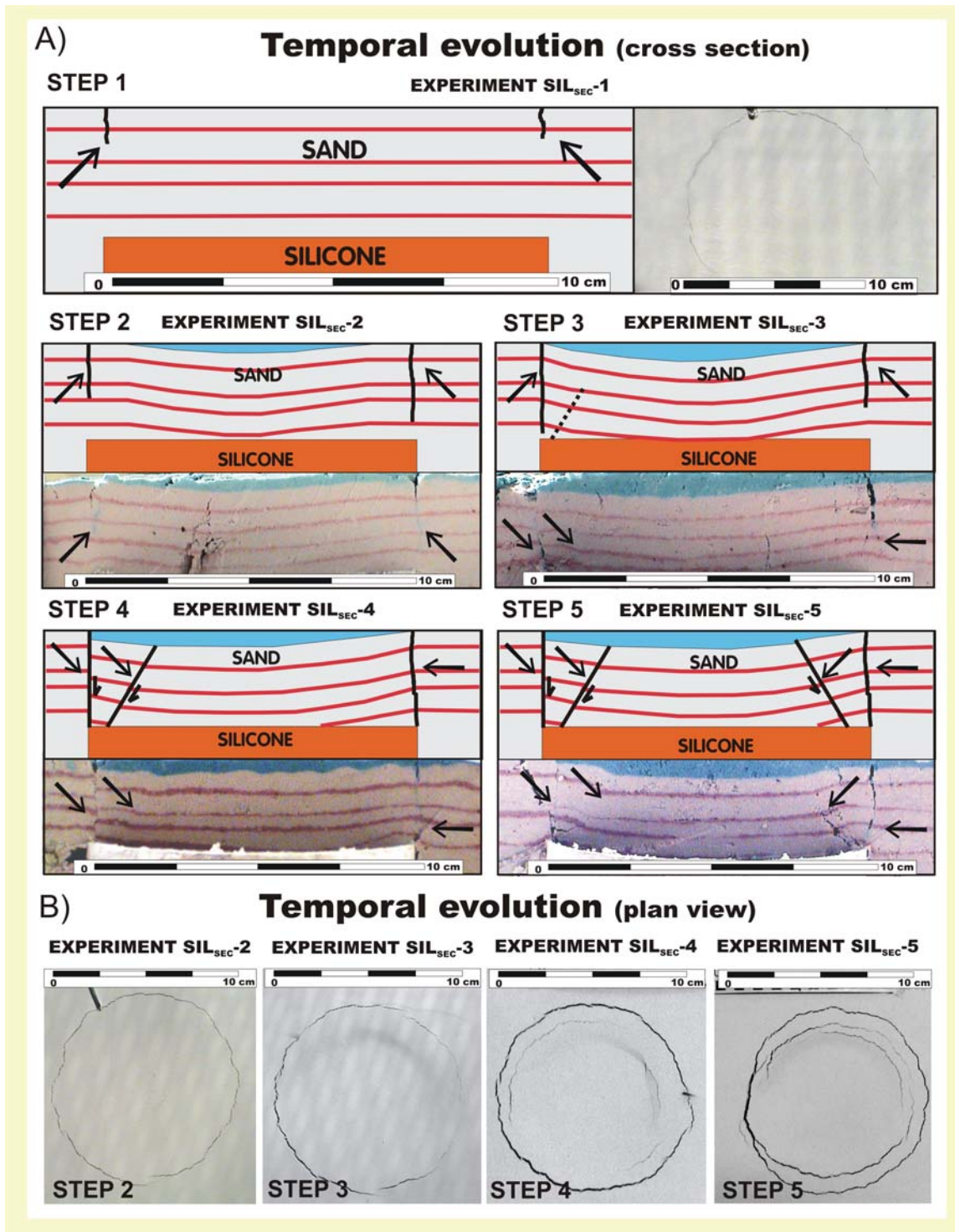
Fig. 3.33: Photographs and sketches of the experiments type SIL$_{SEC}$. **(A)** Cross sections of the experimental results. **(B)** Plan view photographs.

III.3.6 Comparison of results

III.3.6.1 Comparison between balloon and silicone models

The comparison between balloon and silicone models results may help us to infer further restrictions of both experimental methods. The three main aspects considered in this section are: differences in the structural features, the temporal evolution of the collapse process and the influence of the roof aspect ratio.

➢   **Structural differences**

Similarities:

1. At low aspect ratio values, the collapse is piston-like. The faults controlling the subsiding piston are vertical or subvertical ring faults (outward or inward dipping). A second group of "bell-shaped" reverse faults nucleated in the interior of the collapse, their dip angles range between 50º and 70º.

2. At high roof aspect ratio values, the collapsing block losses coherence. Multiple reverse faults nucleated at depth break the roof in wedges.

3. Collapse parts at surface are similar, both types of analogue models produce a non-deformed central area (N) and an external annular zone surrounding the former (EXT). This region is subdivisible in two parts: the zone of tilted strata (T) and the horizontal area with extensive surface fractures (E). The outer limit of the external zone EXT corresponds to the outer limit of the collapse structure OL and the outer limit of the tilted area T is defined by the ring faults controlling the subsiding piston.

Differences:

1. The number of fractures and faults involved in the caldera collapse process is generally higher in balloon than in silicone experiments.

2. In silicone experiments, the external area **EXT** is mainly covered by the tilted area **T** and in most cases **E** is nonexistent. By contrast, in balloon experiments, **E** is the most extensive part.

3. Since in silicone experiments the extensive zone **E** is nonexistent, the piston diameter **P-D** (outer limit of the tilted area **T**) corresponds to the outer limit of the collapse **OL** (theoretically, the outer limit of **E**). By contrast, in balloon experiments the **OL-D** (collapse outer limit diameter) is much larger than **P-D** (piston diameter) due to the large expanse of the extensive zone **E**.

➤   **Temporal evolution**

Similarities:

1. The first structures to form are surface fractures in the external extensional area **EXT**. These fractures define the outer limit of the collapse depression.

Differences:

1. In silicone experiments, the first faults to form are those that will control the subsiding piston. By contrast, in balloon experiments ring faults controlling the piston appear much later, once the extensive zone has developed.

2. In balloon experiments, "bell-shaped" reverse faults nucleated in the first stages of the collapse process, before the development of the ring faults controlling the piston. In silicone models, internal "bell-shaped" reverse faults nucleated once ring fractures have propagated downwards and develop simultaneously with the ring faults.

➢ **Influence of the roof aspect ratio in the dimensions of the collapse parts at surface**

Differences:

1. In balloon experiments, normalized values of the outer limit diameter (**OL-D**$_{\text{NOR}}$) increases with a logarithmic trend. By contrast, in the silicone models the values decrease with increasing roof aspect ratio and data fit a linear function (Fig. 3.37)
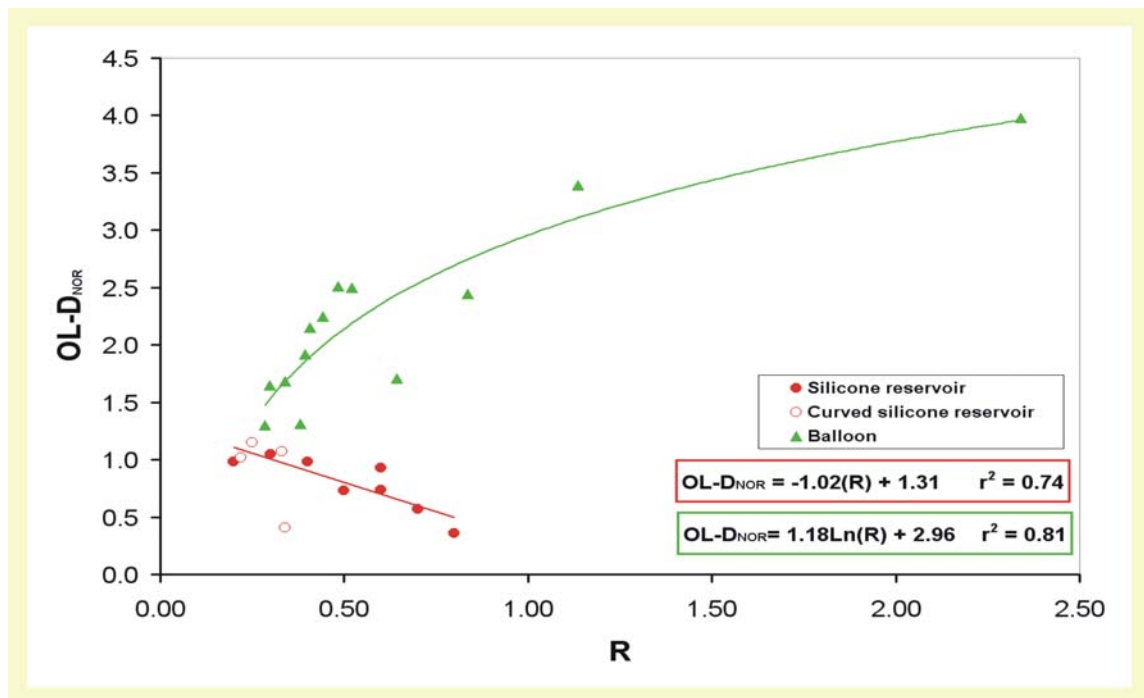

Fig. 3.37: Normalized values of the outer limit diameter OL-D$_{\text{NOR}}$ towards roof aspect ratio. In the Figure are included data for balloon and silicone models, as well as the best fit log- and linear function of both type of experimental devices.

2. In balloon experiments, normalized values for the piston diameter (**P-D**$_{\text{NOR}}$) are in most cases close to 1, independent of the roof aspect ratio value. Cases where **P-D**$_{\text{NOR}}$ >1, ring faults are vertical at depth but inward dipping at surface or simply inward dipping (Fig. 3.38). By contrast, silicone experiments have **P-D**$_{\text{NOR}}$ < 1 (except for very low values of **R**), implying outward dipping faults controlling the subsiding piston. Values of **P-D**$_{\text{NOR}}$ in silicone models are strongly influence by R and decrease with increasing roof aspect ratio (Fig. 3.38).

Fig. 3.38: Normalized values of the piston diameter P-D$_{NOR}$ towards roof aspect ratio. In the Figure are included data for balloon and silicone models, as well as the best-fit linear function for silicone experimental results.

> ➢   In balloon experiments, normalized values for the non-deformed area diameter (**N-D$_{NOR}$**) are in the range between 0.4 and 0.7 with a mean value around 0.7 (i.e. non-deformed area delimited by outward dipping reverse faults). **N-D$_{NOR}$** values of balloon experiment remain almost constant, independent of the roof aspect ratio value. By contrast, **N-D$_{NOR}$** values of silicone experiments are dependent on **R** and decrease with increasing roof aspect ratio with a linear trend (Fig. 3.39).
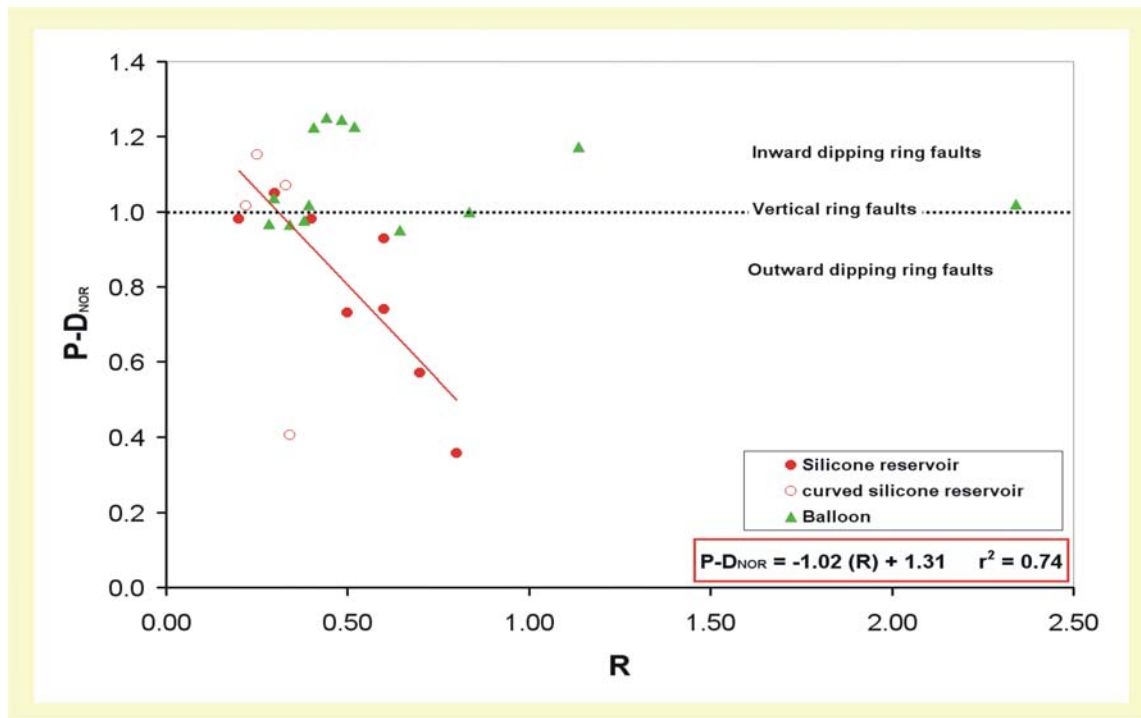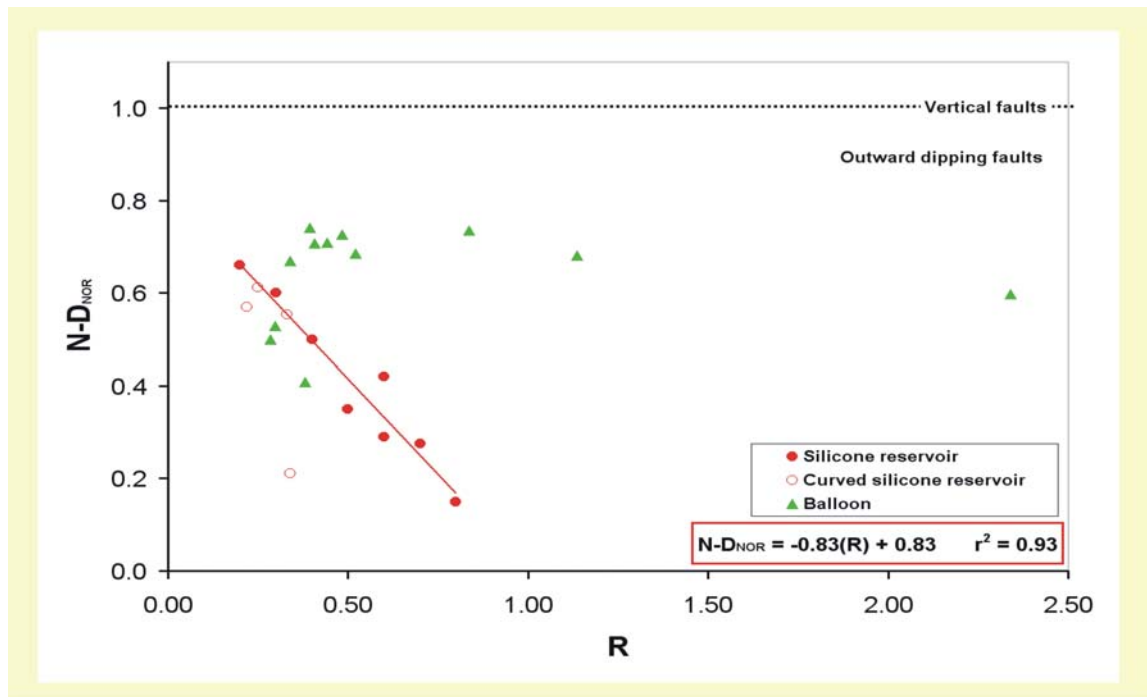
Fig. 3.39: Normalized values of the piston diameter **N-D$_{NOR}$** towards roof aspect ratio. In the Figure are included data for balloon and silicone models, as well as the best-fit linear function for silicone experimental results.

III.3.6.2 Comparison with previous studies

A comparison with previous studies is required to establish the level of coherence between the experimental results presented in this work and previously published ones.

III.3.6.2.1 Dependency of the extensional area with the roof aspect ratio

A possible analysis is to study of the influence roof aspect ratio (**R**) on the dimensions of the external area (**EXT**= area of extensive surface fractures **E** + area of tilted strata **T**, see Fig. 3.14 for more details). Roche et al. (2000) observed previously this experimental dependency and concluded that with increasing R the width of the external area remains constant and the non-deformed central area decreases. At low aspect ratios the width of the external zone is relatively thin compared to the diameter of the whole collapse structure. By contrast, at higher ratios (**R** > 2) the extensional area accounts for at least 90% of the caldera depression. Roche et al. (2000) held that this fact is in broad agreement with the critical aspect ratio 0.7 predicted by mining subsidence models.

The results the analogue models exposed in this work were subjected to a similar analysis in order to verify if they are in agreement with those of Roche et al. (2000). The percentage of external area (**% EXT**) is obtained as follows:

$$\% \, EXT = \frac{EXT}{TA} \cdot 100\%$$
[3.8]

where **TA** (total area of the collapse) is calculated as:

$$TA = \left(\frac{OL \text{ - } D_{max} \cdot OL \text{ - } D_{min}}{4} \right)^2 \cdot \pi$$
[3.9]

and **EXT** (extensional area) as:

$$EXT = TA \text{ - } \left(\frac{N \text{ - } D_{max} \cdot N \text{ - } D_{min}}{4} \right)^2 \cdot \pi$$
[3.10]

Results of balloon (A- and D-type) and silicone experiments are sum up in Table 3.14 and plotted towards the roof aspect ratio in Figure 3.40. Both sets of results may fit a log-function type **% EXT** = A Ln (**R**) + B, but the coefficient of determination is considerably low, principally for the balloon experiments ($r^2 = 0.69$). On the one hand, the layout of the balloon results has a gentle slope and all values are located above the 80% threshold. On the other hand, the fit of the silicone results has a steeper slope and values range from 45% to 85%.

In Figure 3.40 also includes the plot of the percentage of external area towards roof aspect ratio proposed by Roche et al. (2000). Their results (obtained with silicone models) fit also a log-function (Fig. 3.40). The comparison of the three curves shows that the silicone models exposed in this work and those of Roche et al. (2000) obtain similar results. For **R** values lower than 0.5 the external area covers less than the 70 %. By contrast, for roof aspect ratio values close to 1, **%EXT** is around 80%. Since the silicone experiments presented in this work do not consider roof aspect ratio values higher than 0.8, it is impossible to compare both curves beyond **R**=1. Moreover, results

for curved silicone reservoir are reasonably similar to experiments with flat reservoir with equivalent values.

Furthermore, the dependency of **%EXT** with **R** for the results of the balloon models is considerably different to that proposed by Roche et al. (2000). The main differences are: a more gentler slope and significantly higher **%EXT** values. Whereas experimental results of Roche et al. (2000) have an asymptote approximately at 80 %, balloon experiments reach **%EXT** values up to 95%.
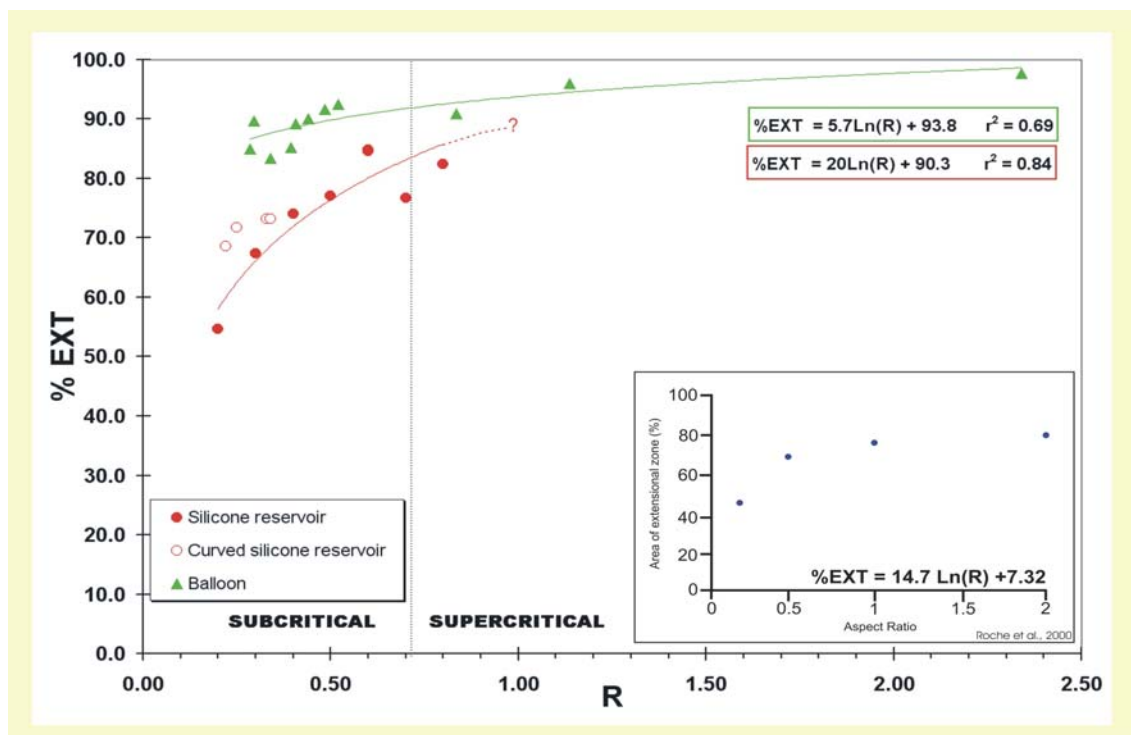
Fig. 3.40: Percentage area of the collapse occupied by the external area (**%EXT**). Dotted black line marks the limit between the subcritical (piston collapse) and the supercritical (multiple fault collapse) collapse type defined by Roche et al. (2000). On the right corner, the graph published by Roche et al. (2000). Best-fit log-functions for balloon and silicone models are also included.

In short, the results of the silicone models are comparable with previous studies (Roche et al., 2000). By contrast, balloon results show some discrepancies.

Experiments	R	% EXT	N-D / P-D	P / N-D
BALLOON MODELS				
A-1	0.28	84.95	0.52	0.59
A-2	0.3	89.69	0.51	0.56
A-3	0.38	90.42	0.42	0.89
A-5	0.39	85.19	0.73	0.54
A-6	0.44	90.06	0.57	0.62
D-1	0.34	83.33	0.69	0.50
D-2	0.41	89.20	0.58	0.57
D-3	0.48	91.64	0.58	0.67
D-4	0.52	92.46	0.56	0.76
D-5	0.84	90.86	0.74	1.15
D-6	1.14	96.00	0.58	1.69
D-7	2.34	97.72	0.59	3.94
SILICONE MODELS				
SIL-1	0.2	54.6	0.67	0.3
SIL-2	0.3	67.3	0.57	0.5
SIL-3	0.4	74.0	0.51	0.8
SIL-4	0.5	77.0	0.48	1.4
SIL-5	0.7	76.7	0.48	2.5
SIL-6	0.6	84.6	0.39	2.1
SIL-7	0.6	84.9	0.45	1.4
SIL-8	0.8	82.3	0.42	5.3
SIL-9	0.33	73.2	0.52	0.6
SIL-10	0.22	68.6	0.56	0.4
SIL-11	0.25	71.8	0.53	0.4
SIL-12	0.34	73.1	0.52	1.6
SIL_{SEC}-1	0.3	n.d.	n.d.	n.d.
SIL_{SEC}-2	0.3	n.d.	n.d.	n.d.
SIL_{SEC}-3	0.3	47.76	0.72	0.41
SIL_{SEC}-4	0.3	56.85	0.66	0.45
SIL_{SEC}-5	0.3	61.85	0.62	0.48

Table 3.14: Table of verified experiments (balloon and silicones experiments). **%EXT** Percentage of external area; **N-D** Non-deformed area diameter; **R** Roof aspect ratio; **P** Analogue magma chamber depth; **P-D** Piston-diameter.

III.3.6.2.2 Relationship between the ratios Di/Do and T/Di

A second verification is the analysis proposed by Acocella et al., (2001b). The authors studied the relationship between the ratios **Di/Do** and **T/Di** (see section III.2 for more details). In the analogue models presented in this study, the diameter of the inner depression (**Di**) presented by Acocella et al. (2001b) (Fig. 3.6) corresponds to the

diameter of the non-deformed area (**N-D**) (Fig. 3.20), the diameter of the outer depression (**Do**) (Fig. 3.6) to the subsiding piston diameter (**P-D**) (Fig. 3.20), and the thickness of the sand-pack (**T**) to the magma chamber depth (**P**). Table 3.15 sums up the experimental values of **N-D** / **P-D** (**Di/Do**) and **P** / **N-D** (**T/Di**) for balloon (A- and D-type) and silicone models (only with flat reservoir). Furthermore, Acocella et al. (2001b) proposed some natural examples (Table 3.15) in order to validate their experimental results.

Calderas	R	P (km)	N-D (km)	P-D (km)	N-D /P-D	P/ N-D
Campi Felgrei	0.25	4±0.5	10.9±0.3	16±0.3	0.37±0.06	0.68±0.03
Bolsena	0.3	5±0.5	10±0.5	16.8±0.5	0.5±0.03	0.59±0.05
Latera	0.6	5±0.5	4.1±0.3	8.3±0.3	1.22±0.04	0.49±0.06
Pantelleria	0.35	3±0.5	5.7±0.5	8.6±0.5	0.52±0.14	0.66±0.09
Rabaul	0.33	4±0.5	7.5±0.5	12.3±0.5	0.53±0.10	0.60±0.07
Tavua	0.72	4.7±0.5	3±0.3	6.5±0.3	1.56±0.29	0.45±0.08
Kilauea	0.43	3±0.5	4±0.3	7±0.3	0.75±0.17	0.57±0.07
Mauna Loa	0.52	4±0.5	4±0.3	7.7±0.3	1±0.18	0.52±0.06

Table 3.15: Geometrical features of selected calderas in nature (Acocella et al.,2001b). Roof aspect ratio **R** obtained considering **R=T/Do** (**R= P/P-D**). **N-D** Non-deformed area diameter; **P** Analogue magma chamber depth; **P-D** Piston-diameter; **R** Roof aspect ratio.

In Figure 3.41 are plotted both the experimental results and the natural values of **N-D** / **P-D** towards **P** / **N-D**. For the silicone models (only those with flat reservoir) and the natural examples, the dependency of **N-D** / **P-D** with **P** / **N-D** is well fitted (r^2 = 0.88 and r^2 = 0.89, respectively) by a linear function **N-D/P-D** = -*A* (**P/N-D**)+*B,* where again *A* and *B* are constants. Best-fit values for these parameters are included in Figure 3.41. By contrast, results for balloon models are disperse and hardly fit to a simple mathematical function.

The comparison of the different experimental results with the natural data shows that silicone experiments with flat reservoir fit almost perfectly with natural examples. By contrast, results for silicone models with curved reservoir are in disagreement with natural values. Moreover, only a small group of the balloon models results (Fig. 3.41 A) fall in the field of the natural examples. Finally, results of experiments (silicone or

balloon models) with roof aspect ratios higher than 0.6-0.7 fall far away from the natural examples and were not included in Figure 3.41.
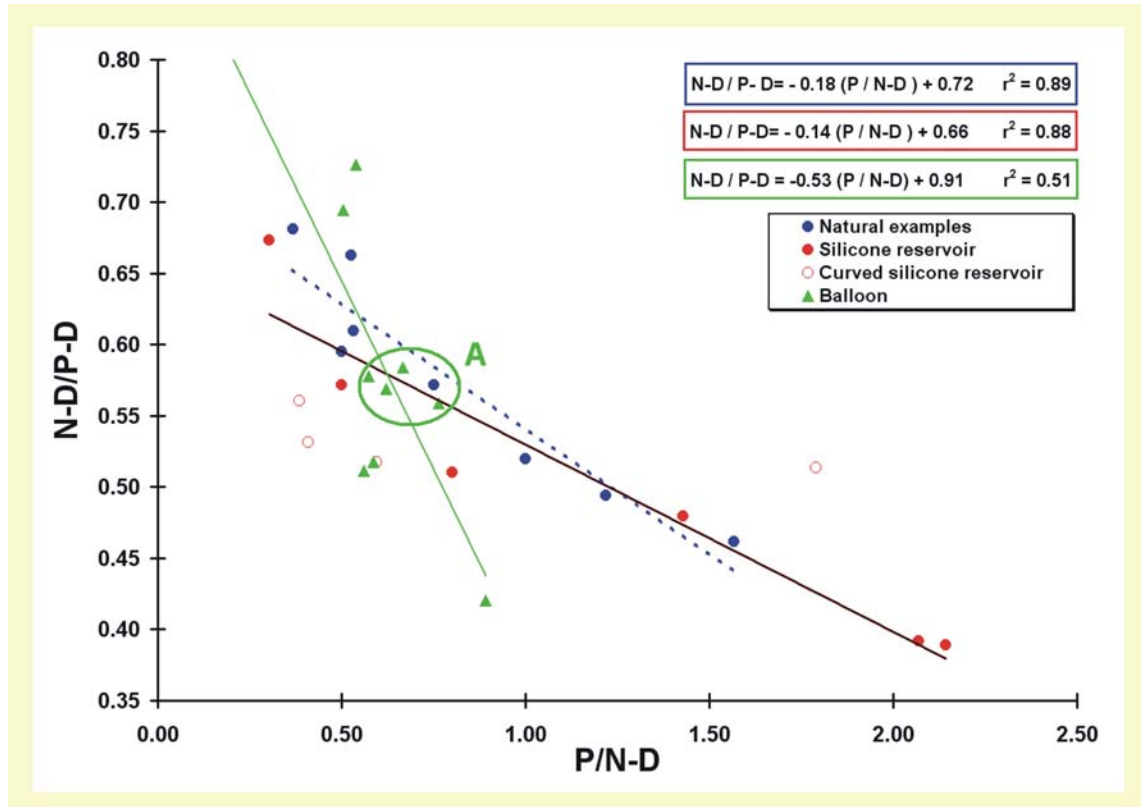

Fig. 3.41: Percentage area of the collapse occupied by the extensional area. Dotted line marks the limit between the subcritical (piston collapse) and the supercritical (multiple fault collapse) collapse type defined by Roche et al. (2000)

Possibly, structural features of silicone models with flat reservoir are similar to those controlling the collapse in the proposed natural examples up to a certain value of roof aspect ratio (**R** = 0.6). Furthermore, collapse structures of experiments with higher R values differ from those in natural systems.

All experiments (A-6, D-2, D-3, D-4) inside this group of balloon results that are in agreement with natural values, have roof aspect ratios in the range between 0.4 to 0.5 and in Figure 3.29 are those points with **P-D$_{NOR}$** value higher than 1 (i.e. inward dipping faults delimit the subsiding piston).

III.3.7 Restrictions of the experimental devices

The principal aim of this section is to sum up the main restrictions of the experimental devices applied in this work. Some of them were already mentioned in section III.2.2 and others appear after comparing balloon and silicone experiments.

III.3.7.1 Restrictions present in both experimental devices

A certain number of experimental limitations are present in both balloon and silicone models:

➢   Existence of grain flow processes due to the use of dry quartz as host rock analogue. This undesirable effect was minimized by using a very small grain size sand (40 μm of mean diameter). Fine grain sand allows vertical scarps to form in cases where previous experimental models presented grain flow processes.

➢   None of the experimental devices used up to now can simulate dike injection during the collapse process (see section III.2.2 for more details).

➢   The balloon may deflate and the silicone level may sink indefinitely, allowing the system to pass by different stages of collapse, although this is not the common case in natural systems (see section III.2.2 for more details).

III.3.7.2 Restrictions present in the balloon experiments

Some restrictions come directly from the use of a balloon as chamber analogue. In short:

➢   The elastic walls of the balloon generate unrealistic forces although these may be interpreted as the n the crystal-mush transition zone between the magma chamber and the host rock (see section III.2.2 for more details).

➢ The balloon buried close to the tank wall may alter the structures developed during the collapse process. In order to evaluate the importance of this perturbation, two types of experiments were carried out: A-type experiments where the balloon is placed in the centre of the tank and D-type experiments where the it is buried close to the tank walls. The comparison of results shows that edge effects are of second order.

➢ The balloon deforms in an elastic way when filled to its maximum capacity or at lower water capacities, the roof subsided vertically (see section III.2.2 for more details).

➢ Collapses generated with balloon models generate a huge extensional area that maybe unrealistic. There is necessary to check the existence of such a large expanse extensional area surrounding the caldera rim with field data or analytical studies.

III.3.7.3 Restrictions present in the silicone experiments

A third group of experimental limitations are related with the use of a silicone reservoir as chamber analogue. Summarizing:

➢ During the preparation phase the silicone tube is not blocked, as other authors do (Roche et al., 2000). By contrast, it remains open. This fact does not introduce important errors in the results due to the high viscosity of the silicone. The time required for the preparation of the experiment is very low in comparison to the flow velocity of the silicone. There is enough time (15-20 min) to prepare the experiment without prior deformation of the reservoir.

➢ No topography presence was considered although volcanic edifices are common in natural systems where collapse caldera occur (see section III.2.2 for more details).

➢ Silicone models have been carried out with homogenous roof above the magma chamber analogue. This is not a realistic approximation to natural systems (see section III.2.2 for more details).

> ➤   Sharp corners in the silicone act to arrest propagating faults and may modify the layout of the structural elements.

> ➤   The curvature of the silicone reservoir may influence the arrangement and features of the structural elements (see section III. 3.5.3.3 and III.3.5.3.4).

III. 4 SUMMARY AND CONCLUSIONS

Experiments on caldera collapse modelling allow a qualitative study of the structural evolution of a caldera collapse process and suggest which of factors play a more relevant role. Analogue models have verified that caldera collapse formation is influenced by multiple aspects like regional tectonics, system geometry, magma and host rock properties, pre-existing structural discontinuities, deformation history, etc.

Differences among these analogue models lie behind the applied experimental devices, the host rock analogue materials (dry quartz sand, flour, etc.), and the magma chamber analogue (water or air-filled balloons, silicone reservoirs, etc.). Although obtained results are generally similar, there exist some differences. A subsequent comparison of the experimental results with field data and analytical studies may help to infer which discrepancies come from the restrictions of each experimental design or have a counterpart in natural systems.

Furthermore, "semi-quantitative" studies with analogue models are also useful. In some cases the results are important to check analytical results or in others, to lay the foundations of future numerical analyses. Three types of semi-quantitative analyses were performed with these analogue experiments: the measurement of the erupted magma chamber volume fraction f required to achieve each step of the collapse process (and the dependency $f(\mathbf{R})$, the estimation of the subsidence pattern and the study of the influence of the roof aspect ratio in the dimensions of the collapse parts at surface. The quantification of these aspects is of particular interest for volcanic hazard. For example, the estimation of $f_{\mathbf{CRIT}}$ in the collapse onset step is important for the interpretation of volcanic deposits and volcano evolution. If the volume of extruded deposits during the pre-caldera phase is know and it is possible to establish the critical erupted magma

chamber fraction required for the caldera onset, there will be achievable to calculate the total volume of the magmatic reservoir before the completion of the eruptive event, and furthermore, the remaining magma inside the chamber. This information is crucial in order to determine the episode in the volcano history and to forecast future eruptions of the volcanic system. Furthermore, the size of the collapse at surface and the subsidence pattern are also crucial to evaluate the volcanic risk in an area with susceptible caldera-forming eruptions.